VILNIUS UNIVERSITY
CENTER FOR PHYSICAL SCIENCES AND TECHNOLOGY

ANTON KOROLIOV

SEMICONDUCTOR CHARACTERIZATION BY TERAHERTZ RADIATION PULSES

Doctoral Dissertation
Physical Sciences, Physics (02 P), Semiconductor Physics (P 265)

Vilnius, 2014

Doctoral dissertation was prepared during 2009 – 20014 at Center for Physical Sciences and Technology, Vilnius, Lithuania.

Scientific supervisor:
Prof. habil. dr. Arūnas Krotkus (Center for Physical Sciences and Technology, Physical Sciences, Physics – 02 P, Semiconductor Physics – P 265).

Scientific adviser:
Dr. Ramūnas Adomavičius (Center for Physical Sciences and Technology, Physical Sciences, Physics – 02 P, Semiconductor Physics – P 265);
Dr. Vaidas Pačebutas (Center for Physical Sciences and Technology, Technological Sciences, Material Engineering – 08 T, Material Technology – T 150).

VILNIAUS UNIVERSITETAS
FIZINIŲ IR TECHNOLOGIJOS MOKSLŲ CENTRAS

ANTON KOROLIOV

PUSLAIDININKINIŲ CHARAKTERIZAVIMAS TERAHERCINĖS SPINDULIUOTĖS IMPULSAIS

Daktaro Disertacija
Fiziniai mokslai, Fizika (02 P), Puslaidininkių fizika (P 265)

Vilnius, 2014

Daktaro disertacija rengta 2009 – 2014 metais Fizinių ir technologijos mokslų centre, Vilnius, Lietuva.

Mokslinis vadovas:

Prof. habil. dr. Arūnas Krotkus (Fizinių ir technologijos mokslų centras, fiziniai mokslai, fizika – 02 P, puslaidininkių fizika – P 265).

Konsultantai:

Dr. Ramūnas Adomavičius (Fizinių ir technologijos mokslų centras, fiziniai mokslai, fizika – 02 P, puslaidininkių fizika – P 265);

Dr. Vaidas Pačebutas (Fizinių ir technologijos mokslų centras, technologiniai mokslai, medžiagų inžinerija – 08 T, medžiagų technologija – T 150).

Acknowledgments

I would like to express my deepest gratitude to my scientific supervisor prof. Arūnas Krotkus, who gave me a chance to work and study in his laboratory, and who also provided a lot of support during the preparation of this dissertation.

I would also like to extend my appreciation to my scientific advisers dr. Ramūnas Adomavičius and dr. Vaidas Pačebutas for help during my work, discussions and explanations of my mistakes.

My sincerest appreciation is extended to my colleagues at the Ultrafast Optoelectronics Laboratory: dr. Renata Butkutė, dr. Andrejus Geižutis, dr. Andrius Bičiūnas, dr. Andžej Urbanovič, dr. Gediminas Molis, Andrius Arlauskas, Juozas Adamonis, Ieva Beleckaitė, Mindaugas Karevičius, Paulius Cicėnas.

Special thanks to my friends Pavel, Sergej, Sergej and Lena, Aleksandr and Jelena, Vlad and Natasa, Indrė, Robertas and Rūta.

I would also like to extend my sincerest gratitude to my family. Without their encouragement, it would be difficult to finish this work. Also, I am thankful to my best friend Miša, who believed in me and helped me make the decision to apply for doctoral studies.

Table of content

List of Abbreviations

pA	Picoampere (10^{-6} A)
nA	Nanoampere (10^{-9} A)
kHz	Kilohertz (10^{3} Hz)
THz	Terahertz (10^{12} Hz)
µm	Micrometer (10^{-6} m)
nm	Nanometer (10^{-9} m)
ps	Picosecond (10^{-12} s)
fs	Femtosecond (10^{-15} s)
mW	Milliwatt (10^{-3} W)
µW	Microwatt (10^{-6} W)
Al_2O_3	Aluminium oxide
CIGS	Copper Indium Gallium (di) Selenide ($CuInGaSe_2$)
CIS	Copper Indium Sulfide or Selenide ($CuInS_2$ or $CuInSe_2$)
CO_2	Carbon Dioxide
GaAs	Gallium Arsenide
GaAsBi	Gallium Arsenide Bismide
GaInAs	Gallium Indium Arsenide
GaInNAs	Gallium Indium Nitride Arsenide
GaInNAsSb	Gallium Indium Nitride Arsenide Antimonide
GaN	Galium Nitride
GaP	Gallium Phosphide
InAs	Indium Arsenide
InN	Indium Nitride
InP	Indium Phosphide
InSb	Indium Antimonide
$LiNbO_3$	Lithium Niobate
Si	Silicon
Ti:sapphire	$Ti:Al_2O_3$
Yb:KGW	Ytterbium-Doped Potassium Gadolinium Tungstate
ZnO	Zinc oxide
ZnTe	Zinc Telluride
°C	Degree Celsius
2PA	Two Photon Absorption
$\Delta T/T$	Differential Transmission
AC	Alternating Current
As_{Ga}	As-antisites
BEP	Beam Equivalent Pressure
BWO	Backward-wave Oscillator

CW	Continuous wave
DC	Direct Current
DPSS laser	Diode Pumped Solid State laser
E_g	Energy band gap
EFIOR	Electric Field Induced Optical Rectification
EO sampling	Electro Optic sampling
eV	Electronvolt
FEL	Free Electron Laser
FFT	Fast Fourier Transformation
FIR	Far Infrared
FTIR	Fourier Transform Infrared Spectroscopy
IR	Infrared
K	Kelvin
LTG	Low Temperature Grown
MBE	Molecular Beam Epitaxy
NW	Nanowires
ODBR	Optically Detected Magnetic Resonance
OPA	Optical Parametric Amplifier
OR	Optical Rectification
PE	Polyethylene
PL	Photoluminescence
PT	Photomodulated Transmittance
QC	Quantum-cascade
RT	Room temperature (20 ºC or 295 K)
RTA	Rapid Thermal Annealing
RSM	Reciprocal Space Mapping
SA	Saturable Absorption
SEM	Scanning Electron Microscope
SESAM	Semiconductor Saturable Absorber Mirror
TDS	Time Domain Spectroscopy
TRTS	Time-resolved THz spectroscopy
VLS	Vapor–liquid–solid
XRD	X-ray diffraction

1. Introduction

Since the invention of THz radiation pulse generation and detection by ultrafast photoconductors activated with femtosecond laser pulses and development of the first THz TDS systems [1,2,3], these techniques have find numerous applications for the studies of different materials in chemistry and biology [4,5]. THz radiation pulses provide unique advantages by combining rarely accessed with other means FIR part of the electromagnetic spectrum with a high temporal resolution of the measurement, therefore are widely exploited for identifying various chemical compounds by characteristic features of their vibrational and rotational spectra. THz-TDS techniques also are intensively investigated because of their potential in ranging and stand-off detection of explosives and other dangerous substances – a task that is of an extreme importance to the security systems [6].

THz pulses can be useful for characterization of semiconductor materials and semiconductor devices, too. Research on such applications has started already with the first developments of THz-TDS systems. The inventors of these systems, IBM group led by Daniel Grishkowsky have used THz-TDS for measurements of FIR spectra of dielectric response of silicon and GaAs crystals [7]. New fields of application of THz pulses were opened with the development of optical pump – THz probe technique that was successfully used for studying carrier recombination and electron intervalley scattering times in GaAs [8]. A high power THz pulses generated using amplified Ti:sapphire laser system open possibilities to perform a nonlinear THz spectroscopy measurement and develop THz pump – THz probe technique [9,10]. THz imaging has many practical applications. THz pulses give much higher imaging resolution than microwaves, are non-hazardous as X-rays and can penetrate different thin non-metal opaque objects. The higher frequency

components give better imaging resolution, but it is still not sufficient for nanoscale applications [11,12]. Such measurements are of an immense importance to the development of various ultrafast semiconductor devices and attracted numerous follow-up developments.

Our group at the Optoelectronics Department of the Center for Physical Sciences and Technology in Vilnius has started the research in this field in 2004 with the use of the optical pump – THz probe type experiments for determining electron lifetime in LTG GaAs [13] and intervalley electron scattering in germanium crystals [14]. Later-on THz-TDS was used for characterization of various narrow-gap semiconductor materials by measuring temperature dependences of characteristic times of electron momentum and energy relaxation as well as the plasma frequency in these crystals [15]. This line of research has become even more active after the proposal of a novel experimental technique – THz excitation spectral measurements [16].

1.1 Motivation

The present work is a continuation of the efforts to use THz radiation pulses in investigating semiconductor materials and ultrafast semiconductor devices. It has been performed in a close cooperation with the technological groups of the Center providing for them necessary feed-back information. Therefore, the majority of the investigated objects were grown at the Centers laboratories; numerous experiments performed on samples grown under predefined technological conditions have additionally guarantied the reliability of the obtained results and conclusions.

Three groups of materials were investigated. To the first group belong dilute bismide GaAsBi epitaxial layers grown on GaAs substrates. GaAsBi is a perspective semiconductor material which properties are not well studied yet.

This material can be used for manufacturing THz emitters and detectors, which can operate activated with femtosecond long wavelength lasers from 1 μm to 1.5 μm. GaAsBi is also considered as a prospective material for highly efficient laser diodes at telecom wavelengths [17,18] as well as for ultrafast NIR range optical switches and optical modulators. Time resolved THz pulse techniques were employed in this work also for the study of copper-indium dichalcogenide layers. CIS and CIGS layers became intensely investigated recently because this material group is perspective due to cheap production cost and efficiency that can compete with Si thin layer solar cell technologies. And finally, pulsed THz techniques, especially the THz excitation spectroscopy, were used when characterizing VLS-grown nanowire samples. GaAs nanowires have a potential to be a more efficient THz radiation emitter than the bulk semiconductor crystals. Due to nanowires orientation radiating dipole is oriented vertically and therefore strongly affects the coupling of THz radiation out of the semiconductor.

1.2 Goal of this work

The goal of this work was to develop pulsed terahertz radiation techniques and use them to study different properties of the semiconductor materials and semiconductor devices.

1.3 Tasks of this work

To reach a stated goal of the work, the following tasks were set:

1. Using the optical pump – THz probe technique study the effects of post-growth annealing on the dynamic properties of GaAsBi layers.

2. Investigate nonlinear absorption of GaAsBi layers by the optical pump – optical probe technique and determine the suitability of these layers for applications in NIR SESAM components.

3. Study the efficiency of THz pulse emission from samples with GaAs nanowires.

4. Study built-in electric fields in CIS as CIGS light absorbers at their different fabrication steps by THz pulses generation techniques.

1.4 Novelty and importance of the work

In this dissertation pulsed THz frequency range techniques are systematically used for the characterization of semiconductor materials and semiconductor devices. Several material systems: GaAsBi, GaAs nanowires, as well as CIS and CIGS layers are investigated. Short duration of optoelectronicaly generated THz radiation pulses was exploited for measuring the electron dynamics in different material with a large temporal resolution. These measurements have led to an unexpected result related to electron lifetimes in thermally annealed dilute GaAsBi. In contrast with the majority other semiconductors, thermal annealing has resulted in the shortening of electron lifetime in GaAsBi to picosecond values, which is important achievement for the application of this material in THz range optoelectronic components.

Another practically important dilute bismide characteristic that was investigated in this dissertation for the first time was the nonlinear optical absorption and its saturation. It has been demonstrated that in GaAsBi with larger than 10% Bi content absorption bleaching recovering on the picosecond time scale can be realized when the wavelengths of the optical signals are as long as 1600 nm.

Pulsed THz and optical techniques were also used for investigating material characteristics that are not accessible by other experimental techniques. As such experiments the absorption characteristics of GaAs nanowires measured by THz excitation spectroscopy as well as determination of the energy bandgap of thin high Bi-content GaAsBi layers by spectral measurement of the nonlinear absorption should be mentioned.

Implementation of the developed experimental techniques in characterization of practical devices was always in the focus of the work. The results of this studies can be applied in the production of new generation THz components, thin layer solar cells, as well as in near and mid-IR range all-optical switches. For one type of the latter devices – SESAM with bismide absorption layer, Lithuanian patent was granted.

1.5 Key statements for defense

1. Non-equilibrium carrier lifetime in GaAsBi epitaxial layers with 6% and larger Bi content decreases to picosecond values after annealing of the layers at temperatures in the range from 550 ºC up to 700 ºC, due to the stress relaxation and Bi-related defect formation.

2. Optical bleaching effect and picosecond carrier lifetimes are observed in GaAsBi/GaAs epitaxial layers at optical wavelengths up to 1600 nm making this material system suitable for the fabrication of near and mid-IR range SESAMs and other all-optical devices.

3. The samples with GaAs nanowires emit THz radiation 2-3 times better than in the bulk GaAs substrates due to enhanced light absorption because of localized surface plasmon resonances in GaAs nanowires.

4. THz emission efficiency from thin copper-indium chalcogenide layers strongly depends on their stoichiometry and on the parameters of the top transparent contact layers, thus it can be used for the mapping of built-in electric fields in solar cells made from these layers.

1.6 Dissertation layout

The dissertation consists of four sections, which are divided into smaller subsections. Concluding summaries are provided at the end of every section as well as at the end of the present Dissertation (before the references list).

The first section contains the introduction and statement for purpose, goals, tasks and statements of defense of this work and the list of author's publications and conference contributions. In the second section, the main principles of THz pulse generation and detection and the experimental setups used in the experiments are presented and explained. In the third and fourth sections, the main measurements results are presented: the results of the study with GaAsBi samples in section three, and the results of GaAs nanowires, CIS and CIGS samples study in the section four are presented.

1.7 Contribution of the author

My contribution to this dissertation includes the assembly of all experimental setups and the performance of all measurements, taking part in the experimental data analysis, writing scientific publications and presenting the results at conferences.

Coauthor's contribution

Photoluminescence and photomodulated transmittance measurements were performed by dr. B. Čechavičius from the Center for Physical Sciences and Technology in Vilnius.

First THz excitation spectra measurements were performed by A. Arlauskas from Center for Physical Sciences and Technology in Vilnius.

1.8 List of publications and conference contribution

The dissertation is based on the following scientific publications [P1-P6] and conference reports [C1 – C11], given in chronological order.

List of publications related to the dissertation

[P1] B. Čechavičius, R. Adomavičius, **A. Koroliov** and A. Krotkus: Thermal annealing effect on photoexcited carrier dynamix in $GaBi_xAs_{1-x}$, Semicond. Sci. Technol. **26,** 085033 (2011).

[P2] S. Balakauskas, **A. Koroliov**, S. Grebinskij, M. Senulis, K. Šliužienė, V. Lisauskas, S. Mickevičius, R.L. Johnson: The terahertz emission and photoelectron spectroscopy study of $CuInS_2$ thin films, Lith. J. Phys **52** (3), 214 (2012).

[P3] R. Butkutė, V. Pačebutas, B. Čechavičius, R. Adomavičius, **A. Koroliov** and A. Krotkus: Thermal annealing effect on properties of GaBiAs, Phys. Stat. Sol. C. **9** (7), 1614 (2012).

[P4] **A. Koroliov**, A. Arlauskas, S. Balakauskas, M. Šoliūnas, A. Maneikis, A. Krotkus, A. Šetkus and V. Tamošiūnas: Study of Terahertz Emission from Surfaces of $Cu(InGa)Se_2$ Layers, Acta Physica Polonica A **124** (5), 846 (2013).

[P5] **A. Koroliov**, R. Adomavičius, R. Butkutė, V. Pačebutas and A. Krotkus: Optical absorption bleaching effect in $GaAs_{1-x}Bi_x$ epitaxial layers, Opt. Quant. Electron. (2014). (**accepted for publication**).

[P6] LT Patentas Nr. 6045, R. Adomavičius, R. Butkutė, **A. Koroliov**, A. Krotkus, V. Pačebutas, pareiškėjas Fizinių ir Technologijos mokslų centras, „Puslaidininkinio įsisotinančio sugėriklio veidrodis“, išduotas

2014 06 25, paraiška patentui Nr. 2013 103, padavimo data 2013 09 26, Lietuvos Respublikos Valstybiniame patentų biure.

Conference contribution related to the dissertation

[C1] R. Butkutė, V. Pačebutas, A. Krotkus, B. Čechavičius, R. Adomavičius and **A. Koroliov**: Thermal annealing effect on properties of GaBiAs, SIMC-XVI, 16th Semiconducting and Insulating Materials Conf., 19–23 June 2011, Stokholm, Sweden.

[C2] **A. Koroliov**, R. Adomavičius, B. Čechavičius, A. Krotkus: Thermal annealing effect on photoexcited carrier relaxation in $GaBi_xAs_{1-x}$, 13th Int. Conf.-School "Advanced Materials and Technologies", 27 – 31 August 2011, Palanga, Lithuania.

[C3] S. Balakauskas, **A. Koroliov**, S. Grebinskij, K. Šliužienė, V. Lisauskas, S. Mickevičius: CIS and CZTS-based thin films for photovoltaic application, AOMD-7, Int. Conf. "Advanced Optical Materials and Devices", 28 – 31 August 2011, Vilnius, Lithuania.

[C4] **A. Koroliov** , R. Adomavičius , A. Šiušys, J. Sadowski, A. Reszka and A. Krotkus: Enhanced Terahertz Emission from GaAs Nanowires, 41st „Jaszowiec“ 2012 International School and Conference on the Physics of Semiconductors Krynica-Zdroj, 8 – 15 June 2012, Krynica – Zdroj, Poland.

[C5] **A. Koroliov**, R. Adomavičius , A. Šiušys, J. Sadowski, A. Reszka and A. Krotkus: Efficient terahertz emission from vertically aligned GaAs nanowires, 14th Int. Conf.-School "Advanced Materials and Technologies", 27 – 31 August, 2012, Palanga, Lithuania.

[C6] A. Krotkus, V. Pačebutas, A. Bičiūnas, **A. Koroliov**, R. Adomavičius, R. Butkutė, A. Urbanovič, A. Arlauskas, B. Čechavičius: THz time-domain-spectroscopy systems based on photoconductive components

made from GaAsBi, 1st Annual Conf. of COST Action MP1204 and Intern. Conf. on Semiconductor Mid-IR Materials and Optics SMMO2013, Febr. 27 – March 2, 2013, Warsaw, Poland.

[C7] **A. Koroliov**, R. Adomavičius, A. Arlauskas, A. Šiušys, J. Sadowski, A. Reszka and A.Krotkus: Efficient terahertz emission from vertically aligned GaAs nanowires, 40-oji Lietuvos nacionalinė fizikos konf., skirta Vilniaus universiteto observatorijos 260 metų sukakčiai paminėti, Birželio 10 – 12, 2013, Vilnius, Lietuva.

[C8] A. Arlauskas, **A. Koroliov**, A. Krotkus, S. Balakauskas, M. Šoliūnas, R. Suzanovičienė, A. Maneikis, A. Šetkus and V. Tamošiūnas: Terahercų dažnio spinduliuotės emisijos iš $Cu(In,Ga)(S,Se)_2$ sluoksnių, 40-oji Lietuvos nacionalinė fizikos konf., skirta Vilniaus universiteto observatorijos 260 metų sukakčiai paminėti, Birželio 10 – 12, 2013, Vilnius, Lietuva.

[C9] **A. Koroliov**, R. Adomavičius and A. Krotkus: Characterization of GaAsBi layers by means of optical pump–probe technique, 42nd Intern. School & Conf. on the Physics of Semiconductors ”Jaszowiec 2013”, June 22 – 27, 2013, Wisła, Poland.

[C10] A. Arlauskas, **A. Koroliov**, A. Krotkus, S. Balakauskas, M. Šoliūnas, A. Maneikis, A. Šetkus, V. Tamošiūnas: Study of terahertz emission from surfaces of $Cu(InGa)Se_2$ layers, 42nd Intern. School & Conf. on the Physics of Semiconductors ”Jaszowiec 2013”, June 22 – 27, 2013, Wisła, Poland.

[C11] **A. Koroliov**, R. Adomavicius, A. Arlauskas, A. Šiušys, J. Sadowski, A. Reszka, A. Krotkus: Enhanced terahertz emission from GaAs and GaAs-MnAs nanowires, 38th International Conference on Infrared, Millimeter, and Terahertz Waves (IRMMW-THz), September 1 - 6, 2013, Mainz on the Rhine, Germany.

Other conference contribution

[OC1] R. Juskenas, Z. Mockus, S. Kanapeckaite, A. Selskiene, R. Giraitis, G. Niaura, R. Kondratas and **A. Koroliov**: High Quality $Cu_2ZnSnSe_4$ Layer Formed Using Electrochemicaly Co-Deposited Cu-Zn-Sn Precursor, 27th European Photovoltaic Solar Energy Conference and Exhibition, 24 – 28 September, 2012, Frankfurt, Germany.

2. Terahertz radiation pulses (literature survey)

2.1 THz-TDS Principles

Experiments performed on semiconductor materials using different part of the electromagnetic radiation spectrum provide important information of their characteristics. The part of this spectrum with frequencies from 0.1 THz to 10 THz (or wavelengths from 30 mm to 0.3 mm) was, up to recently, largely unexploited because of the lack of suitable experimental techniques. The situation has changed with the advent of terahertz time-domain spectroscopy (THz – TDS). It is a spectroscopic technique where properties of a sample are received when a short pulse of THz radiation is transmitted or reflected through or from a sample. Semiconductor devices activated by short femtosecond (fs) laser pulses are used for THz emission and detection. Usually the duration of the laser pulse varies from several tens to several hundreds of femtoseconds.

This method was introduced in the works of the D. Grischkowsky's group [2,19,3] in the end of the 1980's. They were first to place a THz emitter in front of THz detector at a distance of up to 100 cm, and have registered the propagation of THz beams in free space. This group has used a hemispherical sapphire collimating lens to increase the output from the THz emitter, and two paraboloidal mirrors to focus THz radiation on to detector. The width of the registered transient pulse was less than 1 picosecond (ps) (approx. 0.6 ps) and the amplitude spectrum extended beyond 1.2 THz. Such a spectroscopic system was sensitive to far-infrared radiation was capable of measuring both the amplitude and the phase of the electric field (coherent detection) and had a wide dynamic range or signal-to-noise ratio (more than 10^5). This experimental setup is sufficient to be used for spectroscopic analyses. This application of THz-TDS systems was also demonstrated for the first time by the same IBM

group by measuring absorption spectra of the water vapor from 0.2 THz to 1.45 THz [20].

The main components of the THz - TDS setup are the THz emitter and the THz detector. Each of them contains a small piece of a semiconductor substrate with a Hertzian dipole antenna on it. A gap between metallic antennas conductors is activated by the femtosecond laser pulses, and therefore the device is called the photoconductive antenna or the photoconductive switch. It was for the first time demonstrated by D. H. Auston *et al*. [1]. The main parameters of the material used for the photoconductive switch are: short carrier life time (several ps for the emitters, one or less ps for the detectors), high electron mobility, large dark resistivity (10^6 Ω·cm), and high electric breakdown field.

The selection of the material for THz components also depends on the laser wavelength. First experiments were done using 620 nm femtosecond dye lasers and the best material for THz emitters and detectors was ion-implanted silicon-on-sapphire layers [20]. When the Kerr lens mode-locked Ti:sapphire laser (λ = 800 nm) was invented, the most popular material for THz emitters and detectors became GaAs grown by the molecular-beam epitaxy (MBE) at low temperatures (LTG) [21].

Later on, when THz systems became more and more popular and available, a natural decision to make these systems more compact and cheaper was conceived. First Ti:sapphire femtosecond lasers were huge and very expensive, therefore scientist started using lasers with longer wavelengths: λ = 1 μm, λ = 1.3 μm, λ = 1.55 μm. These lasers are smaller and more cost efficient, their production technologies are rather well developed, because 1.3 μm and 1.55 μm are the optical communication wavelengths. The search for proper materials for the THz systems with longer wavelength lasers was started,

because GaAs is wide bandgap material (energy gap (E_g) is 1.43 eV) and it is not as effective with long wavelength lasers. For THz systems activated by 1 μm-wavelength femtosecond lasers a suitable material is GaAsBi [17,22,23]. For THz systems activated by 1.55 μm-wavelength femtosecond lasers – Fe-implanted LTG $In_{0.53}Ga_{0.47}As$ layers grown on InP substrates were used [24,25]. Despite of this, the search for more efficient and suitable materials for THz systems continues.

Two types of fs laser systems with 760 nm - 810 nm central wavelengths range are usually used in THz setups: an amplified Ti:sapphire laser system with a 1 kHz laser pulse repetition rate [26,27] or a Ti:sapphire oscillator [28,29,30]. An amplified Ti:sapphire laser system produces low repetition rate high power laser pulses. Therefore, electro-optic crystals like ZnTe [26,27], $LiNbO_3$ (LN) [10] are usually used for pulsed THz generation and ZnTe [10,26,27] GaP [31] are used for detection. Electro-optic crystals produce and detect wideband THz radiation, but they have phonon absorption bands in THz range (at ~3 THz for ZnTe and ~6 THz for GaP), so some of the spectral information is lost during the measurement. GaAs based photoconductive emitters and detectors are usually used for THz generation and detection with Ti:sapphire oscillator laser systems [30,32,33]. GaAs has a phonon absorption band at 8 THz, which is far away from the "working" bandwidth of these type detectors, so its influence can be neglected and it is supposed that there are no losses in spectral information during measurements. However, due to a small photoconductive gap, the photoconductive emitters and detectors saturate at high laser power.

2.1.1 Classification of the THz emitters and detectors

The THz radiation sources can be divided in to two groups: continuous wave (CW) and pulsed. CW THz radiation sources are: methanol (and other molecular) lasers pumped by a CO_2 laser [34], terahertz quantum-cascade (QC)

lasers [35], free electron lasers (FEL) [36], backward-wave oscillators (BWO) [36], photomixers [37]. These THz radiation sources are not widely used due to some disadvantages. The molecular and free electron lasers are bulky and expensive. The QC lasers need additional cooling. On the other hand, the advantages of these THz radiation sources are: their output power is in the mW range, the operation setup is simple, the frequency bandwidth is narrow and allows measurements at discrete wavelengths, which is useful in some THz imaging and THz tomography applications [38,12]. From this point of view, QC lasers and photomixers are promising THz radiation sources. Therefore, they are intensively developed in order to enhance the output power of photomixers and raise the operating temperature of QC lasers [39].

The majority of current THz applications use the pulsed THz radiation sources driven by the femtosecond (fs) laser pulses. The most widely used generation methods of pulsed THz radiation are: the photoconductive antennas [1], the THz emission from the surface of semiconductors [40], the electro-optic effect [41,42] and THz generation in the air or in another gas plasma [43,44]. In comparison with the CW THz radiation sources pulsed THz radiation sources produce wideband radiation. Most of them produce the THz radiation with maximum frequencies reaching 5 - 7 THz, however, some groups report producing up to 40 THz [44], 60 THz [45] or 100 THz [46] bandwidth. The wide bandwidth THz radiation sources are very important for spectroscopic applications. A compact THz spectrometer can be done using the THz emitters and the THz detectors based on photoconductive antenna in conjunction with the fs fiber laser [47]. However, the main disadvantage of pulsed THz radiation sources is a weak (order of μW) average radiation power, which motivates continuous attempts to improve this parameter.

THz radiation detection methods can be divided into two groups: coherent and non-coherent (also called direct detection) methods. The non-coherent THz radiation detection methods mostly measure the power of the THz radiation. Coherent THz radiation detection methods measure the amplitude and the phase of the THz radiation. The non-coherent THz radiation detectors are: the liquid helium cooled Si bolometers [48], the Golay cells [49], at room temperature (RT) operating microbolometers [50] or pyroelectric detectors [51], the photomixers [52]. The coherent THz radiation detectors are based on the photoconductive antenna [2] or on the electro-optic sampling technique in nonlinear optical crystals [53] or in the air plasma [44].

2.1.2 THz photoconductive emitter and detector

In this subsection, I briefly describe most widely used generation and detection techniques of THz pulses.

The most popular method of THz generation and detection is to use photoconductive switches activated by femtosecond laser pulses (see Figure 1). The photoconductive switch is made of ultrafast semiconductor materials, materials with short carrier recombination times. The MBE grown layers with 1 – 2 ps carrier life times are usually used for the THz detectors, while for the THz emitters – typical lifetimes are 5 - 10 ps. Laser photon energy should by slightly above the bandgap of semiconductor material. For example, the most effective material for THz optoelectronic components for 800 nm Ti:sapphire lasers is the LTG GaAs. The bandgap of GaAs is 1.43 eV and 800 nm Ti:sapphire laser photon energy is 1.55 eV. This is the reason why LTG GaAs is not a suitable material for long wavelength lasers (1 μm – 1.24 eV; 1.55 μm – 0.8 eV).

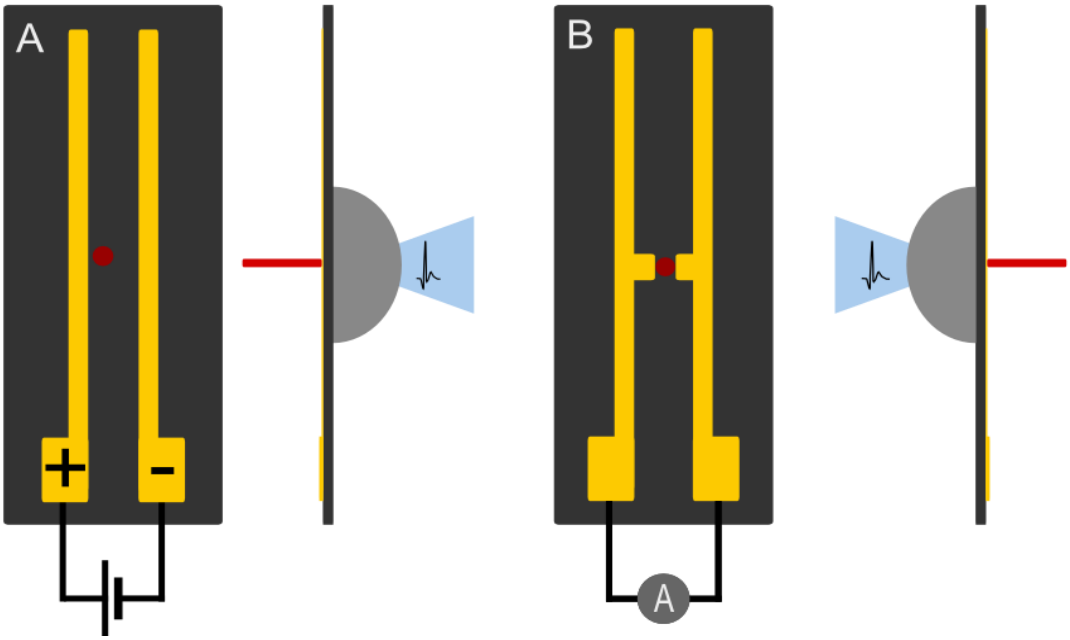

Figure 1. The photoconductive switch with a hemispherical Si lens used as a THz emitter (A) and as a THz detector (B). Red dot and line represent laser spot.

Dipole antenna is manufactured on semiconductor surface by means of photolithography. There are two parallel metallic stripes for emitters, while for detectors H–shaped structures are used. The distance between antenna lines is called a gap. It is about 10 µm wide for emitters, and about 5 µm wide for detectors. In THz systems with amplified (high impulse energy) fs laser systems, a wide gap photoconductive antennas are used [54,55]. A hemispherical Si lens is attached on the other side of the semiconductor [2]. THz emitter usually biased with DC voltage in range of 10 to 50 V (depends on semiconductor material parameters). When the laser pulse illuminates the biased photoconductive antenna gap, its resistance decreases suddenly, and rapidly changing photocurrent in the far field leads to the generation of a short one-period electromagnetic pulse. Such short pulses in the time domain correspond to the broad spectra in the frequency domain. Here's how THz radiation is created.

When a photoconductor is illuminated with laser pulses, changes its conductivity σ. Conductivity changes in a photoconductor illuminated with laser pulses is a complicated process, involving several phenomena like hot electron and hole pair generation, their fast thermalization, ballistic acceleration in external electric field, electron drift velocity overshoot [56], and electric field screening [57]. Hertzian dipole generated electromagnetic pulse *p(t)* electric field in distance *r*, can be written as:

$$E(t) = \frac{1}{4\pi\varepsilon_0 n^2}\left(\frac{p(t)}{r^3} + \frac{n\partial p(t)}{cr^2\partial t} + \frac{n^2\partial^2 p(t)}{c^2 r\partial t^2}\right) sin\theta, \quad (1)$$

where θ is the angle between the laser pulse incidence direction and the dipole axis, ε_0 – vacuum permittivity, n – refraction index of a material between two dipoles [1]. Equation (1) has three terms: the quasi-static field, the near field, and the far field, each characterized by different spatial and temporal dependences. THz electric field propagating in the perpendicular direction to the Hertzian dipole in the far-field can be written as:

$$E(t) = \frac{\mu_0\partial^2 p(t)}{4\pi\partial t^2}, \quad (2)$$

or

$$E(t) = -\frac{e\mu_0\partial I(t)}{4\pi r\partial t}. \quad (3)$$

As it can be seen, the THz radiation electrical field in far field is proportional to the time derivative of the emitter photocurrent.

A THz detector antenna works similarly. However, it is not biased by an external voltage, unlike the emitter antenna. A current change between the contacts of photoconductive detector is proportional to the arrived THz electric field amplitude and conductivity changes when it is gated by the femtosecond

laser pulses. The photocurrent in the antenna is the convolution of the THz electric filed E_{THz} and the photoconductivity induced by the laser pulses *g(t)*:

$$J(t) \propto \int_{-\infty}^{\infty} E_{THz}(t) g(t) dt. \quad (4)$$

2.1.3 THz emission from the surface of semiconductors

Another method to generate THz radiation pulses is the generation of THz radiation from the surface of a semiconductor. A surface of semiconductor refers to the depth of laser pulse absorption by the semiconductor (for example, in GaAs it is ~1 μm, in InAs it is ~150 nm at 800 nm wavelength). The THz emission occurs when a semiconductor surface is illuminated by femtosecond laser pulses. It is a very simple way of THz generation because special antennas or bias voltage are not needed. The surface THz emitter can be very compact and THz radiation can be easily collected and focused using THz lenses and mirrors. The other advantage is that it is a non-contact and a non-destructive way of using the effect of THz generation for study of generating semiconductor material. However, the THz generation efficiency (about 10^{-5}) is not as high as with photoconductive emitters (~10^{-3}). Almost any direct band gap semiconductor can be a surface THz emitter, but narrow-gap semiconductors are more efficient THz radiation emitters (see Figure 2). The p-InAs are the most efficient.

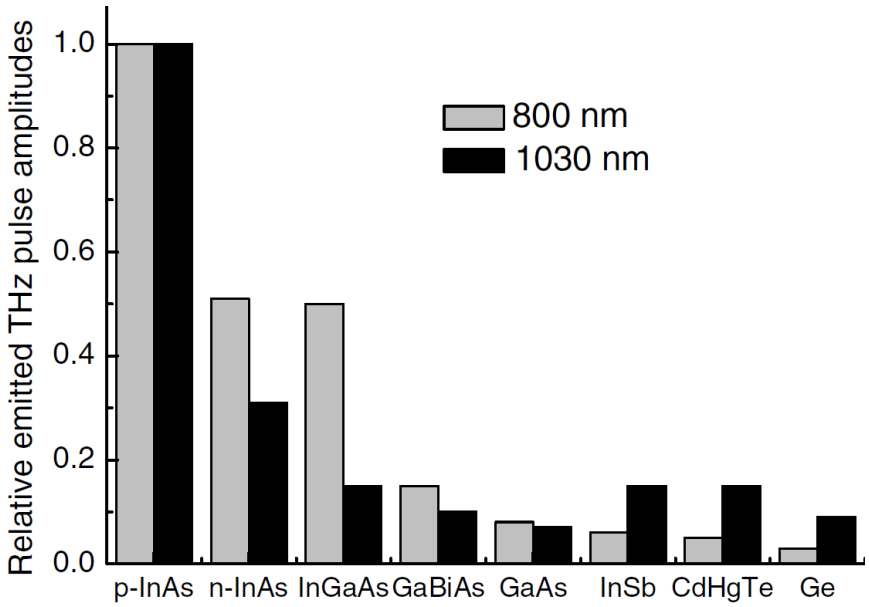

Figure 2. THz emission from different semiconductor surfaces excited by two different wavelength femtosecond laser pulses (adopted from [58]).

Generally speaking, the THz radiation from the surface of semiconductor is emitted by a dipole that is induced due photocurrent surge or nonlinear optical processes. In the far field the THz field can be expressed as [59]:

$$E_{THz} = -\frac{S}{c^2 r}\int_0^{\infty}\left(\frac{\partial j}{\partial t} - \frac{\partial^2 P}{\partial t^2}\right)dz, \tag{5}$$

Where c is the speed of light in vacuum, r is the distance from the point of observation to the emitting region; S is the area of laser beam spot on the surface of semiconductor, j and P is the photocurrent and the nonlinear polarization components in the direction of the THz wave polarization. Integration is carried out over the depth z. Expression (5) is correct when laser beam diameter is smaller than emitted THz wavelength.

The next subsections will shortly describe physical mechanisms of THz radiation from the surface of particular semiconductor materials.

Built-in surface electric field

In 1990 X. -C. Zhang *et al*. demonstrated the ability of generating THz radiation from the surface of semiconductor excited with femtosecond laser pulses without any applied bias voltage [40].

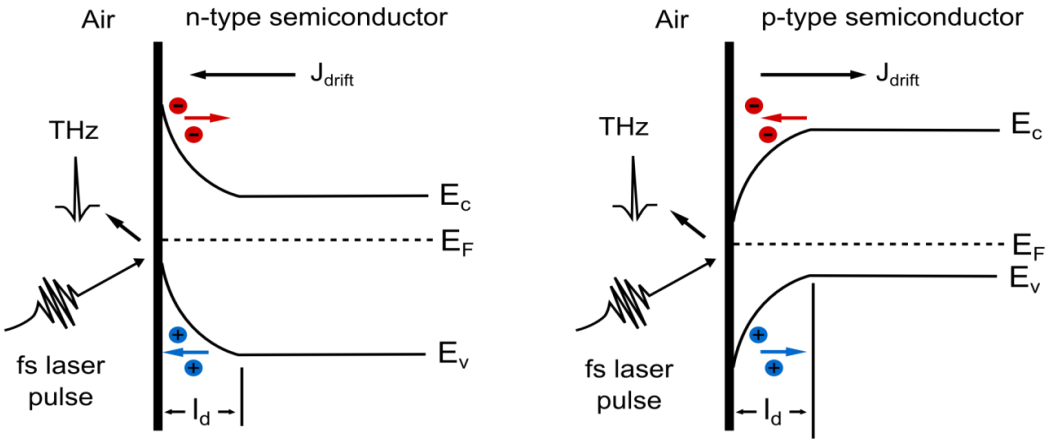

Figure 3. Band diagram of an n-type and p-type semiconductor. Photocarriers that are generated by fs laser pulses are swept across the depletion width l_d by the built-in depletion field and emit THz pulses.

Figure 3 illustrates a band diagram of n- and p-type semiconductor. The presence of surface states in the band gap of the semiconductor leads to the Fermi level "pinning" near the semiconductor/air interface, and the conduction and valence band bending. Appearing charge depletion layer forms the built-in electric field at the surface. The strength of this field can be up $10^4 – 10^5$ V/cm. When a femtosecond laser pulses with the photon energy greater than the band gap are absorbed, electron-hole pairs are created. The built-in electric field drives the carriers into opposite directions, like in the photoconductor emitter, and produces fast changing photocurrent. The rise time of the photocurrent is on the order of laser pulse duration, and the decay time is the transit time of free carriers through the depletion layer. Fast changing photocurrent is an

effective source of THz radiation with the amplitude defined by the time derivative of the photocurrent [40].

To achieve the maximum amplitude of the THz radiation from the semiconductor surface, the incident angle of the laser beam should be close to the semiconductor Brewster angle [40,60]. However, usually the incident angle of the laser beam is chosen to be 45°. This mechanism is also called photocurrent surge effect. The stronger is the surface band bending in semiconductor the better THz emitter it is. N- and p-type semiconductors generate opposite polarity THz pulses, which reflects the fact that they have opposite polarity static surface electric fields [40,60].

Due to the presence of strong surface electric field and relatively long absorption depth this THz generation mechanism is common in wide bandgap semiconductors like InP [40,60] and GaAs [61,62].

Photo Dember field

The THz radiation can be generated from the surface of semiconductor even if the surface electric field is weak. This can be possible due to different electron and hole mobility (photo Dember effect). The photogenerated electrons have a higher mobility than holes, so they move faster from the point of their excitation on the surface into the bulk of material. Electrons and holes are spatially separated and electric field transient is generated. This field accelerates the holes and slows down the electrons. So finally, electrons and holes start to move together as a single quasi-neutral packet [58].

Usually the photo Dember effect is studied for the case of stationary photoexcitation, when the drift-diffusion approach is correct. In this case, the carrier's temperature is the same as the lattice temperature and the Dember voltage is low, and is of the order of 10^{-2} V [58,59]. However, in narrow gap

semiconductors, like InSb and InAs, excited with femtosecond Ti: sapphire laser pulses electrons remain hot for several picoseconds due to high excess energy (>1 eV) and travel much longer distances then thermal electron and hole separation length. So, for the first hundreds of femtoseconds after the photoexcitation, the electron movement is purely ballistic rather than diffusive, and surface photovoltage can be very large (up to 1 V) [59].

It was mainly thought that the momenta of photogenerated electrons and holes are distributed isotropically in momentum space. However due to specific symmetry of the hole wavefunction in zinc-blende semiconductors like GaAs and InAs, distribution of photocarriers over momenta is anisotropic. It has been found that this anisotropy can cause the appearance of the lateral photocurrent at semiconductor surface illuminated by the linearly polarized light [63,64]. This lateral photocurrent is smaller than the perpendicular component, but due to its orientation it produces THz radiation that can be more efficiently out-coupled from the semiconductor bulk than the radiation that was generated by the carrier movement in direction perpendicular to the surface [58,59]. The indirect proof of this optical orientation effect was found in measurements of the angular dependences of THz radiation from InAs [65]. It was found that radiating dipole is tilted away from the normal to the crystal surface.

Optical rectification (OR) and electric field induced optical rectification (EFIOR)

In a non-centrosymmetric semiconductor the low-frequency nonlinear polarization *P* responsible for the optical rectification effect is given by the relation:

$$P = \chi^{(2)} E E^* + \chi^{(3)} E E^* F \qquad (6)$$

Where E is the electric field of the laser pulse, $\chi^{(2)}$ and $\chi^{(3)}$ are the second and the third-order nonlinear optical susceptibility tensor, F is DC electric field. The first term describe optical rectification (OR) effect the second term describe electric field induced optical rectification (EFIOR) effect. The origin of F field can be the built-in surface electric field, or the field appearing during spatial separation of photocarriers. The azimuthal angle dependence measurements are traditionally used for separating the optical rectification contribution from the THz radiation emission from the photocurrent surge processes because current surge processes do not cause azimuthal anisotropy. The azimuthal angle dependence measurements can also help to separate OR and EFIOR effects [66]. It can be done performing this experiment on (100) orientation samples. If the THz emission is induced by the OR effect it amplitude changes will have $cos2\theta$ dependence, however THz emission induced by the EFIOR effect will not depend on azimuthal angle θ at all.

For a specific semiconductor material sometimes it is difficult to determine which THz generation mechanism is dominating because it depends on sample crystallographic orientation, laser excitation wavelength and fluence, as well as on the sample doping type and level.

The most controversial material is InAs. It was a long while thought that photo Dember field is the main mechanism of THz radiation generation in this material [67]. However, recent studies shown that it is not true [59,68]. The evidence of azimuthal dependence of $\cos3\theta$ in (111) orientation n- and p-type InAs sample, and generation of *S*-polarized THz radiation cannot be caused by the photocurrent surge mechanism. The OR contribution was also neglected after performing azimuthal dependence measurements on (100) orientation n-InAs sample [66]. Therefore, it was concluded that THz radiation is generated in InAs by the influence to instantaneous polarization due to electric field

induced optical rectification (EFIOR) at the surface of semiconductor [68]. The photocarrier accelerating electric field was formed due to carries spatial separation when it is moving ballisticaly during first several hundredths of femtoseconds. This was measured using two excitation pulses scheme, where the first pulse (pump) was parallel to the surface normal, and another one (probe) was incident on the surface at 45º angle. The probe pulse generated *S*-polarized THz radiation was measured as a function of the time delay between the pump and probe pulses [59].

Excitation of InAs or InSb with 1.5 eV (800 nm) laser pulses can cause the electron scattering into the *L* valley, whose energy is 1.08 eV for InAs [69] and 1.03 eV [70] for InSb from the top of the valence band. Inter-valley scattering can decrease THz emission efficiency because electron mobility in the *L* valley is much smaller than in the *Γ* valley. This may be the explanation for why the InSb is a worse THz surface emitter than InAs albeit the InSb electron mobility (~ 76 000 cm^2/Vs) is twice a high than InAs (~30 000 cm^2/Vs) [70].

Later on, it was found that magnetic field can enhance THz radiation from the surface of semiconductors [71,62]. Presumably magnetic field rotates radiating dipole and therefore strongly affects the coupling of THz radiation out of the semiconductor. Moreover, all details of such enhancements are still not clear.

2.2 Semiconductor investigation with THz radiation pulses

In this subsection, a description of how THz pulses can be used for semiconductor properties analysis will be presented.

2.2.1 THz -TDS setup

Terahertz time-domain spectroscopy setup, which was introduced by D. Grischkowsky's group, is shown in Figure 4. This setup scheme is widely used with minor modifications.

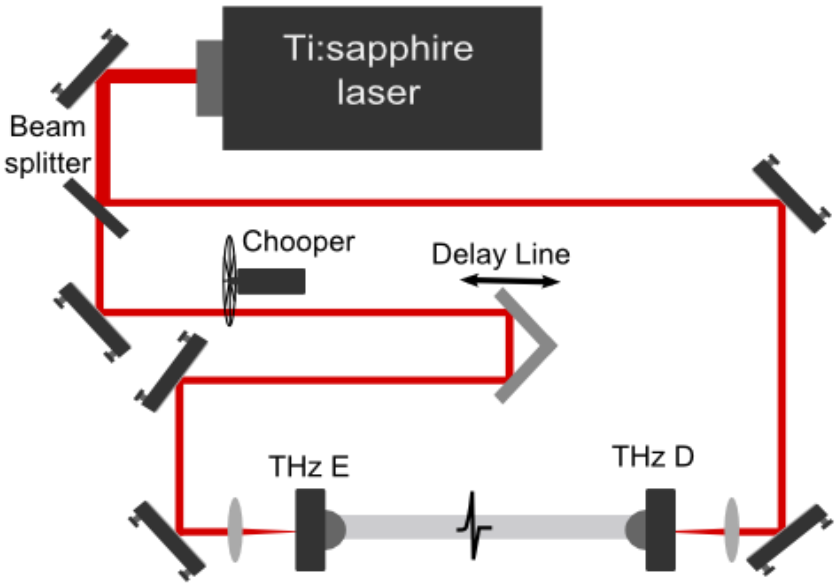

Figure 4. THz-TDS setup

The femtosecond laser pulse is divided in to two parts. The optical path of two branches must be equal. One part is activating the biased photoconducting emitter, while the other is gating the photoconducting detector. The THz pulse from the emitter is guided to the detector, and the electric field of the THz pulse is sampled in the detector by changing the relative delay between the two parts of the optical pulses. The signal from the THz detector is usually weak - approximately of pA to nA order of magnitude. To detect such small signals, a lock-in amplifier is used. This synchronous measurement technique requires a

mechanical chopper to be placed in the emitter or the detector branch. There are setups without choppers, when an emitter is biased with the AC voltage. The typical operation frequency of the chopper is 1-2 kHz. The higher the chopper frequency is, the better the signal-to-noise ratio of the signal measured by lock-in amplifier becomes. The delay line is used for temporal scanning of the generated THz pulses. The delay line and the lock-in amplifier are controlled using computer. By performing FFT calculations of the registered THz signal, its spectrum and phase can be attained (see Figure 5).

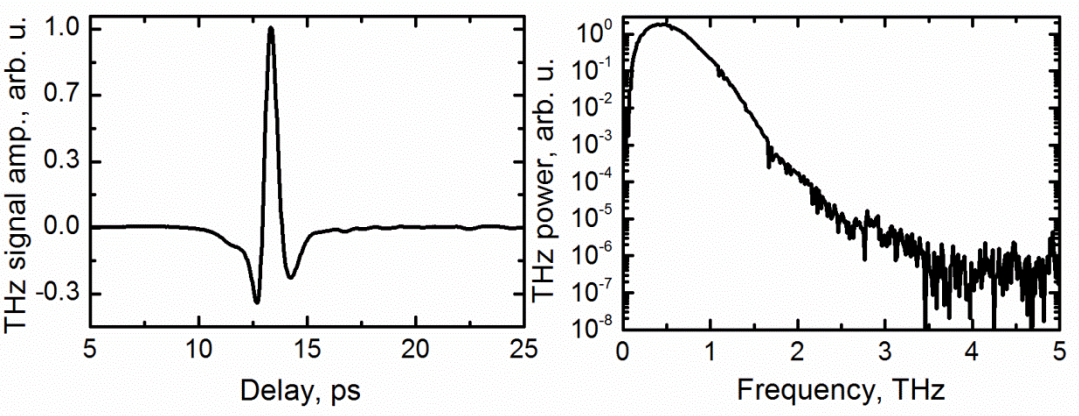

Figure 5. Registered THz signal amplitude and its calculated spectrum.

2.2.2. Studies of dielectric response

The dynamics of carriers in semiconductors are important both for scientific research and for semiconductor industry. However, interesting phenomena usually occur at frequencies comparable to either the frequency of the plasma or the damping rate, and these frequencies are in the region of the THz. The strongest absorption of the free carriers lies below 2 - 3 THz. It is difficult to reach these frequencies with microwaves or far-infrared because the techniques and measurements are usually time-consuming. Therefore, THz-TDS is a good instrument to study such phenomena [72].

When a conducting sample is placed in a TDS system between the THz emitter and the THz detector, the registered signal is the THz pulse that is transmitted through sample. Its amplitude and spectrum are affected by the dielectric properties of the sample. When this pulse is compared with reference pulse, the characteristics of absorption (signal amplitude attenuation) and refraction (delay) of the sample to the THz radiation can be studied (see Figure 6).

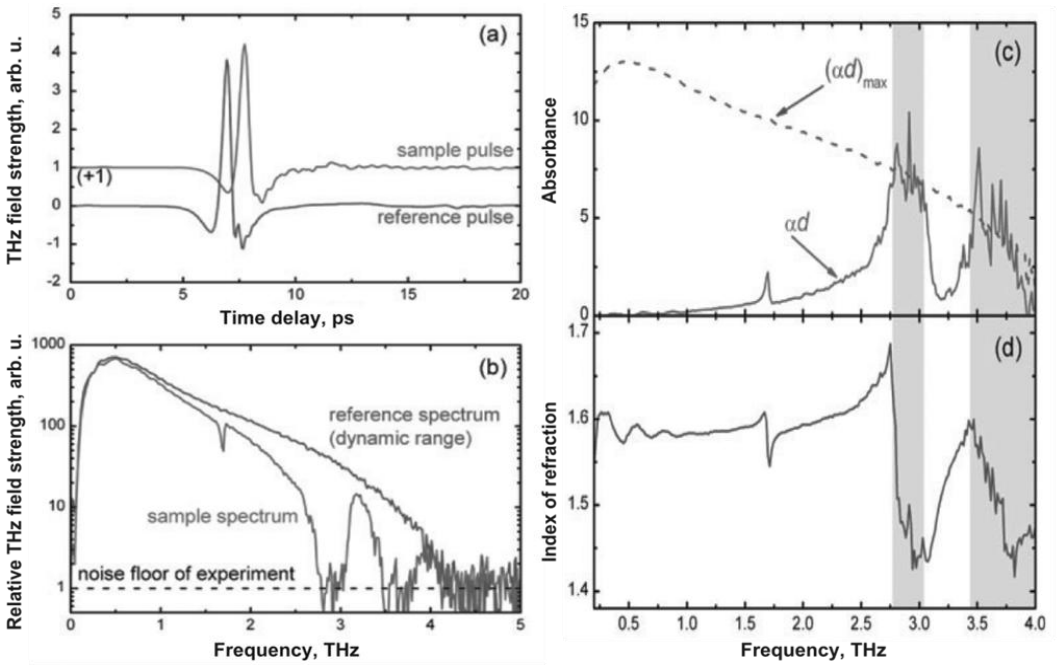

Figure 6. (a) Time traces of the reference and sample pulses in a transmission THz - TDS experiment, (b) frequency spectra of the reference and sample pulses with respect to the noise floor of the experiment, (c) the extracted absorbency αd and the highest detectable absorbance $(\alpha d)_{max}$, and (d) index of refraction of the sample material. The sample consisted of a mixture of cytosine and PE filler, and the measurement was carried out with a nominal sample temperature of 10 K (adopted from [73]).

The same is true for reflection spectroscopy. The measurement results can be interpreted using the Drude theory [72], and it shows that the THz-TDS method can be used to determine the complex conductivity and study the

dielectric response of semiconductors in the THz range. The data analysis for thick and thin samples is different due to overlapping multiple THz pulse reflections from air/sample interfaces in the thin sample (see Figure 7). In thick samples, the reflected pulses are not overlapping. Therefore, the reflected pulses are not counted, and only the main pulse is used for the calculations.

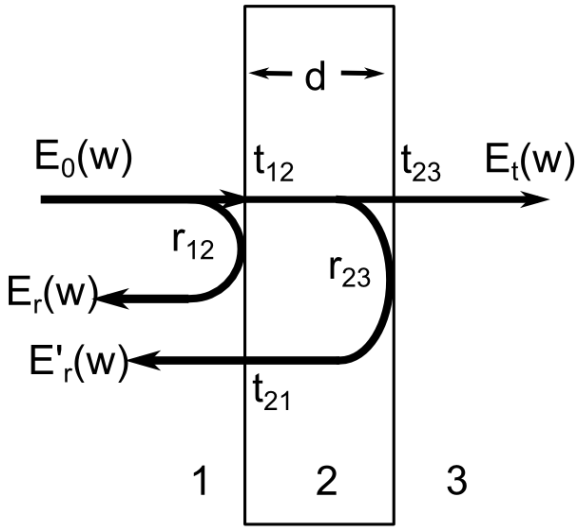

Figure 7. Schematic illustration of the geometries for transmission and reflection spectroscopy. $E_0(\omega)$ is the incident field, $E_t(\omega)$ is the transmitted field, $E_r(\omega)$ and $E'_r(\omega)$ are field reflected from the first and the second air/sample interface, t and r are Fresnel transmission and reflection coefficients, d – sample thickness (adopted from [73]).

These calculations are used for thick samples. During the experiment, the reference pulse electric field $E_{ref}(t)$ and the sample pulse electric field $E_{sam}(t)$ were measured. When fast Fourier transformation is performed, the result is $E_{ref}(\omega)$ and $E_{sam}(\omega)$ – spectral representation of reference and sample pulses in time-domain. Moreover, we can extract information about phase changes. The ratio of the complex field is [73,74]:

$$\frac{E_{sam}(\omega)}{E_{ref}(\omega)} = T(\omega)e^{i\Delta\varphi(\omega)} = t_{12}t_{23}e^{-\frac{\alpha d}{2}}e^{\frac{i(n-1)\omega d}{c}} \quad (7)$$

where d is the thickness of the sample, ω is the frequency of the radiation, c is speed of light in vacuum and $T(\omega)$ is a factor which accounts for the losses due to reflection on the sample surfaces, $\Delta\varphi(\omega)$ is the phase change, t_{12},t_{23} - complex Fresnel field transmission coefficients. The complex refractive index $\hat{n}(\omega) = n(\omega) + \kappa(\omega)$, and the absorption coefficient of the sample α without using Kramers-Kronig relations are calculated from the experimentally obtained $T(\omega)$ and $\Delta\varphi(\omega)$. The extinction coefficient $\kappa(\omega)$ is related to the absorption coefficient $\kappa(\omega) = \alpha(\omega)\, c / 2\omega$. If material absorption coefficient is low then the Fresnel transmission coefficients are real values, and $n(\omega)$ and $\alpha(\omega)$ can be calculated as [73]:

$$n(\omega) = 1 + \frac{\varphi(\omega)c}{\omega d}, \qquad \alpha(\omega) = -\frac{2}{d}\ln\left(\frac{(n+1)^2}{4n}T(\omega)\right). \tag{8}$$

For thin samples, where multiple reflections occur, Duvillaret *et al.* [75] suggested another calculation method which includes the Fabry-Perot factor $FP(\omega)$ and complex Fresnel transmission coefficients in data analysis:

$$\hat{T}(\omega) = \frac{\hat{E}_{sam}(\omega)}{\hat{E}_{ref}(\omega)} = \frac{4\hat{n}}{(\hat{n}+1)^2} e^{-\frac{\alpha d}{2}} e^{\frac{in\omega d}{c}} FP(\omega), \tag{9}$$

where

$$FP(\omega) = \frac{1}{1 - \left(\frac{\hat{n}-1}{\hat{n}+1}\right) e^{-\alpha d} e^{2in\omega d/c}}. \tag{10}$$

The solution requires an iterative procedure. Duvillaret *et al.* in [75] show a solution for both a thick sample, where Fabry-Perot echoes a separate and for a thin sample where Fabry-Perot echoes overlays. In [76] Duvillaret *et al.*

demonstrate a precise method of sample thickness determination using the THz-TDS technique. Sample thickness is then used in the determination of the refractive index and it is important to determine the most precise value.

The refractive index can be converted into the relative dielectric constant. The dielectric function $\varepsilon(\omega)$ and the complex conductivity $\sigma(\omega)$ are determined through the following relationship [77]:

$$\varepsilon(\omega) = n^2(\omega) = \varepsilon_{dc} + i\frac{\sigma(\omega)}{\varepsilon_0 \omega}, \tag{11}$$

where ε_{dc} is sample dielectric constant. The fitting process is iterative. Some fitting parameter values are selected. Then they are iteratively modified till the difference between the measured and the calculated values is minimized.

The contribution of the free carriers in semiconductors to the properties of the material at wavelength below the bandgap is determined by the intraband transitions of the partially filled band. Omitting the restoring force of the free carriers, this leads to the simple Drude model for which the complex conductivity $\sigma(\omega)$ is related to the concentration of the carrier N and the mobility μ [77]:

$$\sigma(\omega) = \frac{\varepsilon_0 \omega_p^2 \tau_0}{1 - i\omega\tau_0}, \tag{12}$$

where ω_p is the plasma frequency $\omega_p^2 = \frac{Ne^2}{\varepsilon_0 m^*}$ and τ_0 is the relaxation time $\tau_0 = \frac{\mu m^*}{e}$, where m^* is the effective electron mass. Free carriers are independent in this model and there are no interactions between them except collisions. The time between collisions is set at rate of $\Gamma = 1/\tau_0$. Therefore, the plasma frequency, the concentration of free carriers and their mobility can be extracted from the THz-TDS measurement.

The Drude model is quite simplified and is works well when the sample is large enough (bulk semiconductor). If we study the sample with nanostructures, the Drude model is inaccurate and more comprehensive (extended Drude) models like the plasmon model or the Drude-Smith model are used in such cases [73,78]. The Drude-Smith model includes carrier backscattering:

$$\widehat{\sigma}(\omega) = \frac{Ne^2\tau/m_{eff}}{(1-i\omega\tau)}\left[1+\sum_{n=1}^{\infty}\frac{c_n}{(1-i\omega\tau)^n}\right], \tag{13}$$

where N is the carrier density, τ is the carrier scattering time, c_n is backscattering parameter for the n -th collision. The first term is usually taken (n = 1). When c = 0, we get the simple Drude model, and when c = -1 we get a fully localized response, an equivalent to the overdumped oscillator.

The first measurements of the refractive index and the absorption coefficient in THz range using the THz-TDS setup were taken by D. Grischkowsky and coworkers [7,72]. They measured absorption coefficient and refractive index of dielectrics like: Crystalline Sapphire, Crystalline Quartz and Fused Silica: also in crystalline semiconductors like: Silicon, Germanium and Gallium Arsenide. Their measurements were compared with the result from other groups obtained using Fourier-transform spectroscopy (FTS or Fourier transform infrared spectroscopy (FTIR)). They show that the THz time domain spectroscopy is capable to measuring same data as the FTIR but with higher precision. This was the start of THz range exploitation in spectroscopy. They found that Crystalline Silicon is almost transparent for THz radiation (absorption coefficient was 0.05 cm^{-1}) and the index of refraction is changing by less than 0.001. These results have shown that Silicon is the ideal material for THz optics. It is used in THz emitters and detectors with photoconductive antennas

as lenses for better THz coupling from antenna substrates. Also, it can be used as THz beam splitter or THz filter.

The n-type InSb samples were studied with THz-TDs system in transmission and reflection geometries at various temperatures by Adomavičius *at al*. [15]. The reflection and transmission spectra were fitted with Drude model. The electron scattering time was used as a fitting parameter while the plasma frequency was a constant. The fitting result was not in good agreement with measurements results, until the nonparabolicity of the electron energy dispersion of the conduction band in InSb was taken into account. The effective mass and the plasma frequency depend on the electron energy. The electron scattering time dependence on temperature (from 15 K to 240 K) in InSb was measured using THz-TDS setup. A clear maximum at ~60 K was measured and explained by the presence of two electron scattering mechanisms. At low temperatures (till ~60 K) the electron scattering time increases due to ionized impurities scattering. However, in temperature interval from 60 K till 300 K the electron scattering time decreases due to the phonon scattering.

2.2.3 Pump – Probe experiments

This subsection will discuss implementation of the pump probe technique in THz spectroscopy measurements. This technique is used for the investigation of carrier dynamic processes in semiconductor materials. THz - TDS provide information about transient electric field. The pump – probe technique is utilized, to measure the dynamic response of carriers to external excitation. The main idea of the optical pump - optical probe measurement technique is that there are two pulses. More powerful pump pulse, which excites free carriers in semiconductor material, and less powerful probe pulse, this pulse examines sample’s optical response and provides dynamic information by

changing the delay time between pump and probe pulses. Two types of this technique are used in THz spectroscopy: Optical pump - THz probe and THz pump – THz probe.

Optical Pump -THz Probe

Optical pump – THz probe measurements are also called Time-resolved THz spectroscopy (TRTS). Its setup is shown in Figure 8. It differs from the conventional transmission geometry THz-TDS setup in that the laser beam in the TRTS setup is divided in to three parts and the third pulse directly illuminates the sample collinearly with the THz pulse. It is very important that the optical pump beam illuminates the sample homogeneously and that the overlap between the optical beam and the THz probe were as good as possible. For that reason before the sample an aperture is placed. The delay between the pump beam and THz probe pulses is implemented by using a second delay line stage.

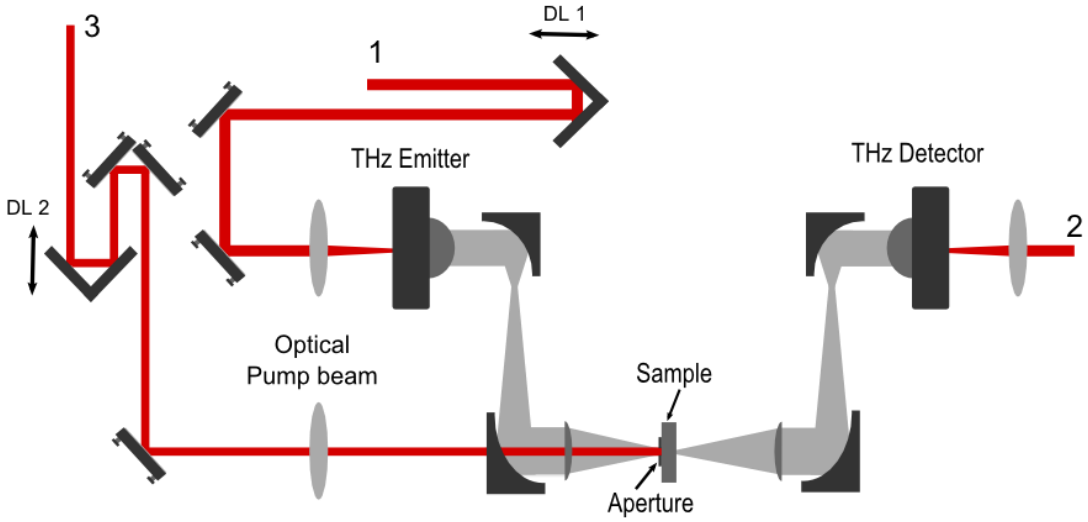

Figure 8. Optical pump THz probe in the transmission geometry setup with the photoconductive THz emitter and detector. The laser pulse is divided into three parts, first (1) is used for the THz emitter, second (2) - for the THz detector and third (3) – for the optical pump. DL 1 – first delay line is used for the THz

pulse scan, DL 2 – second delay line is used for dynamics measurements.

It is difficult to produce high densities of excitation on a sample when oscillator-based laser systems are used, because one cannot tightly focus the optical beam due to the THz beam spot size (the pump beam should be large). The small excitation densities induce small relative changes in the terahertz transmittance and a very sensitive photoconductive antennas-based THz emitter - receiver system is needed to detect such small changes. Moreover, only several groups worldwide have such systems, based on the oscillator laser and photoconductive THz emitter [32,33]. Most other groups use amplified laser systems with ZnTe electrooptic crystals for THz generation and detection.

The TRTS setup has two delay lines. Therefore, there are several modes of measurement, which produce two types of information shown in Figure 9.

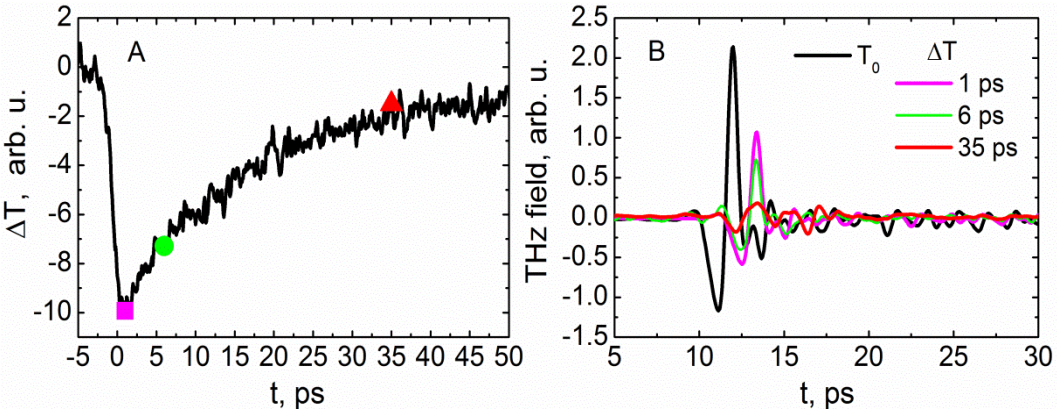

Figure 9. Two types of result can be obtained from the Optical pump - THz probe measurement. A - photoexcited carrier dynamics, B – a THz field scan with additional photoexcitation with different delays between the optical pump and THz probe pulses.

During the first measurement mode, the first delay line (DL 1) is fixed at position where the THz pulse electric field has a maximum value. During measurement we change the delay between the optical pump and the THz probe pulses by moving the second delay line (DL 2) and registering THz

pulse transmission changes because of the optical pump induced absorption. The changes in the THz peak transmission are measured as a function of delay between the optical pump – THz probe pulse in the form of dynamic of the photoexcited carriers (see Figure 9a). In literature, this measurement mode is also called a *1D scan*. Another type of measurement, called *2D scan*, is similar to THz-TDS measurement, but accomplished with additional optical excitation (see Figure 9b). During measurement, two delay lines are used for this scan. It can be *partial 2D* or *full 2D scan*. During *partial 2D scan*, the entire THz pulse scan is performed with several delay values between the optical pump and the THz probe pulses (DL 2 positions). Whereas the *full 2D scan* at each DL 2 position changes performs an entire THz pulse scan. It takes some time to perform the measurement, but it provides the most information, both dynamic and spectral [73,84].

When an optical pump pulse hits the sample, the free carriers are induced. Transmission of the THz radiation due to free carrier absorption is reduced. Free carrier absorption affects the complex dielectric permittivity changes in a sample. Therefore, the transmission of THz radiation decreases. By changing the delay between the optical pump and the THz probe pulses, the changes in the complex dielectric permittivity $\Delta\sigma$ [79] of a sample can be measured.

If optically induced free carriers are form a thin layer d on a semi insulating semiconductor surface and $d << \delta < \lambda_{THz}$, then measured negative differential transmission $-\Delta T/T$ can be expressed in the following way [73,79]:

$$-\frac{\Delta T}{T} \sim \frac{Z_0 \sigma d}{1+n}; \tag{14}$$

If $\sigma = Ne\mu$, then:

$$-\frac{\Delta T}{T} \sim \frac{Z_0 N e \mu d}{1+n}, \quad (15)$$

where δ is the pump beam penetration depth, λ_{THz} – the THz pulse wavelength, Z_0 – the impedance of free space (377 Ω), σ - the conductivity of a sample, n – the sample index of refraction, N – the free carrier density, e – electron charge, μ - free carrier mobility. By using the (15) formula, useful parameters of material like induced free carrier density N, induced free carriers mobility μ and free carrier's lifetime τ can be determine form negative differential transmission measurements. This means that in same condition measured parameters (N, μ, τ) can be compared between the materials with similar optical and THz properties.

TRTS measurements cannot distinguish difference between electrons and holes. Since the effective mass of heavy holes is usually several times larger than the effective mass of electrons and the THz pulses are non resonant with the semiconductor band gap, it can be concluded that, with the help of the optical pump - THz probe technique one would be able to study induced free electron dynamics in semiconductor materials [73]. Induced free carrier densities in optical pump - THz probe measurement are of the order of 10^{15} cm^{-3} - 10^{16} cm^{-3} - this is lower densities than in typical all optical pulse pump-probe measurements, nevertheless it is still possible to probe carrier transport phenomena with a femtosecond temporal resolution [80,84]. Also, this technique can be used to study materials which are difficult to investigate with traditional methods, for example for studying materials with nanostructures [8].

The optical pump – THz probe technique is used in the majority of publications to study the lifetime of induced free carriers in semiconductor materials, which were used for the production of the terahertz emitters or

detectors. Free carrier lifetime value is extracted by fitting the experimental data, which was recorded during *1D scan* (see Figure 9b), with one or two exponent function. The first material that was studied using the TRTS technique was GaAs [81], since it was the most popular and well studied material. THz radiation was generated in $LiTa0_3$ crystal in form of Cherenkov cone radiation in this experiment [82], and the authors were able to directly observe the transfer of electrons from the low mobility *L* and *X* valleys in GaAs to the higher mobility *Γ* valley on a 2-3 ps time scale following the optical injection being well above the bandgap [81]. After that and several other publications released by Jepsen *et al.* [83] and Schmuttenmear *et al.* [8,84] GaAs became the etalon sample for TRTS setup calibration.

Induced free carrier lifetime dynamics were also studied in GaAsBi, GaAsN [85], Ge [86], Ge nanowires [87], InP [88,89], ZnTe and CdTe [90] and some other materials.

The optical pump - THz probe technique is also suitable for studying intervalley scattering and energy relaxation times in semiconductor materials. Samples for such a purpose should be excited with energies above the bandgap. The effective mass of electrons is higher and mobility is lower in upper valleys than in *Γ* valley. This property affects the transmission of the THz radiation because of free carrier absorption and is evident in the measurements results of carrier dynamic. The first experiment of this kind, using, a GaAs sample, was performed by Nuss *et al.* [81]. They used a 625 nm laser to induce carriers in-to the higher valley. Nowadays, most groups use the Ti: sapphire laser system, the energy quant of which is ~ 1.5 eV. Therefore, it is possible to study the intervalley scattering processes in narrow bandgap semiconductor materials. The first of such studies was performed in Ge samples [14] and $In_{0.53}Ga_{0.47}As$ [80]. The intervalley scattering to *Δ* valleys

time in Ge sample was determined to be of the subpicosecond order, and caused the reduction of the electron mobility. The intervalley scattering time in $In_{0.53}Ga_{0.47}As$ was determined to be 350 fs.

THz pump - THz probe

The THz pump – THz probe is a high electric field pump probe technique used to study the dynamics of carriers in semiconductor materials. Hot electrons are generated by high power THz pulses (pulse intensities can reach 150 MW/cm^2) when utilizing this technique. Such THz pulses can create high strength (up to 150 kV/cm) electric fields on the surfaces of the semiconductor materials. This technique is used by group of M. Hoffmann *et al.* [10,91,92]. An advantage of this technique is that it eliminates direct optical electron-hole generation, which complicates the analysis of optical pump – THz probe measurement results. However, this technique requires high power laser systems, which are expensive.

Figure 10 illustrates the THz pump - THz probe setup in transmission geometry. High power THz pulses are generated by optical rectification in the $LiNbO_3$ crystal by utilizing the tilted pulse front method, which enables the generation of large THz field amplitudes using high power femtosecond laser pulses without unwanted nonlinear optical effects. The 800 nm, 100 fs pulse duration, 1 kHz repetition rate, 5 mJ pulse energy regeneratively amplified Ti:sapphire laser system was used in this setup. The laser pulse was divided in to three parts. 86% of the laser's power was used to generate THz pump pulses, 10% were used to generate THz probe pulses, and 4% - were used for EO sampling. A compound ZnTe detector with 0.1 mm active layer and total thickness of 1.1 mm was used for THz detection. THz pump and THz probe pulses were spatially delayed using the delay line stage. THz pulses were

collinearly routed and focused on to the surface of a sample by means of a pair of parabolic mirrors.

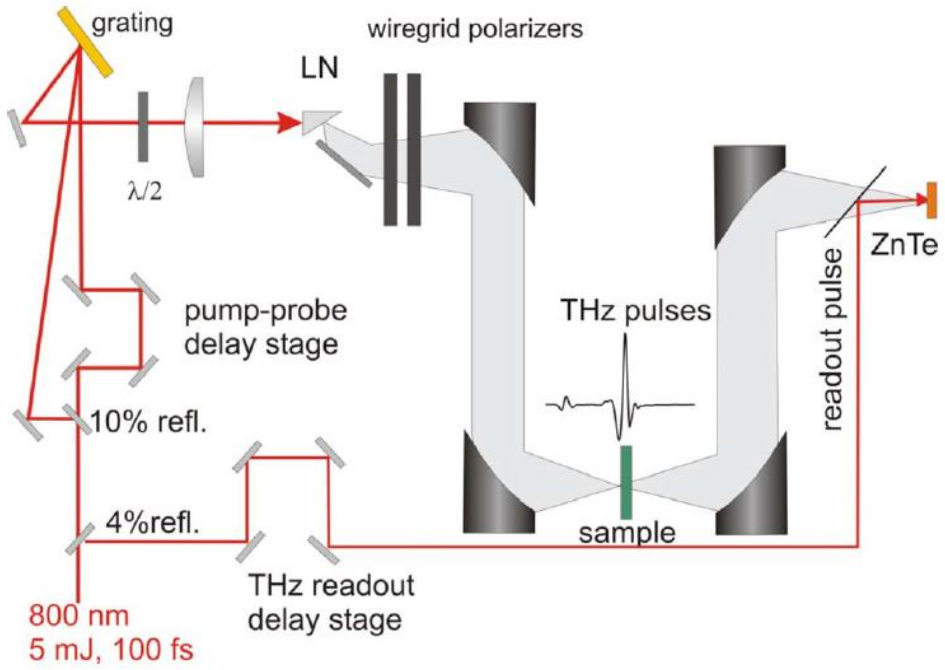

Figure 10. THz pump – THz probe setup. THz pulses are generated in $LiNbO_3$ by tilted pulse front excitation and detected by electro-optic sampling in ZnTe crystal (Adopted form [10]).

Nonlinear THz transmission measurements were performed during the experiment. The authors measured the THz field with ($E_{sam}(t)$) and without ($E_{ref}(t)$) the sample in at the path of the THz beam and calculated the effective absorption coefficient [10]:

$$\alpha_{eff} = -\frac{1}{d}\ln\left(T^2\frac{\int_0^{t_{max}} E_{sam}^2(t)dt}{\int_0^{t_{max}} E_{ref}^2(t)dt}\right), \quad (16)$$

where d – is the thickness of the sample, t_{max} – is the time window of the measurement, T – is the factor accounting for reflection losses at the sample

surface, α_{eff} – is the equivalent to the energy absorption coefficient averaged over the bandwidth of a measurement setup.

Several popular semiconductor materials like: GaAs [10,92], Si, Ge [92] and InSb [10,91] were studied using this technique.

2.2.4 Applications of surface THz emission in semiconductor characterization

The method of THz generation from surfaces of the semiconductors can be used for investigating several important material characteristics. Dependences of surface generated THz pulse amplitude on the femtosecond laser photon energy were used for characterizing conduction band structure at higher energies. It is possible to study intervalley scattering effects, evaluate the energy position of the subsidiary conduction band valleys [93] and measure THz excitation spectra [16] of semiconductor materials using tunable wavelength lasers system for THz generation from the surface of semiconductor. The whole range of semiconductor materials was studied using this technique: InAs [16,93], InSb [16,93], InGaAs [94], InN [16], GaAs [16].

The amplitude of THz pulses can also be used for mapping the built-in surface electric field in semiconductors. The built-in surface electric field and fast carrier separation are the main parameter of thin-film photovoltaic solar cells. $CuInSe_2$ (CIS) and $Cu(InGa)Se_2$ (CIGS) are semiconducting materials, which are used for the production of thin-film photovoltaic solar cells, and their efficiency reaches 20% [95,96]. So, THz generation from the surface of thin-film CIS and CIGS samples can be used for study built-in surface electric field in these materials [97,98], which can help to increase efficiency of thin-film photovoltaic solar cells. R. Adomavičius *et al.* have studied several CIS and CIGS samples from different manufacturers and of different composition [97].

The results have showed that CIS and CIGS samples can generate THz radiation. The THz pulse electric field amplitude of the best samples was comparable with the THz pulse electric field amplitude from surface of n-type GaAs, and was two times worse than p-InAs. They have also showed that the THz pulse electric field amplitude depends on the composition of the sample. The Cu/In ratio is the main parameter upon which the open-circuit voltage of a CIS photovoltaic cell depends and this parameter should be close to 1[99].The most efficient THz emission was registered from samples with Cu/In ratio equal to 0.9 [97]. These samples also can be good THz surface emitters.

2.3 Experimental setups

During my work, I have used several experimental setups with different lasers and supplementary devices. In this subsection I will explain them in more detail.

2.3.1 THz – TDS

I have used conventional THz – TDS system with Ti:sapphire osciliator (Coherent Mira; λ = 800 nm, 76 MHz repetition rate, 150 fs pulse duration, 650 mW output power). Setup diagram is shown in Figure 11.

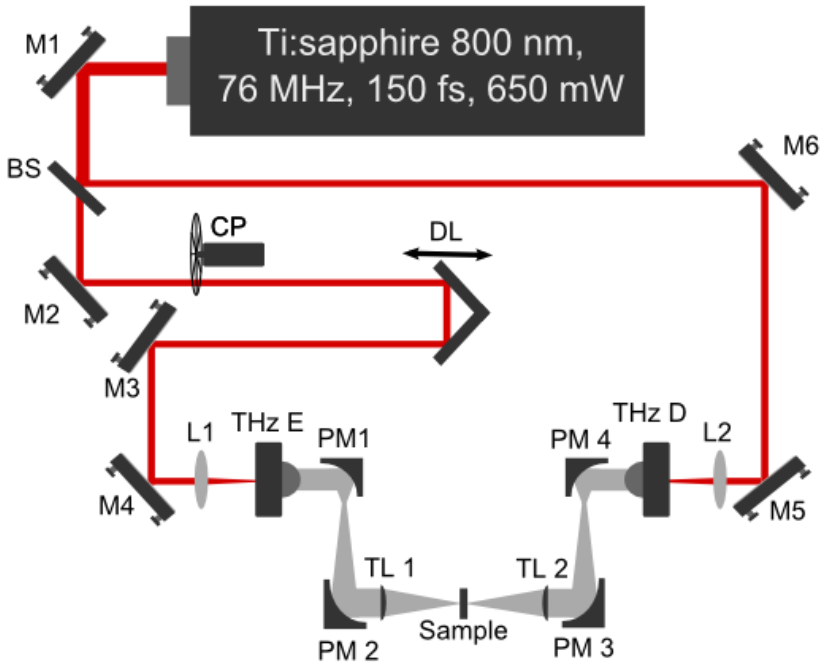

Figure 11. Terahertz time domain spectroscopy setup. BS – the beam splitter, CP - the mechanical copper, DL – the optical delay line, L1 - L2 - optical lenses, M1 - M6 - dielectric mirrors, PM 1 – PM 4 – parabolic gold mirrors, TL 1 – TL 2 - THz teflon lenses, THz E and THz D – the terahertz emitter and detector.

The laser pulse was split into two parts: one was used for activating photoconductive LTG GaAs THz emitter, and the other one for gating photoconductive LTG GaAs THz detector. 40 mW of the laser power was used to illuminate the photoconductive antenna gap of a THz emitter and the same amount to illuminate the photoconductive antenna gap of a THz detector. The THz emitter bias voltage was 50 V. The distance between the THz emitter and the THz detector was around 30 cm. Gold coated parabolic mirrors and Teflon lenses were used to focus and collimate the THz radiation. The sample was placed between the emitter and the detector. The terahertz pulse scanning was performed while moving the delay line (8MT175-100, Standa). The emitter excitation pulse was modulated with mechanical chopper (SRS SR540) at 1 kHz and the signal was registered with lock-in amplifier (SRS SR830).

2.3.2 THz surface emission

The THz emission experiments from the surface of semiconductor sample were performed using another Ti:sapphire oscillator (Femtolaser Femtosource Synergy; λ = 800 nm, 85 MHz pulse repetition rate, 20 fs pulse duration, 200 mW output power). Setup diagram is shown in Figure 12.

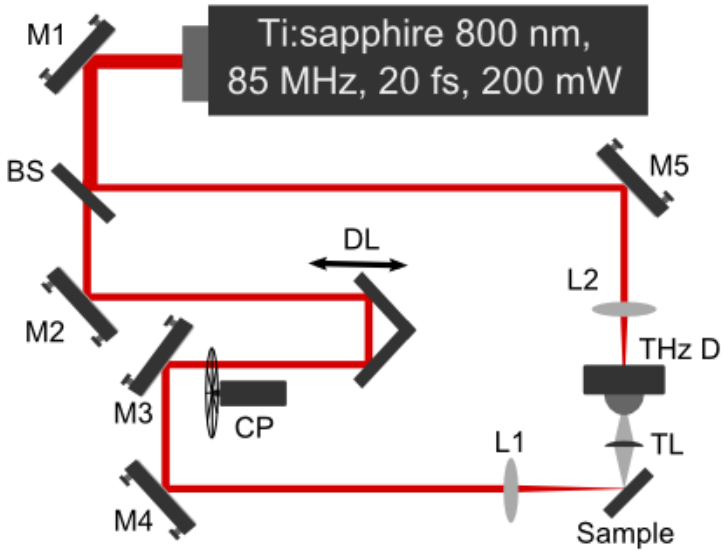

Figure 12. The THz emission from the surface of semiconductor setup. BS – the beam splitter, CP - position of the mechanical chopper, DL – the optical delay line, L1 - L2 - optical lenses, M1 - M5 - dielectric mirrors, TL - teflon lens, THz D – the THz detector.

The laser pulse was split into two beams via beam splitter. 30 mW of the laser power were used to illuminate the photoconductive antenna gap of a LTG GaAs THz detector, the remaining laser power was focused on a surface of a THz emitter. The focused laser beam width was less than 1 mm. The sample (or surface THz emitter) was placed in front of the THz detector at an angle of 45 degrees. The THz pulse was emitted along the direction of reflected optical excitation beam. The distance between the THz emitter and detector was about 15 - 20 cm. The Teflon lens was used to focus the THz radiation. The THz pulse scanning process was the same, as in previous setup. The emitter excitation pulse was modulated with mechanical chopper (SRS SR540) at 1 kHz and the signal was registered with lock-in amplifier (SRS SR830). The measured THz pulse amplitudes and spectra of different semiconductor materials were usually compared with the parameters of THz radiation emitted from surface of p-InAs sample, measured in same conditions. We perform this

comparison because p-InAs are the best surface THz emitter for 800 nm laser wavelengths.

2.3.3 Optical pump – THz probe

This setup is based on the THz-TDS setup that was described in section 2.3.1 and is shown in Figure 13.

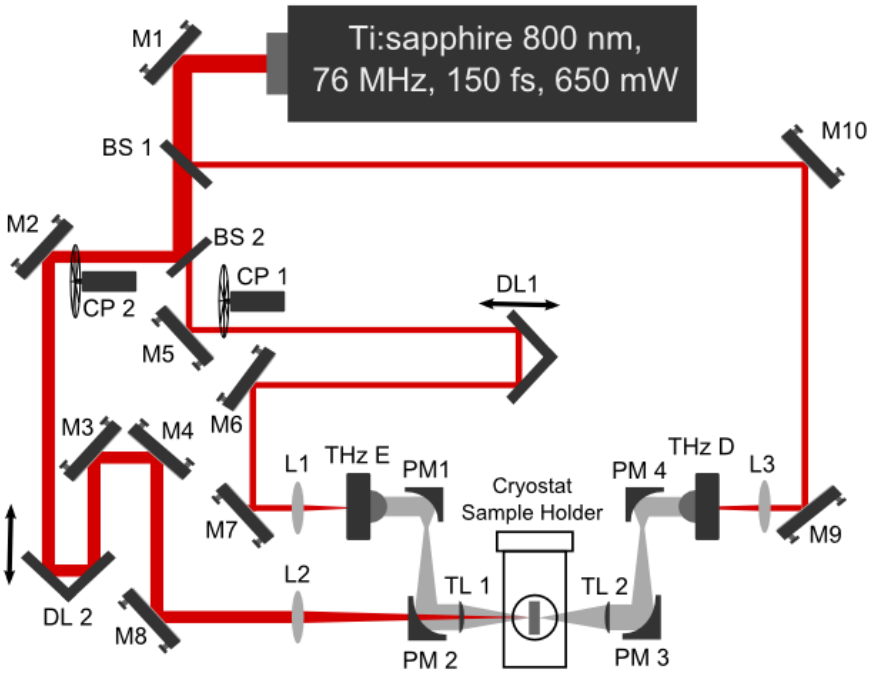

Figure 13. The optical pump - THz probe setup. BS 1 – BS 2 – the beam splitters, CP – positions of the mechanical chopper, DL – the optical delay lines, L 1 – L 3 - optical lenses, M 1 – M 10 - dielectric mirrors, PM 1 - PM 4 - parabolic gold mirrors, TL 1 - TL 2 - teflon lenses, THz E and THz D – the THz emitter and detector.

In this setup the laser beam was split in to three parts. The first laser beam part, which was most powerful, was used to directly illuminate the sample and create non equilibrium carriers in it. The generated carrier density was from 10^{16} to 10^{17} cm^{-3}. The second part of the laser pulse was used to illuminate photoconductive antenna gap of a LTG GaAs THz emitter, and third was used

to illuminate photoconductive antenna gap of a LTG GaAs THz detector. The delay between different laser beams was controlled with help of two optical delay lines (8MT175-100, Standa). To achieve more homogenous sample excitation the optical pump and the THz probe beams should propagate in the same direction and completely overlap on the surface of a sample. Therefore, the optical pump beam was passed through holes in the parabolic mirror (PM 2) and the Teflon lens (TL 1) and sample was placed on a holder with a 300 μm aperture. For temperature dependent measurements the sample was places in a close circle liquid helium cryostat (CRYO Industries CTI M-22). It allows reduce sample temperature up to 11 K. This setup can be used as TDS setup when chopper is in the first position (CP 1). During the scan, the sample is placed between the THz emitter and detector. Mechanical chopper is placed to the first position (CP 1). Moving the first delay line (DL 1) we find the THz signal maximum. Then the mechanical chopper is placed to the second position (CP 2) and by moving the second delay line (DL 2) the scan was performed at the signal maximum. In this experiment, we need to do two measurements with and without a THz probe signal. After that we need to subtract the result of the second measurement from the first one. This procedure helps to eliminate the THz signal that is generated by the sample when it is excited with the optical pump beam.

2.3.4 Optical pump – optical probe

The optical pump - optical probe setup is shown in Figure 14. In this setup an amplified Yb:KGW laser system (Pharos, Light Conversion; 1030 nm wavelength, 160 fs optical pulses duration, 200 kHz pulse repetition rate). The laser radiation (≈6 W) was directed to the optical parametric amplifier (Orpheus, Light Conversion) which generates tunable 640 - 2600 nm wavelength and approximately 140 - 160 fs duration pulses.

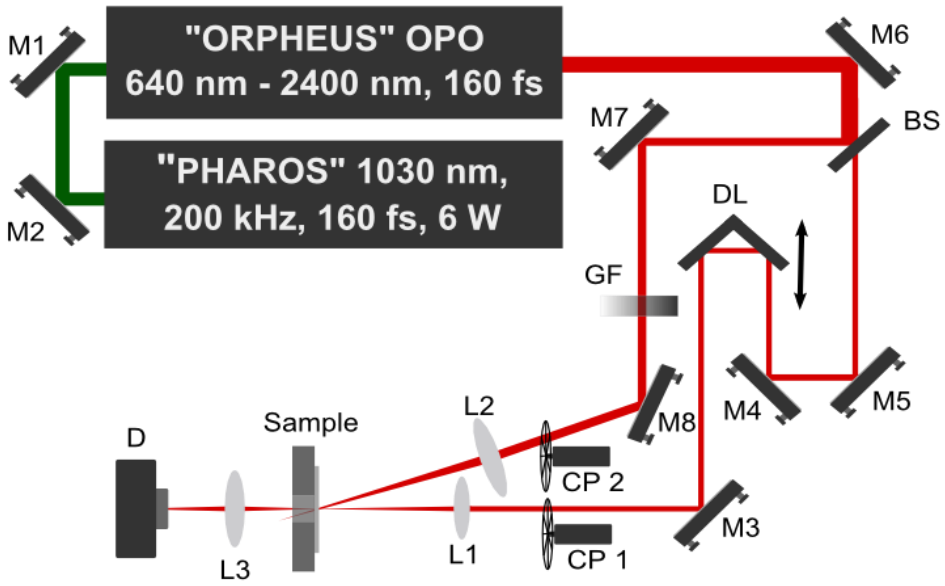

Figure 14. The optical pump - optical probe setup. BS – the beam splitter, CP - position of the mechanical chopper, DL – optical delay line, D - optical detector, L1 - L3 optical lenses, M1 - M8 gold mirrors, GF – the gradient neutral filter.

As in the optical pump – THz probe setup, the laser beam was split in to two beams: the pump and the probe beams. The pump beam is more powerful because its purpose is to induce free carries in the sample. The probe beam is less powerful and it is used to probe the induced free carriers relaxation processes in a sample. The transmission geometry scheme was used. The probe beam was directed straight to the sample. After beam passes through the sample it was pointed to a big aperture Ge detector. Later on, to get a better signal to noise ratio, a liquid nitrogen cooled InSb detector was used. The pump beam was directed to the sample at a small angle of less than 30º to avoid the pump beam reaching the detector. The pump and probe beams were tightly focused on a surface of a sample by means of optical lenses. The probe beam spot diameter was smaller than the spot diameter of a pump beam. The optical delay line (8MT175-100, Standa) was used for the scan procedure. The

detector output was connected to a lock-in synchronous amplifier (SRS SR830), and mechanical chopper (SRS SR540) was used for a synchronous detection. Depending on a measurement phase, the mechanical chopper position was either on the pump or either on the probe beam. The gradient neutral filter was used to control the pump beam intensity.

2.4 Summary

- THz radiation pulses can be generated using photoconductive antennas or surface emitters and detected by coherent or non-coherent techniques.
- THz – TDS provide information about the THz signal amplitude and phase. Using this information, the absorption coefficient ant the complex refractive index can be extracted without using Kramers-Kronig relations.
- Sample complex conductivity and the dielectric function can be calculated from measurement results and calculation results are in good agreement with the Drude theory.
- Important material parameters: plasma frequency, current carrier mobility and density as well as electron momentum relaxation time can be determined
- The optical pump – THz probe technique is used to study induced free carrier lifetime, intervalley scattering and energy relaxation times.
- All these techniques are widely used to study parameters of semiconductor materials.

3. Study of GaAsBi properties

3.1 Annealed GaAsBi

Semiconductor industry is continuously searching for new materials with energy bandgap in the near-infrared spectral range and with close lattice match to GaAs for optoelectronic and optical communication devices, photovoltaic technologies, and, recently, to the components for terahertz (THz) spectroscopy systems. During the last years attention was paid to dilute bismides materials. A $GaAs_{1-x}Bi_x$ alloy is the most promising and widely studied material for these applications [100,101]. $GaAs_{1-x}Bi_x$ bandgap is reduced when Bi is incorporated in to GaAs lattice, about 90 meV per 1% of Bi atoms and becomes equal to 0.75 eV when 11% of Bi is incorporated. Also this alloy has E_g and refractive index that are less sensitive to the changes of ambient temperature [102]. This feature would be useful for the applications such as diode lasers and optical modulators. Short characteristic carrier lifetime in this alloy make it also a promising material for THz emitters and detectors. Therefore studies of the influence of technological conditions to the properties of GaAsBi material characteristics are very important.

Rapid thermal annealing (RTA) is a simple and popular process, which is used to improve the crystalline structure and decrease defect and dislocation amount in as-grown layers. However, influence of this process to the bismide properties is little studied. There are some unanswered questions about the mechanisms of the carrier recombination and the lifetime dynamics in $GaAs_{1-x}Bi_x$. The understanding of the physics of these processes can help the development of GaAsBi-based devices.

3.1.1 Samples

The GaAsBi samples we grown in the Optoelectronic Technology Laboratory of the Center for Physical Sciences and Technology by Dr. Klemensas Bertulis. The sample parameters are presented in Table 1.

Table 1. Studied $GaAs_{1-x}Bi_x$ sample parameters.

Sample Name	Substrate (orientation)	Thickness (μm)	Bi (%)	E_g (eV)
Sample A	GaAs (100)	1.5	4	1.15
Sample B	GaAs (100)	1.5	6	1.05

The epitaxial layers were grown in a solid-state MBE system on semi-insulating GaAs (100) substrates. A metallic Ga and Bi sources and an As_4 molecular source were used. The substrate temperature was 330 ºC. It is lower than traditional GaAs growth temperature by MBE of ~600 ºC. This prevents the Bi segregation and induces better bismuth incorporation. The growth rate was ∼1 μm h^{-1}, and a As/Ga beam equivalent pressure (BEP) ratio was ∼2. The layers were 1.5 μm thick. The energy bandgap of the as-grown layers determined from the optical absorption spectra at room temperature was of the order of 1.05–1.15 eV, which corresponded to the Bi compositions x between 0.04 and 0.06 [103]. All samples were annealed in RTA oven for 30 s at different temperatures up to 700 ºC under nitrogen atmosphere.

3.1.2 Measurement techniques

The samples were investigated using several techniques: photoluminescence (PL) and photomodulated transmittance (PT) measurements at room and liquid nitrogen temperatures and optical pump –THz probe.

Optical pump – THz probe technique was used to study carrier dynamics in $GaAs_{1-x}Bi_x$ epilayers. The used setup was introduced in 2.3.3 subsection. The photoinduced carrier density was of the order of 10^{16} cm^{-3}. During the measurement, the samples were placed in a closed cycle liquid helium cryostat, where the sample temperature was changed from 295 K room temperature (RT) to 11 K.

Photoluminescence measurements were performed using green DPSS laser (473 nm) with an excitation intensity of 10 Wcm^{-2} and 0.4 m monochromator. Photomodulated transmittance measurements were performed by using the DPSS laser (473 nm) as the pumping source. A 100 W tungsten halogen lamp filtered by 0.4 m monochromator providing monochromatic light. Transmitted light was detected by a thermoelectrically cooled InGaAs photodetector and the signal was recorded by a lock-in amplifier. The chopping frequency of the pump beam was set to 190 Hz. Measurements were made at room (295 K) and liquid nitrogen (80 K) temperatures.

3.1.3 Measurement results

First of all, carrier dynamics measurements were performed using optical pump – THz probe technique. Measurements were done at room temperature. Samples with 4% and 6% Bi atom concentration as-grown and annealed at 600 ºC temperatures were compared. Results are shown in Figure 15.

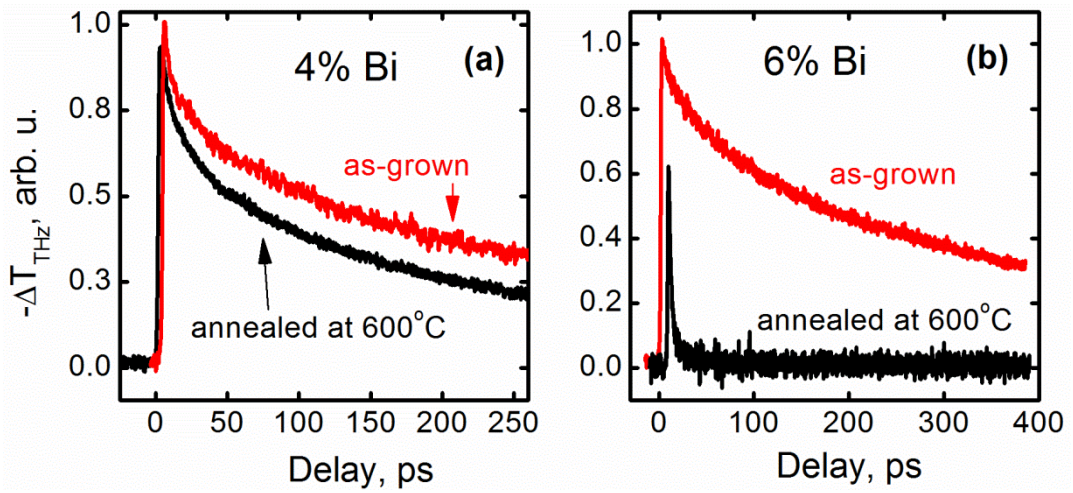

Figure 15. GaAsBi optically induced THz transmission changes measurements made at room temperature. Bi atom concentrations: 4% (a) and 6% (b).

Non-equilibrium carrier decay times were determined from obtained measurement results by using an exponential fit. A two-exponential decay function was used for fitting, because all curves have ultrafast part in the beginning and slowly varying exponential tail.

As it is seen from measurement results, the non-equilibrium carrier lifetimes in both as-grown samples are similar and show relatively slow decay. The annealing in RTA oven has a dual effect on non-equilibrium carrier lifetime. In the sample with 4% Bi this time has changed slightly (see Figure 15a), whereas in the sample with 6% of Bi atom concentration non-equilibrium carrier lifetime was strongly reduced by the annealing and became as short as several picoseconds making it useful for THz emitter and detector fabrication [104].

Then non-equilibrium carrier decay time dependence on the temperature was measured. As-grown and annealed at 650 ºC samples were used in these experiments. The results are presented Figure 16.

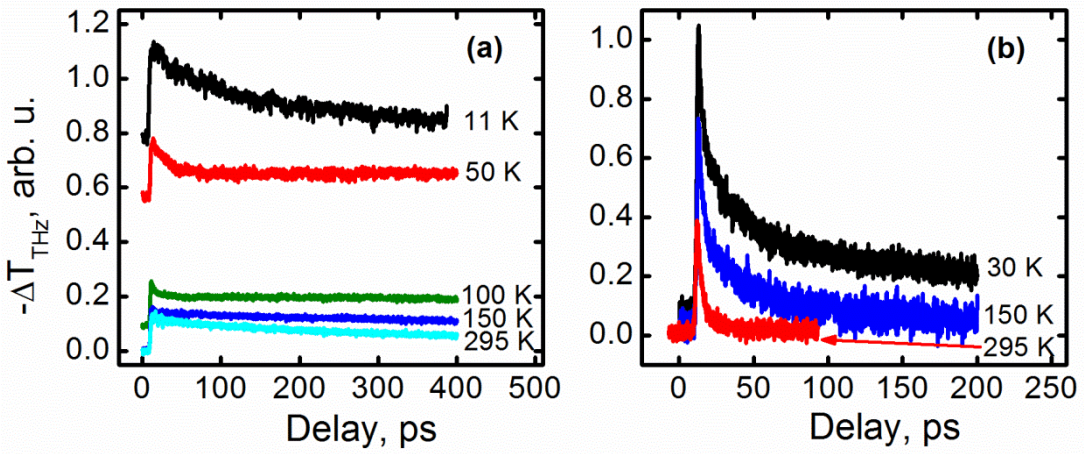

Figure 16. The optically induced THz transmission changes dependence on sample temperature. Sample with 6% of Bi atom: (a) as-grown, (b) anneal at 650 ºC.

Measured temperature dependence of the optical induced THz transmission change show that samples A and B behave differently in low temperature range as well.

Lowering the temperature of as-grown and annealed sample A and as-grown sample B resulted in the increase of the decay time and the appearance of a large optically induced background of THz absorption component. The growth of the background THz absorption component became significant at lower than 100 K temperatures. This evidences that the non-equilibrium carrier lifetime became comparable or larger than the pulse repetition period of 13 ns of the used Ti:sapphire oscillator. On the other hand, the non-equilibrium carrier recombination time in the samples made from layer B and annealed at temperatures exceeding 600 ºC remains short even at the lowest temperature, although a slower decay component becomes observable at T < 150 K. The optically induced background level in this case is much smaller than in the samples with long carrier lifetimes.

The photoluminescence (PL) and photomodulated transmittance (PT) studies of sample B were performed at room (RT) and liquid nitrogen temperatures. Results are shown in Figure 17.

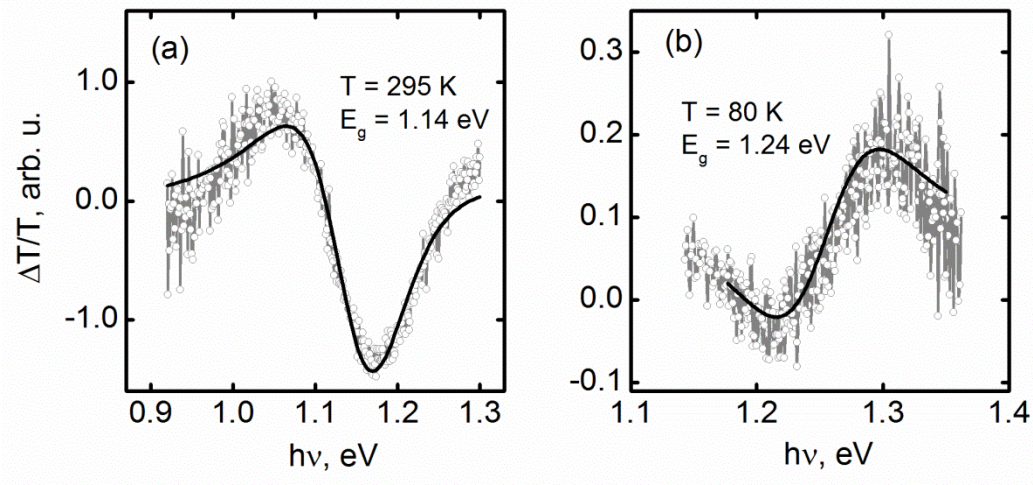

Figure 17. Photomodulated transmittance spectra and their low electrical field modulation fits (17) for sample B at room (a) and liquid nitrogen (b) temperatures. The energy bandgaps E_g = 1.14 eV and E_g = 1.24 eV were determined for temperatures 295 K and 80 K, respectively.

PT spectra were fitted by a line shape function for low electrical field modulation [105]:

$$\frac{\Delta T}{T} = Re\left\{\frac{C \cdot e^{j\varphi}}{(E - E_g + j\Gamma)^m}\right\}, \tag{17}$$

where C and φ are the amplitude and phase of the PT feature, E_g – energy bandgap, Γ broadening parameter, m = 2.5 for a three-dimensional critical point. PT measurements show that E_g of sample B increases from 1.14 eV at RT to 1.24 eV at 80 K. Similar behavior was also noticed by other groups [106].

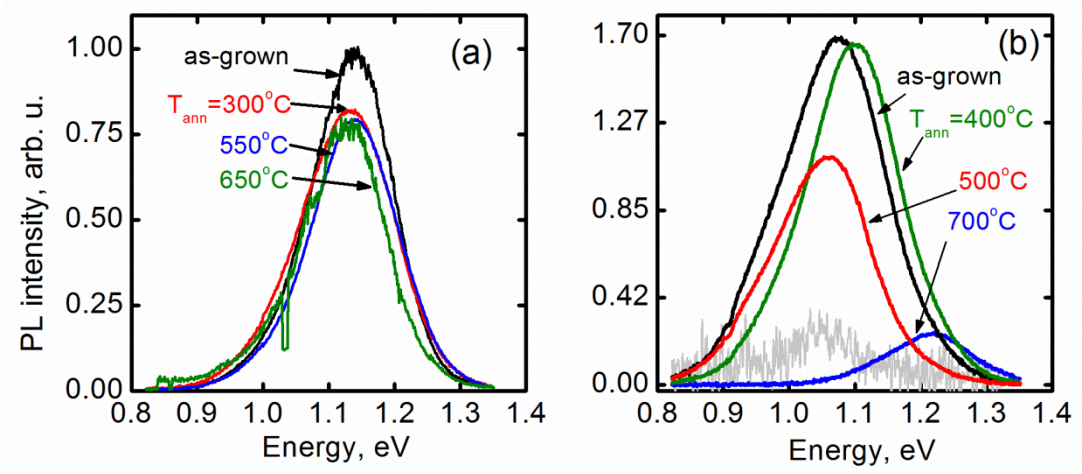

Figure 18. Photoluminescence spectra for as-grown and differently annealed samples: (a) sample A, (b) sample B. The curves with the indicated annealing temperatures correspond to the measurements made at 80 K; the gray curves at the bottom correspond to the measurements made at RT.

Photoluminescence measurements (see Figure 18) of both A and B samples demonstrates signal at room temperature but the signals at this temperature were weak. The PL peak position did not change after annealing for both samples when measured at 80 K, except for sample B annealed at 700 ºC. Its peak position shows a blue-shift, this is in line with the results obtained from PT measurements (see Figure 17b) which evidences that the bandgap energy increases at 80 K.

3.1.4 Discussion

It was determined in [107] that short non-equilibrium carrier lifetimes in $GaAs_{1-x}Bi_x$ at room temperatures is due to defect levels inside the bandgap of a material. These deep donor defect levels act as efficient recombination centers with a density of 10^{14} to 10^{15} cm^{-3} and an electron capture cross-section of $\sim 4 \cdot 10^{-13}$ cm^2. They can efficiently trap electrons while are ionized and then start capture the holes after becoming neutral. The origin of these

recombination centers in GaAsBi is not clear yet. However, they can occur in the layers with a larger Bi composition because a bigger lattice mismatch results in a larger density of structural defects. The density of structural defects could increase in a mismatched layer during high-temperature annealing.

The low temperature grown GaAsBi epilayer structure is similar to low temperature MBE grown GaAs, where short non-equilibrium carrier lifetimes appear due to As-antisites (As_{Ga}) inside the bandgap [108]. However, in GaAsBi an electron capture cross-section can be several times larger [107]. The evidence of As-antisites defects in $GaAs_{0.985}Bi_{0.015}$ epilayers was determined using optically detected magnetic resonance (ODBR) technique [109]. However, the samples investigated in this work were grown at 270 ºC temperature and only 1.5% of Bi was incorporated. After post-growth rapid thermal annealing at 600 ºC As_{Ga} defects concentration was reduced.

We introduce a model where, the optically induced background THz absorption component can be explained by taking in to account the presence of two defect levels inside the bandgap of the GaAsBi: the deep donor and the shallow acceptor defect levels. In GaAsBi the holes traps can be the bismuth pair and cluster states located near the valence band maximum [110]. The deep donors are responsible for recombination of both types of carriers, and shallow acceptors are determining the temperature dependences of the non-equilibrium electron and hole density.

The background THz absorption signal depends on steady state non-equilibrium carrier concentration accumulated during a period of time much longer than the time between two laser pump pulses. Since in this quasistationary state the rate of carrier recombination must be equal to the rate of their photoexcitation *G*, the electron and hole capture rates shall be equal to *G*:

$$G = n\sigma_e v_e(N_{D0} - N_D) = p\sigma_h v_h N_D \quad (18)$$

where n is the free electron concentration, p is the hole concentration in the valence band, v_e and v_h are the electron and hole thermal velocities, N_{D0} is the deep trap density, N_D is the number of those traps occupied by electrons, and σ_e, and σ_h are the capture cross section of these traps for electrons and holes, respectively. As the electron capture cross section is by two orders larger than the hole capture cross section, the electron and hole capture rates will become equal only when the majority of traps will be occupied:

$$N_D \approx N_{D0} \quad (19)$$

Non-equilibrium holes can be trapped by the shallow acceptor defect levels. Also, they can be thermally excited from acceptor band to the valence band; the rates of these processes in the steady state must be equal:

$$p\sigma_p v_p(N_{A0} - N_A) = N_A N_v \sigma_p v_p \exp\left(-\frac{\Delta E}{kT}\right) \quad (20)$$

where N_{A0} is the total shallow acceptor trap density, N_A is the number of them occupied by holes, σ_p is the hole trapping cross-section, N_v is the effective density of states in the valence band, k is the Boltzmann constant, T is the absolute temperature, and ΔE is the activation energy of the hole traps.

The shallow acceptor trap density dependence on temperature $N_A(T)$ can be derived from the equation (20):

$$N_A(T) = \frac{N_{A0}\frac{p}{N_v} exp\left(\frac{\Delta E}{kT}\right)}{1 + \frac{p}{N_v} exp\left(\frac{\Delta E}{kT}\right)} \quad (21)$$

At room temperature the majority of shallow acceptors are ionized and do not affect the hole concentration in the valence band; therefore, the influence of shallow acceptor traps to the carrier recombination is insignificant. The situation changes at low temperatures when a significant part of the free holes occupies the shallow acceptor level: the decreased free hole concentration p disturbs the balance between generation and recombination of the carriers. As a result, the concentrations n and p start to increase until p reaches its room temperature value (as $\sigma_h v_h N_D \approx$ const - only the increase of p can maintain the balance between generation and recombination), whereas n increases by value of N_A. The increase of the electron concentration Δn can be extracted from the optical pump - THz probe measurements, because the change of THz transmittance is directly proportional to the non-equilibrium electron concentration in the sample (the electron mobility is much higher than the hole mobility; therefore, we can neglect the hole contribution to the induced transmittance changes). The experimentally estimated Δn and the calculated N_A are presented in Figure 19. The best match between experimental results and theory was obtained with the following fitting parameters: ΔE = 50 meV, N_{A0} = $4 \cdot 10^{16}$ cm^{-3} and $p = 1 \cdot 10^{16}$ cm^{-3}.

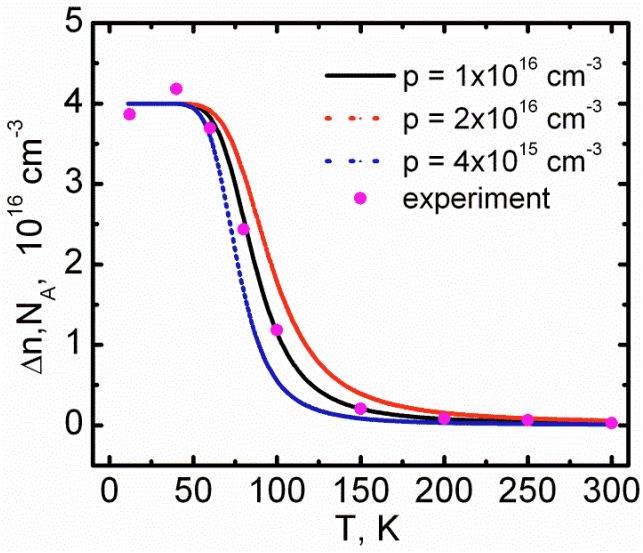

Figure 19. Temperature dependence of experimentally estimated electron concentration increment Δn fitted with calculated density N_A of the holes occupying shallow acceptor traps. The fitting parameter p denotes free hole concentration accumulated at room temperature under stationary state photoexcitation.

3.1.5 Conclusions

1. The rapid thermal annealing at temperatures up to 700 ºC has a dual effect on the electron decay characteristics of GaAsBi layers. For samples with 4% of Bi atoms it has minor changes, however for samples with 6% of Bi atoms the non-equilibrium carries lifetime is reduced to less than 1 ps.

2. The PL peak position for sample with 6% of Bi atom annealed at 700 ºC has a blue-shift, which is in line with the results obtained from PT measurements showing that the bandgap energy increases at 80 K.

3. The recombination centers in GaAsBi are more likely to occur in the layers with a larger Bi composition, due to a bigger lattice mismatch with the substrate and their number shall grow during the high-temperature annealing due to stress relaxation in the layer.

3.2 Nonlinear optical effects in GaAsBi

When a semiconductor material interacts with intense laser radiation, various nonlinear optical phenomena are induced. The nonlinear absorption phenomena are usually studied because it is the main principle of operation of modern optical devices like lasers [111], optical switches and optical limiters [112], and telecommunication signal regenerators [113]. The nonlinear absorption is the change in material transmittance as a function of the incident optical beam intensity. There are two reasons that cause a change in material transmittance: a) transmittance can decrease with increasing optical intensity due to multiple photon absorption processes or b) increase with increasing intensity as a result of saturable absorption (SA). The first of these effects is used for optical switching and optical limiting, whereas SA is used in short pulse lasers for Q-switching and mode-locking as well as for the signal regeneration in telecommunication networks.

The semiconductor saturable absorber mirror (SESAM) is an essential component of all modern femtosecond laser systems that are used for the generation of ultrashort pulses by passive mode locking. SESAM contains thin saturable absorber semiconductor layer grown on top of a Bragg reflector for better performance. The operating principle of SESAM is based on the carrier induced bleaching of the optical absorption in a thin semiconductor layer. For most applications, SESAM's should be fast (order of picoseconds), but their speed is limited by the rate of carrier recombination in the absorber layer. Moreover, the absorber layer should be made from a direct band semiconductor that can be integrated in the same epitaxial structure with a high quality Bragg reflector. At the moment, the best SESAMs are fabricated on high index contrast GaAs/AlAs or GaAs/AlO_x distributed Bragg reflectors grown on GaAs substrates. However, the selection of semiconductor materials

that could be grown on GaAs substrates and would have the energy band gaps narrower than that of GaAs (E_g = 1.42 eV) is very limited, which makes the fabrication of SESAMs for long-wavelength, telecommunication range lasers a challenging task. So far, SESAMs with absorber layers containing from GaInNAs quantum wells [114] or InAs quantum dots [115] were demonstrated for mode-locking of 1.3 μm lasers. Quinternary GaInNAsSb layers with dilute amounts of nitrogen grown on GaAs have been used in SESAMs that are designed for a 1.55 μm wavelength range [116,117], however, the absorption recovery times in these materials were too long (longer than 10 ps) for their use in femtosecond pulse generation. Therefore, the search of the appropriate material for this wavelength range is still going on and GaAsBi can be one of them.

3.2.1 Samples

As in the previous subsection $GaAs_{1-x}Bi_x$ samples were grown by molecular beam epitaxy (MBE) on (100) GaAs substrate. The growth temperature was 300 ºC. Sample parameters are presented in Table 2. The samples we grown in the Optoelectronic Technology Laboratory of the Center for Physical Sciences and Technology by Dr. Vaidas Pačebutas and Dr. Renata Butkutė.

Table 2. Parameters of $GaAs_{1-x}Bi_x$ samples

Sample	Thickness (μm)	Bi content (%)	E_g (eV)	Carrier lifetime[a] (ps)	Carrier lifetime[b] (ps)
B290	1.5	4.2	1.08	1.2	1.2
B285	1.5	6.6	0.97	1.4	1.8
B287	1.5	11	0.75	2.1	3.5

[a]from the optical pump-terahertz probe experiment

[b]from the optical pump-optical probe experiment

1.5 μm thick $GaAs_{1-x}Bi_x$ high crystalline quality samples with up to 10% of Bi atom concentration were grown. Bi content x and $GaAs_{1-x}Bi_x$ layer lattice relaxation levels were evaluated from X-ray diffraction (XRD) rocking curves and reciprocal space mapping (RSM) measurements of (400) and (440) reflexes. The energy band gap of $GaAs_{1-x}Bi_x$ layers was defined from optical transmission measurements using conventional spectrometer; the carrier lifetimes were determined from the optical pump – THz probe and optical pump – optical probe measurements.

3.2.2 Experimental setup

All measurements were performed using a tunable wavelength fs laser system which is based on a 1030 nm Yb:KGW laser with a pulse repetition rate of 200 kHz and pulse duration of 160 fs providing 6 W output power that is used for pumping an optical parametric amplifier (OPA). The wavelength of the OPA can be changed from 640 nm to 2600 nm. The tunable fs laser system allows us to measure several semiconductor material parameter dependences on the excitation laser wavelength (or energy).

The open aperture z-scan measurement [118] technique is traditionally used for nonlinear absorption measurements [119], and with the help of OPA we wanted to measure the nonlinear absorption dependence on incident photon energy or, in other words, nonlinear absorption spectrum. However, due to large changes of the OPA optical beam shapes during the wavelength tuning it has been difficult to perform a high-quality z-scan and to reach the goals expected. Therefore, an optical pump – optical probe technique was chosen instead. The setup scheme was introduced in subsection 2.3.4. The electron-hole pairs were generated in the sample by the pump pulses, and the induced absorption was monitored by measuring the change in the transmitted probe pulse energy. The main rule of the pump – probe technique is that the diameter

of the probe beam should be smaller than the pump, and the pump beam should not reach the detector. The pump and probe beams were tightly focused on the sample's surface - on the 0.13 mm and 0.10 mm diameter spots, respectively. The average power of the pump beam was about 100 times larger than the power of the probe beam.

When measuring the light transmission through a thin semiconductor layer, one has often to deal with the potential influence to the results of the substrate absorption. A conventional technique of characterizing thin semiconductor layers is a reflection pump - probe type measurement, but in this case the interpretation of the results is often rather complicated. In our case, the band gap of the $GaAs_{1-x}Bi_x$ layer was smaller than of the GaAs substrate, which has allowed us to perform pump-and-probe measurements in the transmission geometry and without any special sample preparation.

Another common problem of all optical measurements is the quality of the sample surface. In our case it should not scatter the incident light. Quality of our samples was sufficient and no additional polishing procedures were needed.

3.2.3 Measurement results

GaAsBi absorption bleaching

The time-resolved differential transmittance ($\Delta T/T$) measurement results of GaAsBi layers are presented in Figure 20.

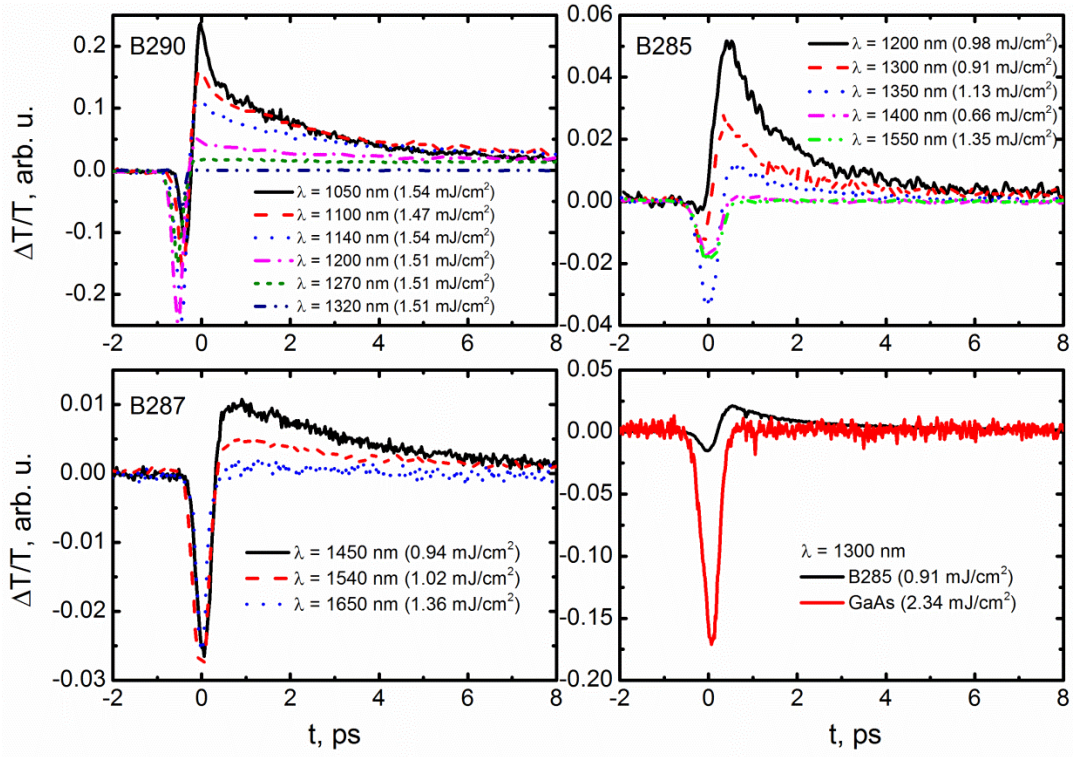

Figure 20. Time-resolved differential transmittance measurement results of GaAsBi samples.

All measured curves of GaAsBi samples were similar and contained two parts: an initial narrow dip and a fast rising peak with slower decay times. The narrow dip corresponds to 2PA of GaAs substrate. This was found after a separate measurement of GaAs and GaAsBi samples in the same conditions (see bottom-right graph on Figure 20). The peak at the longer delays corresponds to the optical absorption bleaching of GaAsBi layer. This bleaching can be attributed to a conduction band filling in the $GaAs_{1-x}Bi_x$ layer because other well-known effects, such as the band gap shrinkage or the free-carrier absorption, can only cause the decrease of a sample's transparency. It seems that both of these effects are much weaker than the band filling when optically injected carrier concentrations are in the 10^{19} cm^{-3} range, though they have to be taken into consideration at higher excitation levels [120].

Performing the time-resolved optical pump - optical probe measurement, we can separate the ultra-fast two-photon absorption of the substrate from the slower free-carrier non-linearities of the layer. The decay of the positive $\Delta T/T$ is determined mainly by the lifetime of non-equilibrium electrons excited by the pump pulse. The lifetime of the free carrier was previously measured using the optical pump - THz probe technique under a relatively low optical carrier density level of ~10^{16} cm^{-3}. It can be seen from Table 2 that, despite the different excitation conditions, the lifetimes measured by the optical pump - THz probe and the optical pump – optical probe techniques are very similar.

GaAsBi bandgap determination method

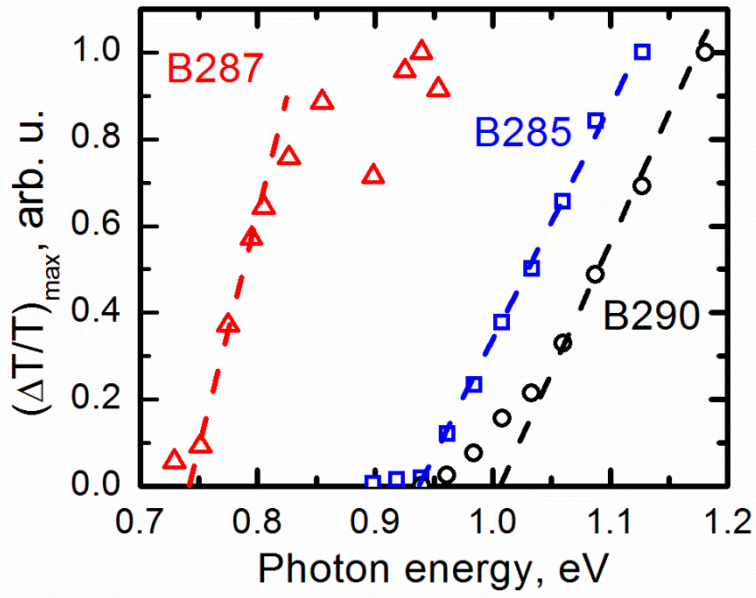

Figure 21. Increase of the transmittance for GaAsBi samples as a function of the laser photon energy. Symbols– experimental data; dashed lines are guide for the eyes.

Figure 21 shows spectral dependences of the induced optical bleaching of three GaAsBi samples. A well defined threshold behavior of this effect is observed. This behavior can be understood by taking into account the changes of a

relative part of the pump pulse energy absorbed in the $GaAs_{1-x}Bi_x$ layer with a changing light wavelength. The absorbed part of the pump pulse energy vanishes when the photon energy becomes smaller than the band gap of the $GaAs_{1-x}Bi_x$ layer. Similarly, the bleaching capability calculated for one pair of carriers vanishes when the photon energy of the probe light becomes smaller than the band gap. As Figure 21 shows, the spectral dependences of induced optical bleaching can be used for a quite accurate determination of the band gap of the GaAsBi layer. This is a rather useful feature, since standard band gap determination methods have serious limitations when used for the characterization of thin $GaAs_{1-x}Bi_x$ layers: the photoluminescence of materials with picosecond carrier lifetimes is relatively weak and the sensitivity of the modulation spectroscopy techniques is restricted by high equilibrium hole densities in bismide layers with a larger Bi content.

Figure 21 shows that the bandgap of sample B287 is around 0.74 eV, which is one of the smallest registered GaAsBi bandgap values. GaAsBi bandgap value of 0.74 eV is equal to approximately 11% to 12% of Bi atom concentration.

Saturable absorption

We chose two laser beam wavelength to measure differential transmittance of the sample B285 at various excitation levels. The 1250 nm wavelength was chosen to be near the sample bandgap and 1050 nm wavelength was chosen because at that wavelength there was very weak 2PA in GaAs substrate. Measurement results are shown in Figure 22. It can be seen that the amplitude of these transients $\Delta T/T$ is changing faster at low pump beam powers and saturating at high pump beam powers.

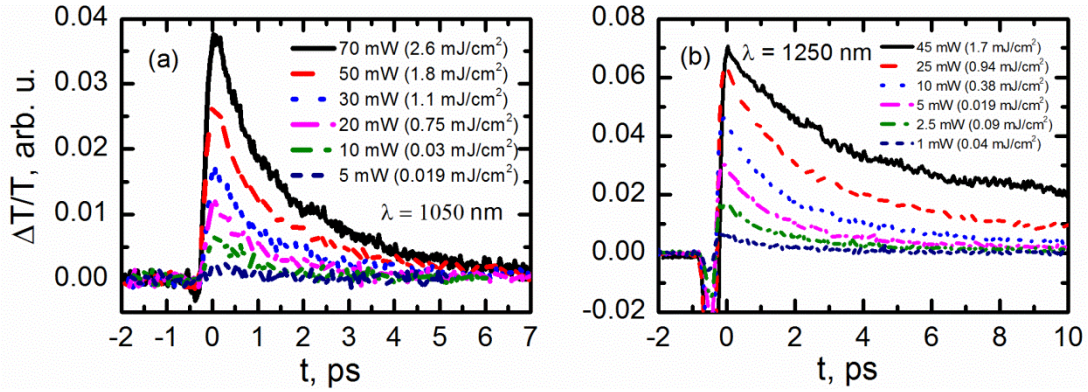

Figure 22. Time-resolved differential transmission signals from sample B285 at various excitation levels at two wavelength: 1050 nm (a) and 1250 (b).

The nonlinearity of the absorbance change can be clearly seen in Figure 23 where the absorption coefficient of sample B285 at two laser wavelengths is plotted as a function of the pump beam fluence.

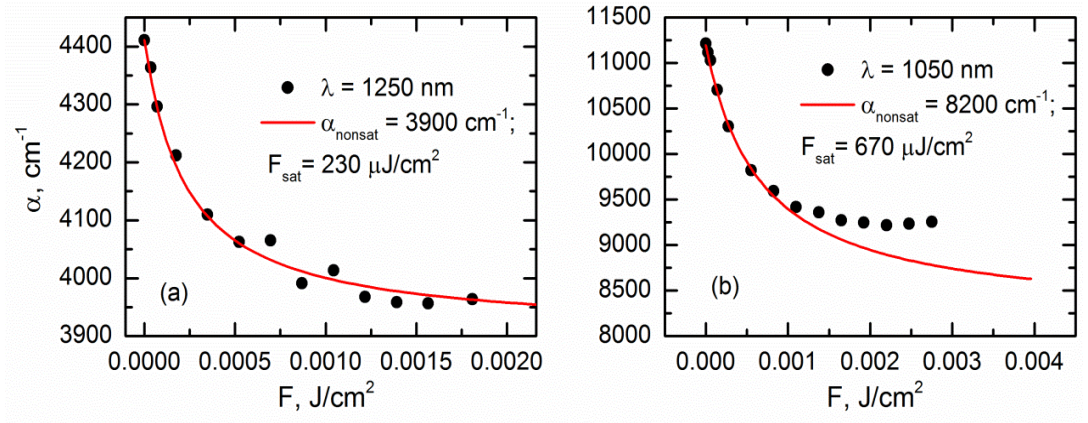

Figure 23. Absorption coefficient of the sample B285 as a function of the pump pulse fluence. The light wavelength is equal to 1250 nm (a) and 1050 nm (b). Points - experimental data; line – calculation result (see text below).

Experimental points presented on this figure were obtained by using the results of the optical pump - optical probe (see Figure 22) and of the conventional transmission spectroscopy experiments; these points were fitted to the theoretical formula for nonlinear absorbance of semiconductors [121]:

$$\alpha(I) = \frac{\alpha_0}{1 + F / F_{sat}} + \alpha_{nonsat}, \quad (22)$$

where $\alpha(I)$ – the intensity - dependent absorption coefficient of the semiconductor layer, α_0 – the saturable linear absorption coefficient, α_{nonsat} – the nonsaturable linear absorption coefficient, F – the energy fluence of the pump pulse, F_{sat} – the saturation fluence. The best fits were achieved with α_{nonsat} = 8200 cm^{-1}, F_{sat} = 0.67 mJ/cm^2 (λ = 1050 nm) and α_{nonsat} = 3900 cm^{-1}, F_{sat} = 0.23 mJ/cm^2 (λ = 1250 nm). These parameters are comparable with typical parameters of the saturable absorbers [119]. The discrepancy between experimental data and the fitting curve observed for λ = 1050 nm wavelength at high excitation levels can be attributed to the free-carrier absorption in the bismide layer.

3.2.4 Conclusions

1. The optical absorption bleaching effect in GaAsBi layers has been observed over a wide wavelength range extending up to 1.6 μm.

2. The non-equilibrium carrier lifetimes of order of a few picoseconds and saturation fluencies comparable with their values to the best known semiconductor saturated absorbers make the investigated GaAsBi samples promising material for near and mid-IR range SESAM devices.

3. The non-linear absorption measurements using the optical pump – optical probe technique are suitable for carrier lifetime measurements and semiconductor band gap determination.

4. THz-TDS experiments

4.1 GaAs Nanowires

The samples with nanostructures like nanowires and nanorods are very promising materials for THz emitters because this structures enhance THz emission from optically excited surfaces as compared to bulk semiconductor. THz emission from low temperature grown InN nanorods was about one order of magnitude greater in power than that from the bulk InN film [122]. The THz emission from samples with Si nanowires [123] was two orders of magnitude stronger than from Si wafers. Seletskiy *et al.* [124] reported 15 times more efficient optical-to-THz power conversion from InAs NW than from InAs substrate, but this result was obtained only by taking in to account spatial fill-factor of NW in a sample. In our research we study samples with GaAs nanowires and also observe THz emission enhancement as compared with GaAs substrate.

4.1.1 Samples

The samples with GaAs nanowires (NW) were obtained from the Institute of Physics, Polish Academy of Sciences (grown and structurally characterized by Prof. Janusz Sadowski group). The sample parameters are presented in Table 3.

Table 3. Physical characteristics of GaAs samples with nanowires

Sample Name	Substrate (orientation)	NW Material	NW Shell	NW thickness (nm)	NW length (μm)
NW 17	GaAs (111) B	GaAs	-	~ 50	Up to 3
NW 25b	GaAs (111) B	GaAs	GaMnAs	~ 60	
NW 26b	GaAs (111) B	GaAs	MnAs		
NW 28b	GaAs (111) B	GaAs 0.5 μm + [InAs 5 nm / GaAs 10 nm] x 50			

NW 29b	GaAs (111) B	0.5 μm GaAs + 3 μm InGaAs	GaMnAs		
NW 32	GaAs (111) B	GaAs	Some MnAs phase		

GaAs nanowires were grown by vapor-liquid-solid method in a solid source MBE reactor on GaAs (111) B substrates at high (~550 °C) temperature. There were two types of GaAs NW samples grown: samples with GaAs NWs and samples with GaAs NWs combined with (Ga,Mn)As ferromagnetic semiconductor or MnAs feromagnetic metal, so called core-shell nanowires. The catalytic growth of primary GaAs core NWs was induced by randomly distributed around 50 nm diameter gold nanodroplets. GaAs nanowires grown on GaAs (111) B substrate grown up to 3 μm long and their diameter was around 50 nm. The growth process took up to several hours. Therefore, GaAs nanowires were grown on (111) orientation substrate, they grow in a vertical direction and their orientation is (111). This can be seen on pictures taken with scanning electron microscope (SEM) (see Figure 24).

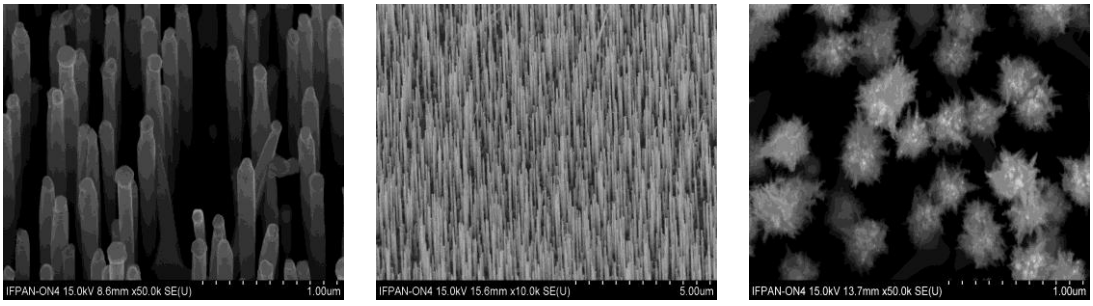

Figure 24. SEM pictures of vertically grown GaAs NWs samples.

The core-shell nanowires were grown in a two-step mode. After the growth of the primary GaAs NW core the growth temperature was lowered to 250 °C and (Ga,Mn)As or MnAs shells were grown around the GaAs NW cores. The growth rate was about 2 Å/min and growth process took about 0.5 h, so the

shell thickness should be about 60 Å. The areal density of as grown nanowires was around 30 NWs per square micrometer as seen in Figure 24.

4.1.2 Measurements

GaAs NW samples were investigated with THz-TDS setup, where samples with nanowires were used as surface THz emitters. The THz radiation at the photoexcited semiconductor surface is generated by a dipole that is usually induced due to fast changing photocurrent or by the changes of nonlinear polarization of the material however, only small amount of generated THz radiation is emitted in to free space because oscillating dipole is oriented perpendicular to the surface of semiconductor (see Figure 25a), and THz radiation are generated parallel to the surface of the semiconductor. Only radiation which falls in-to 15º total internal reflection free cone, escapes from the sample, other part of THz radiation reflects back.

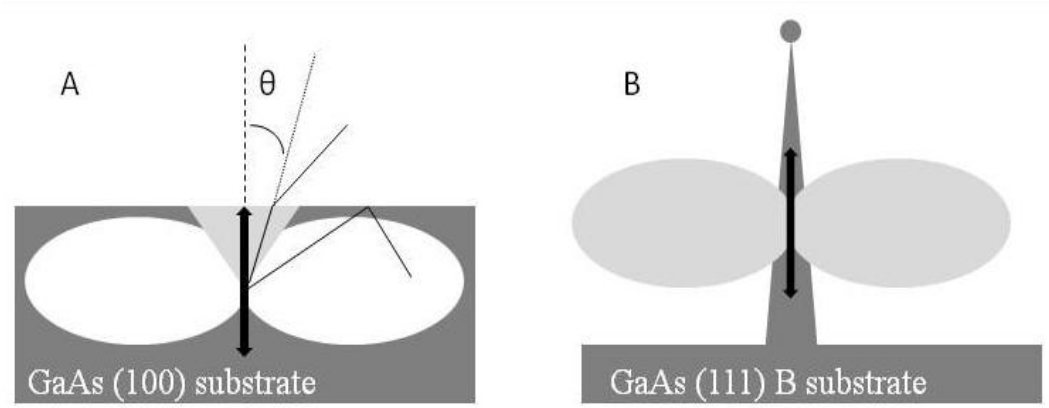

Figure 25. The electric dipole orientation in GaAs substrate (A), and GaAs nanowires (B).

On the other hand, in vertically grown nanowires oscillating dipole is oriented along the nanowires, and THz emission direction is oriented perpendicular to the surface of a nanowire, therefore a much large part of radiation can be

emitted in to free space. This idea was suggested by Seletskiy *et al.* [124] and was starting point of our research.

THz efficiency measurements

First of all, the THz emission from surface of samples with GaAs nanowires measurements were performed, and results were compared with results obtained from GaAs substrate. The measurement setup explained in section 2.3.2 was used. The samples were excited at 45º angle. The obtained THz pulse amplitudes and spectra from samples with GaAs nanowires and bulk GaAs substrate are presented in Figure 26. The results normalized to GaAs peak value are presented in Table 4.

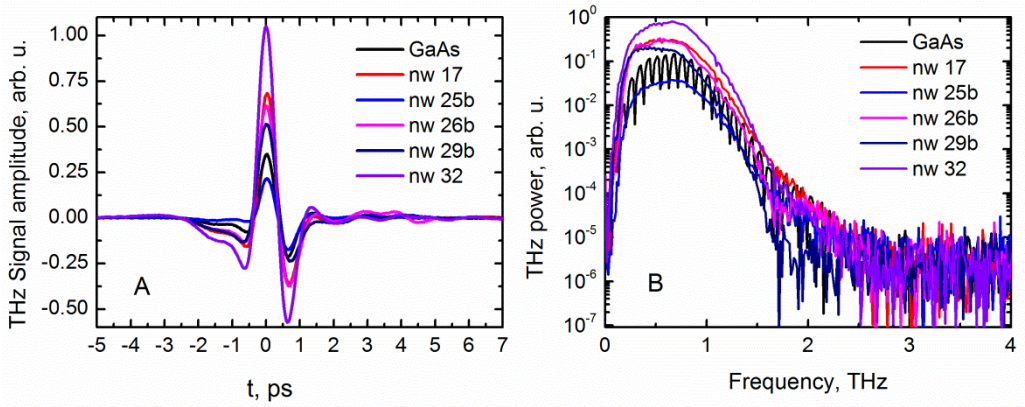

Figure 26. THz signal amplitude (A) and spectra (B) obtained from samples with GaAs NWs and GaAs substrate.

Table 4. THz emission from surface of samples with nanowires peak values normalized to GaAs substrate THz emission peak value.

GaAs	NW 17	NW 25b	NW 26b	NW28B	NW29b	NW 32
1	1.96	0.62	1.76	1.03	1.47	3

As seen from the measurement result, the waveforms of THz pulses are similar, but the samples with GaAs nanowires emit THz radiation 2 - 3 times more efficiently than GaAs substrate, despite their fill factor of only 0.07.

The other measurements were done only with NW 17, NW 26b and NW 32 samples because they emitted THz pulses better than other NW samples and GaAs substrate. The dependence of terahertz emission on an incoming optical beam polarization measurements were done, the results are shown in Figure 27.

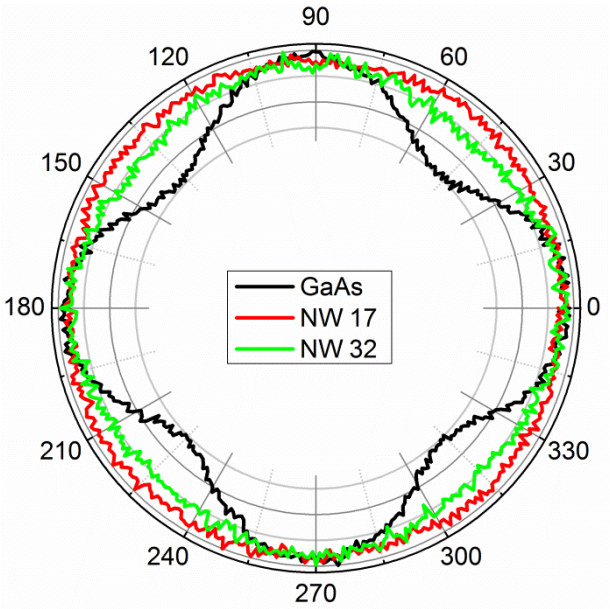

Figure 27. The emitted THz pulse amplitude dependences on an incoming optical beam polarization.

It can be seen that the THz emission from the samples with GaAs nanowires is almost independent on the excitation beam polarization. The behavior of GaAs substrate is also shown in Figure 27 for comparison.

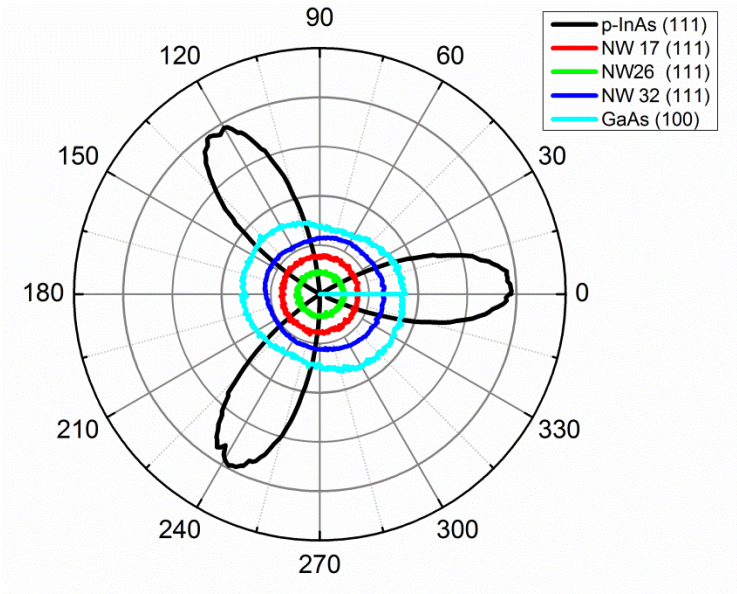

Figure 28. The emitted THz pulse amplitude dependences on sample rotation angle.

The measured azimuthal angle dependencies of the p-polarized excitation revealed two-fold symmetry for GaAs substrate and angle-independent behavior for samples with GaAs NWs (see Figure 28). InAs sample results are presented to show what azimuthal dependence for (111) plane samples should be. Analogical behavior was observed in InAs nanowires [125].

Orientation dependent terahertz emission is a characteristic feature of nonlinear THz generation mechanisms such as optical rectification, thus these processes can be eliminated as sources of THz generation in our NW samples. On the other hand, electric field induced carrier acceleration effects must be considered. Photoexcited carriers can be accelerated in a surface depletion field and in the field at gold cap-nanowire interface; furthermore, the acceleration can occur due to the photo-Dember effect. As nanowire surfaces are oriented in various directions, the THz field originated from NW surface will be zero at the far-field. In contrast, the Schottky barrier between the Au-cap and the NW tip can cause a depletion region with a unidirectional electric field along the

NW that can separate photoexcited electrons and holes and cause the THz emission.

Angular emission characteristics measurements

Measurements

Then we examine the idea that was introduced in Figure 25, that THz radiation should be emitted more efficiently from the side of nanowires because the oscillating dipoles are oriented alongside the nanowires. To determine the direction of the oscillating dipoles in nanowires and their angular emission characteristics, the electric field of generated THz radiation was measured as a function of light incidence angle θ_i. Therefore, the sample holder was modified so, that it has become possible to change the angle between the laser beam and a normal to the sample surface from 0º to 90º (see Figure 29).

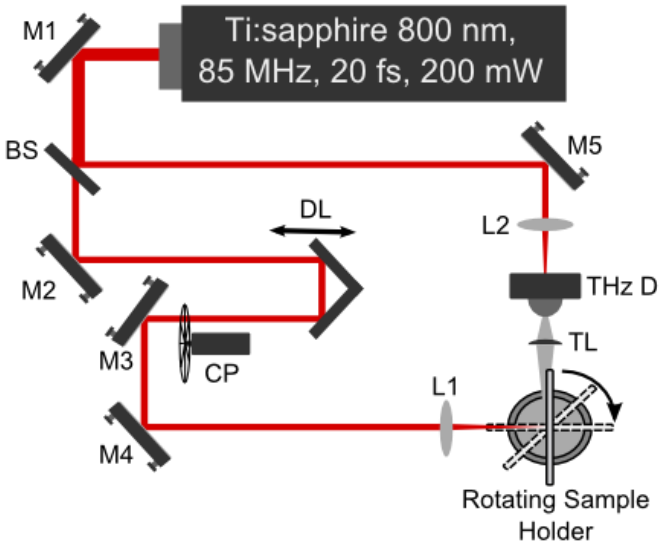

Figure 29. A schematic diagram of the experimental setup with modified sample holder.

The angle between excitation laser beam and detector position was 90º. Only sample excitation angle was changed from 0º - the sample is perpendicular to

the excitation laser beam, to 90º - the sample is parallel to the excitation laser beam. The sample holder was rotated manually every 5º.

The measurements were performed with GaAs substrate and several samples with GaAs nanowires. The results are shown in Figure 30.

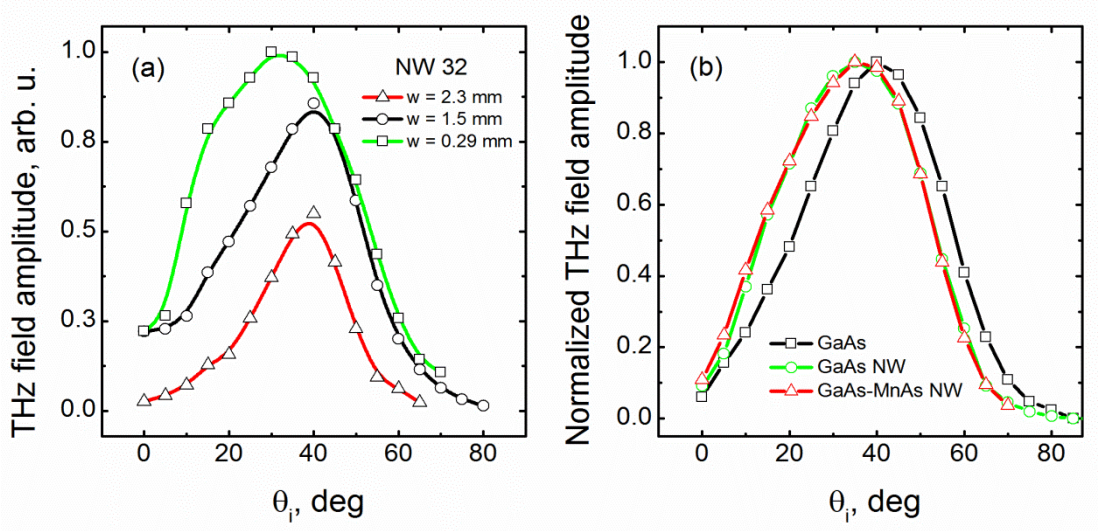

Figure 30. Angular emission characteristics measurements results. Lines are guides for the eyes; (a) the THz pulse amplitude angular dependence on excitation spot size, here *w* is a laser spot radius at a surface of the sample; (b) the THz peak value dependence on sample excitation angle θ_i in GaAs substrate and samples with GaAs nanowires, when w = 0.5 mm.

As expected, THz emission maximum value for bulk GaAs substrate was obtained when angle between laser pulse excitation and sample surface was 45º. However, for samples with GaAs nanowires the THz emission maximum value was obtained at smaller angles. The pump laser spot diameter was around 1 mm.

We also noticed that the angular emission maximum position depends on excitation spot diameter. When optical beam was loosely focused onto the sample surface, a maximum around 45º was observed for all samples.

However, when the pump beam was focused more tightly, angular emission maximum position has shifted to smaller angles, for samples with nanowires this shift was larger than for bulk sample (see Figure 30b).

Model

In our model the THz radiation is generated only in NW layer. The NWs form a homogeneous layer with the effective refraction index n_2, which is a fitting parameter. However, oscillating dipoles emits radiation in all directions, but we neglect THz radiation reflections from GaAs substrate. Dipole approximation method [60] was adopted for interpretation of the angular characteristics measurements results. According to our model, the detectable THz emission field can be expressed as:

$$E_{THz} \sim \sin(\theta_2) \times \left(1 - R_{opt}\right) \times t_{THz} \times E_{\Omega}(\theta_i), \quad (23)$$

where θ_2 defines the terahertz radiation direction inside the sample (see Figure 31), θ_i - optical excitation or sample rotation angle, R_{opt} – the optical reflectivity at the NW surface. The first term $sin(\theta_2)$ originates from the radiation pattern of the dipole approximation when the dipole axis is perpendicular to the sample surface. The second term shows how much optical excitation is transmitted through the sample. The third term t_{THz} is THz field transitivity at semiconductor-air interface. The fourth term is the emission cone correction function:

$$E_{\Omega}(\theta_i) = exp\left[-\left(\frac{2\theta_i - \frac{\pi}{2}}{\Omega}\right)^2\right] \quad (24)$$

where Ω is a divergence angle of the THz radiation beam. The divergence angle is inversely proportional to the optical pump beam diameter at the

sample surface. The emission cone correction function accounts the restrictions determined by the Huygens law, and shows expansion of the THz radiation.

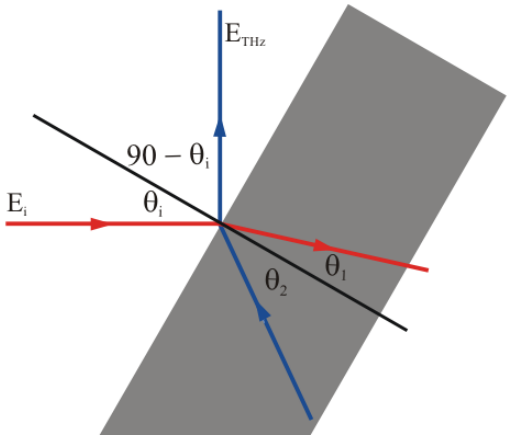

Figure 31. Graphical representation of our model.

For p-polarized THz radiation R_{opt} and t_{THz} has the following forms:

$$R_{opt} = \left(\frac{n_1 \times \cos(\theta_i) - \cos(\theta_1)}{n_1 \times \cos(\theta_i) + \cos(\theta_1)}\right)^2 \tag{25}$$

$$t_{THz} = \frac{2 \times \sqrt{n_2} \times \cos(\theta_2) - \cos\left(\frac{\pi}{2} - \theta_i\right)}{\left(n_2 \times \cos\left(\frac{\pi}{2} - \theta_i\right) + \cos(\theta_2)\right) \times \sqrt{\cos(\theta_2)}} \tag{26}$$

where n_1 and n_2 is the sample refraction index for the optical and terahertz radiation, respectively, and θ_1 is the angle of the refracted optical beam. The relations between angles θ_i, θ_1 and θ_2 are the following:

$$\theta_1 = \arcsin\left(\frac{\sin(\theta_i)}{n_1}\right) \tag{27}$$

$$\theta_2 = \arcsin\left(\frac{\sin\left(\frac{\pi}{2} - \theta_i\right)}{n_2}\right). \tag{28}$$

Discussion

The THz emission independence on a polarization angle was already evidenced in THz emitters made from black silicon [126], and was explained by the light

trapping effects in this nanostructured material. This effect also determines weak light absorption dependence on light beam incident angle, so that $1\text{-}R_{opt}$ is approximately equals to 1 for the whole range of investigated incidence angles. Other three terms of (23) equation has clear maxima: $sin(\theta_2)$ peaks at θ_i = 0º, $t_{THz}(\theta_i)$ has a maximum at a Brewster angle, $E_{\Omega}(\theta_i)$ reaches its higher value at θ_i = 45º. The result of a product $sin(\theta_2) \times t_{THz}(\theta_i)$ has a maximum near Brewster angle at small θ_i, however, at large θ_i it continuously decreases till reaches zero at θ_i = 90º. The $E_{THz}(\theta_i)$ is strongly depends on THz radiation divergence angle Ω and index of refraction n_2. When Ω is small $E_{\Omega}(\theta_i)$ function has a very narrow peak at θ_i = 45º, therefore the result of multiplication with slowly, in this region, varying function $sin(\theta_2) \times t_{THz}(\theta_i)$ gives us the similar shape of $E_{THz}(\theta_i)$ and $E_{\Omega}(\theta_i)$ functions (see Figure 32).

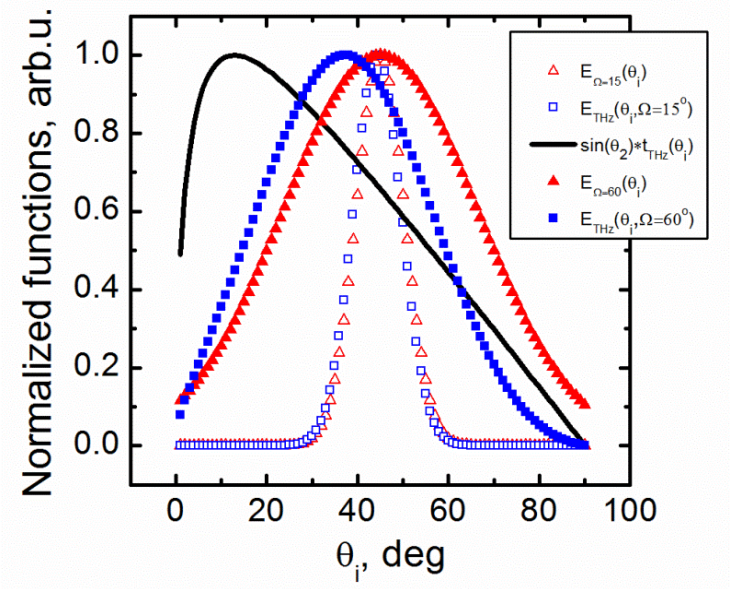

Figure 32. Calculated $E_{THz}(\theta_i)$, $E_{\Omega}(\theta_i)$ and $sin(\theta_2) \times t_{THz}(\theta_i)$ dependencies on optical beam incidence angle θ_i. n_2 = 3.5, black line - $sin(\theta_2) \times t_{THz}(\theta_i)$ function, triangle symbols – $E_{\Omega}(\theta_i)$ functions, square symbols - $E_{THz}(\theta_i)$ functions, open symbols Ω = 60º, filled symbols Ω = 15º.

In the case of quickly expanding beams (Ω is large), $E_{THz}(\theta_i)$ does not repeat the shape of $E_{\Omega}(\theta_i)$ anymore; instead, $E_{THz}(\theta_i)$ maximum shifts toward smaller angles. The larger Ω determines the larger variation of $sin(\theta_2)\times t_{THz}(\theta_i)$ values across the THz beam (see Figure 32) and, subsequently, larger shift of the function $E_{THz}(\theta_i)$ towards smaller θ_i. Regarding the refraction index of material, the larger value of n_2 also determines the larger variation of $sin(\theta_2)\times t_{THz}(\theta_i)$ as well as a larger shift of the function $E_{THz}(\theta_i)$ to the smaller values of angle θ_i (see Figure 33).

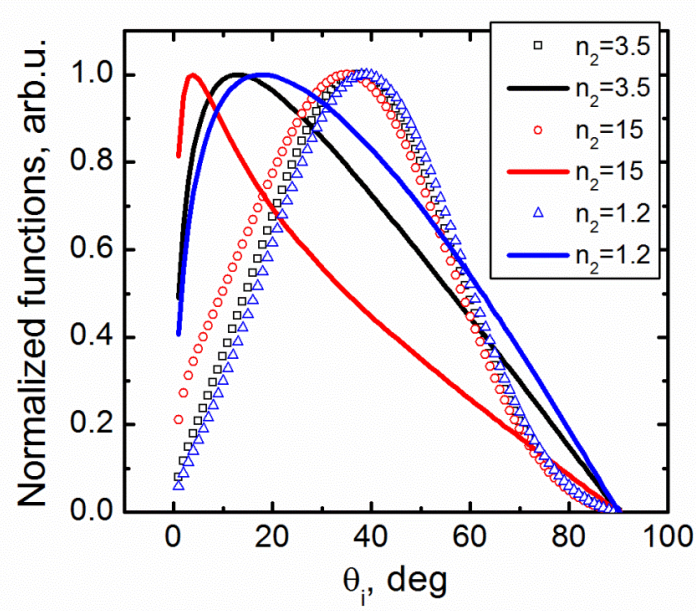

Figure 33. Calculated $E_{THz}(\theta_i)$ (symbols) and $sin(\theta_2)\times t_{THz}(\theta_i)$ (solid lines) dependencies on θ_i and n_2.

A self-evident analogy between the Figure 30 and Figure 33 can be seen. The bigger divergence angles in Figure 33 correspond to the smaller optical beam spots in Figure 30, thus the comparison of experimental and calculated results explains the spot size influence on registered $E_{THz}(\theta_i)$ dependencies. According to our calculations, the index of refraction of the NWs layer in the THz range is higher than in bulk substrate, despite the fact that fill factor of NWs layer is approximately 0.07. The diameter of nanowires in our samples is about 60 nm,

which is too large to result in significant quantum confinement effects, which can enhances the conductivity of the NW layers. The large n_2 enhances Fresnel losses for THz beam significantly; regardless of that, samples with NWs are better THz emitters than bulk GaAs.

THz excitation spectra measurements

For these measurements setup shown in Figure 34 was used.

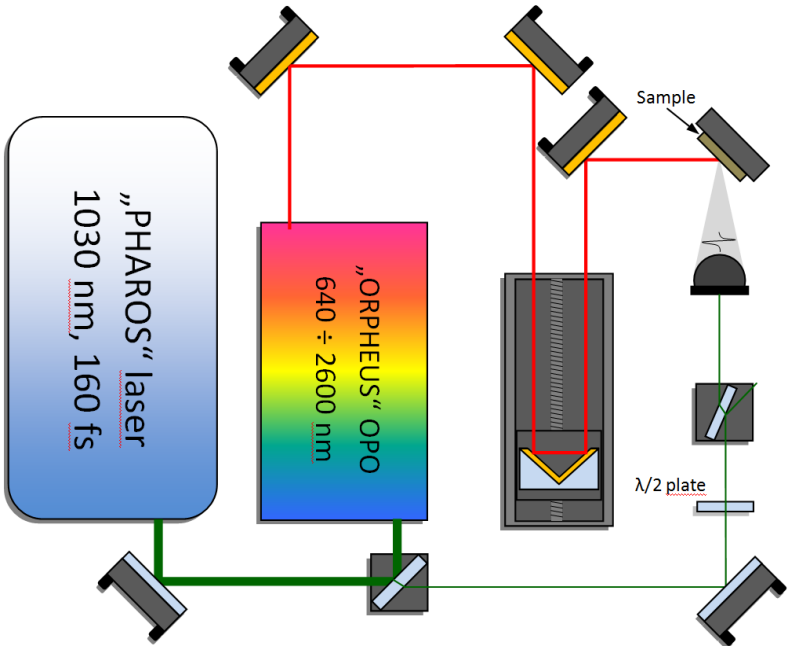

Figure 34. THz excitation spectra measurement setup using optical parametric amplifier.

The Optical parametric amplifier generates tunable 640 nm - 2600 nm wavelength and 140 fs - 160 fs duration pulses at 200 kHz repetition rate. These pulses were used for photoexcitation of the samples with nanowires and GaAs substrate. The THz pulses were detected by GaAsBi photoconductive THz detector which was excited by small part of Yb:KGW laser radiation (≈5 mW). THz excitation spectrum was determined by changing excitation wavelength and measuring peak to peak value of THz transient. Measurements

were performed at a constant optical power (≈5 mW) weaker than the detector saturation level. All spectra were normalized to a constant photon number. This measurement technique was presented in paper [16]. Measurement results are presented in Figure 35a.

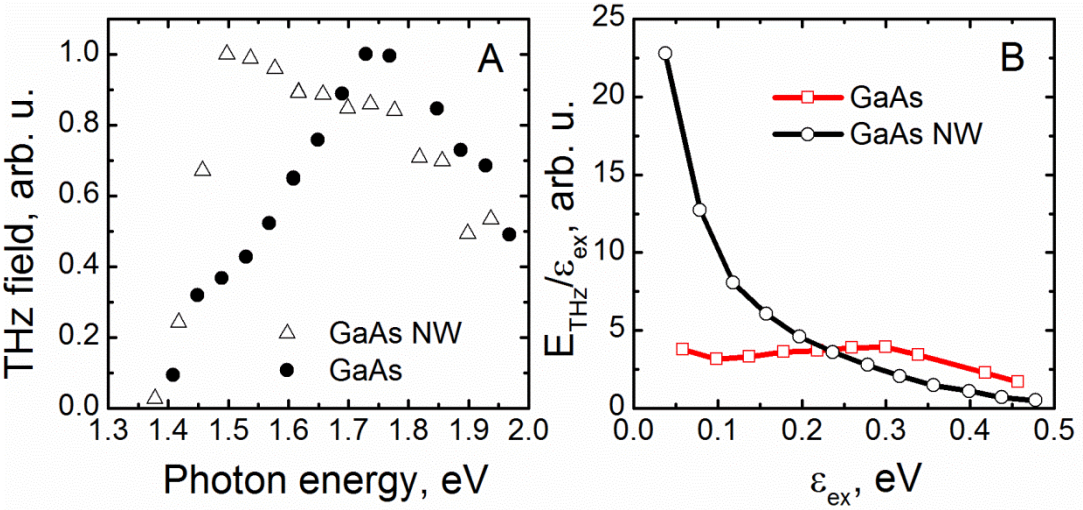

Figure 35. THz field amplitude dependence on the excitation pulse energy for GaAs substrate and GaAs NW samples (A); Normalized THz field amplitude dependence on the electron excess energy ε_{ex} ($\varepsilon_{ex} = h\nu - E_g$) (B).

Figure 35a shows dependences of the THz pulse amplitude radiated from the surfaces of semi-insulating bulk GaAs and NW samples on the pump photon energy. The dependence measured on bulk GaAs has three main features: sharp step at the optical absorption edge, monotonously increasing THz pulse amplitude at higher energies and decrease of this amplitude in the spectral range corresponding to photoexcited electron excess energies larger than 0.3 eV. In contrast, THz excitation spectra of NW samples demonstrate only a sharp increase in the vicinity of GaAs absorption edge followed by a continuous decrease of THz emissivity at higher photon energies.

Figure 35b shows radiated from the surface of GaAs substrate and samples with NW THz pulses amplitudes normalized to ε_{ex}. $\varepsilon_{ex} = h\nu - E_g$, where $h\nu$ is

the laser pulse energy and E_g is material bandgap. At low electron excess energies, THz pulses are mainly generated due to electron and hole separation in the built-in surface electric field. At shorter laser wavelengths the electron and hole separation, due to their different motion away from their excitation positions (photo-Dember effect) also contributes to the THz pulse generation; moreover, initially this separation increases with increasing electron excess energy but afterwards starts to decrease at the energies when the probability of intervalley scattering of electrons becomes significant. The optical density of states for electrons is directly proportional to $\sqrt{(h\nu - E_g)}$. On the other hand, the electrical dipole induced by the separation of photoexcited electrons and holes is approximately proportional to $\sqrt{\varepsilon_{ex}}$ [16]. These relations determine approximately linear dependence between the electron excess energy and the THz pulse amplitude. As predicted, THz pulse amplitude normalized to ε_{ex} is almost independent on electron excess energy for bulk GaAs sample. However, the normalized THz pulse amplitude for the samples with NWs decreases rapidly with increasing ε_{ex}. This behavior can be explained assuming enhanced light absorption due to localized surface plasmon resonances in GaAs nanowires. The similar kind of resonance was observed in Si NW samples [127]. The localized surface plasmon resonance enhances light absorption in the vicinity of the nanowires and this enhancement is bigger for longer wavelengths.

4.1.4 Conclusions

According to the results that were observed we can conclude, that:

1. The samples with GaAs nanowires emit THz radiation 2-3 times better than GaAs substrate, despite the small surface fill factor (0.07) of NWs.

2. The spatial pattern of THz emission in NW samples differs from that of a bare bulk semiconductor. A THz beam that is generated in the NW sample propagates closer to the surface of the sample. This behavior can be explained by large effective index of refraction of NW layers.

3. The better THz generation efficiency of samples with nanowires can be explained assuming enhanced light absorption due to localized surface plasmon resonances in GaAs nanowires.

4.2 Thin film Solar Cells

$CuInS_2$ (CIS) and $Cu(In,Ga)Se_2$ (CIGS) chalcogenide compounds are promising semiconductor materials for thin film solar cells light absorbers. CIS solar cell efficiency ranges from 10% to 12% [128] and the efficiency of the best CIGS - based solar cells is approaching 20% [96]. It means that these technologies are comparable to silicon - based thin film solar cell technology and are cheaper.

THz time domain spectroscopy is non-contact and non-destructive technique which is used to study properties of semiconductor materials. THz radiation generation from the surface of semiconductors method can be used for the characterization of conduction band structures at higher energies, or built-in surface electric field properties (see subsection 2.2.4). THz imaging based on pulsed and CW THz radiation sources was used to study a silicon solar cell with tab wire soldering defects, different reflection coefficients for metalized and non-metalized, structured and unstructured surfaces [129,130]. Study results show that THz pulses can be applied to detect and study different defect types appearing during the solar cell production.

A strong internal electric field is responsible for THz emission from the surface of II–III–VI_2 compounds [97]. This field also leads to the separation of charge carriers in solar cells. Therefore, THz pulses can be used for real-time diagnoses of light absorbers during different manufacturing processes of solar cells. This study is the first step in the development of the method for the characterization of materials that is used in the production of thin film solar cells.

4.2.1 Study of $CuInS_2$ light absorbers

Samples

There are several processing techniques for the preparation of $CuInS_2$ thin films. The most popular is the two-step process. The first step is the production of a precursor Cu–In film by the evaporation or sputter deposition into a vacuum system. During the second step, the precursor film is placed into a sulfurisation furnace filled with H_2S gas or elemental sulfur vapors for the formation of a CIS film.

Studied CIS thin films were produced by the sulfurisation of DC magnetron-sputtered metallic precursor layers on molybdenum-covered soda-lime glass substrates. The sputtering was performed in Ar^+ atmosphere under the pressure of 2 Pa. The sputtering current was 30 mA, voltage 550 V. Under these conditions, the deposition rate was ≈1.1 Å/s. The thickness of the films was about 1 μm. X-ray diffraction analysis confirmed the formation of a single $CuInS_2$ phase and the presence of minor secondary phases $Cu_{2-x}S$.

The CIS samples were obtained from the Center for Physical Sciences and Technology, they were grown and structurally characterized by the Dr. Saulius Balakauskas.

Measurement results

THz surface emission measurements from the CIS samples were performed using the setup that was explained in section 2.3.2. Several CIS samples with different Cu/In atomic ratios values were investigated. The measurement results are presented in Figure 36.

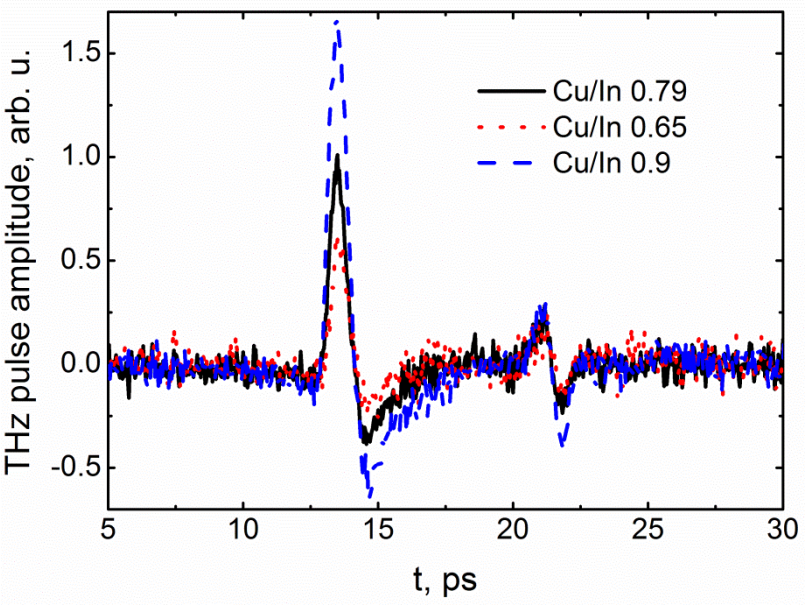

Figure 36. THz pulse waveform, radiated by CIS samples, exited by femtosecond laser pulses at different Cu/In atomic ratios: (1) 0.65, (2) 0.79, and (3) 0.9.

Adomavičius *et al.* has found that terahertz radiation efficiency strongly depends on the stoichiometry of $CuInSe_2$ layers [97]. The THz transient magnitude increases monotonically when the $CuInSe_2$ layer composition gets closer to the stoichiometric composition. On the other hand, the output parameters of the $CuInSe_2$ monograin layer solar cell devices also depend on the composition of absorber material. The highest value of solar cell efficiency is reached when the precursor Cu-In alloy composition ratio varies between $0.9 < Cu/In < 1$ [131].

Our measurement results show similar behavior. THz emission amplitudes radiated by our $CuInS_2$ samples increase monotonically with increasing precursor Cu-In alloy composition ratio and reaches its maximum value when Cu/In ratio equal to 0.9. Much weaker THz emission from $CuInS_2$ thin films was observed at Cu/In ratio ≤ 0.7.

4.2.2 Study of Cu(In,Ga)Se_2 light absorbers

The aim of this research was to use THz emission from the surface of CIGS sample to study dependence of THz emission efficiency on the sample composition during several technological steps.

Samples

The CIGS samples were obtained from the Center for Physical Sciences and Technology, grown and structurally characterized by the Prof. Vincas Tamošiūnas group.

Samples were grown using Alcatel SCM 650 sputtering equipment. First, approximately 1 μm thick molybdenum layer was deposited on top of the polished and cleaned glass plate. Afterwords, approximately a 0.36 μm thick layer was deposited from a single quaternary chalcogenide CIGS target (Pioneer Materials, 20 cm diameter, 6.35 mm thickness, composition: Cu - 22.8 at.%, In - 20 at.%, Ga - 7 at.%, Se - 50.2 at.%). After deposition, the sample was annealed in argon atmosphere for 20 min at 250 ºC and for 40 min at 530 ºC. Then, a 50-60 nm undoped ZnO buffer layer and several 200 nm thick n-type doped ZnO:Al_2O_3 layers were deposited on top of the sample. CIGS samples were grown on 9 × 12 cm^2 glass plate (see Figure 37). Each of the squares corresponds to a CIGS layer segment. Figure 37 shows that sample surface is not homogenous due to a relatively large glass size causing non-uniformity during the deposition step and thermal gradients during the thermal processing step.

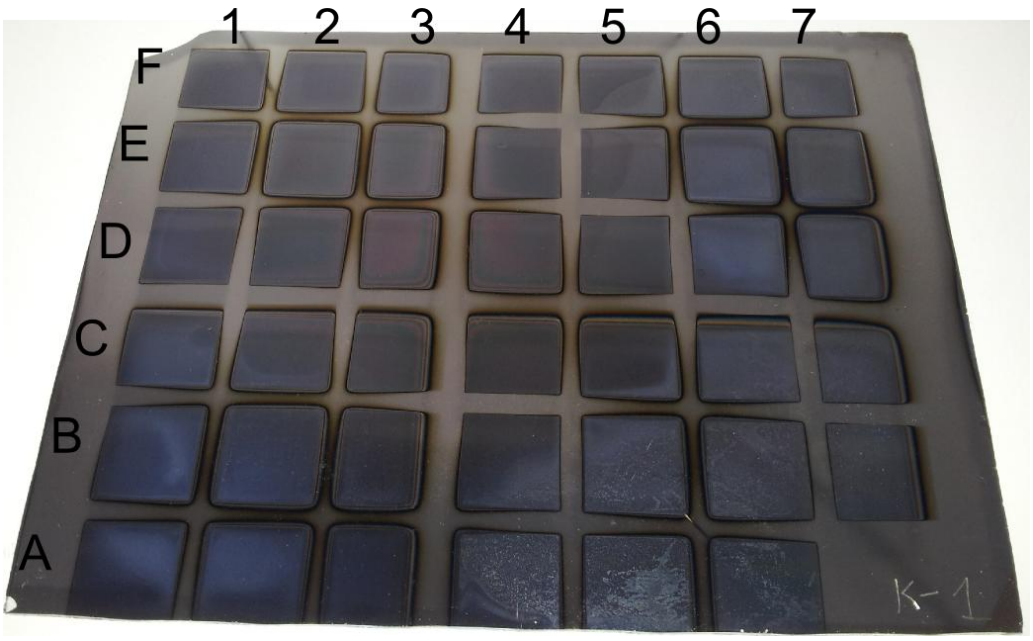

Figure 37. Photograph of CIGS array sample. Numbers and letters are used for indexing.

Measurement results

CIGS samples were studied using THz radiation generation from the surface of the sample setup (see section 2.3.2) and THz excitation spectra measurement [16]. Measurements were taken after each technological step. THz excitation spectra measurements were taken using a tunable laser system (Pharos laser with optical parametric amplifier Orpheus, Light Conversion); this laser system was explained in section 2.3.4. These measurements were taken after each ZnO layer deposition.

First entire CIGS sample array was scanned using the first setup. Due to large sample dimensions, a sample was attached to a 2-axis stage mount; this was done to measure THz emission from each element in the array. Measurement results are shown in Figure 38.

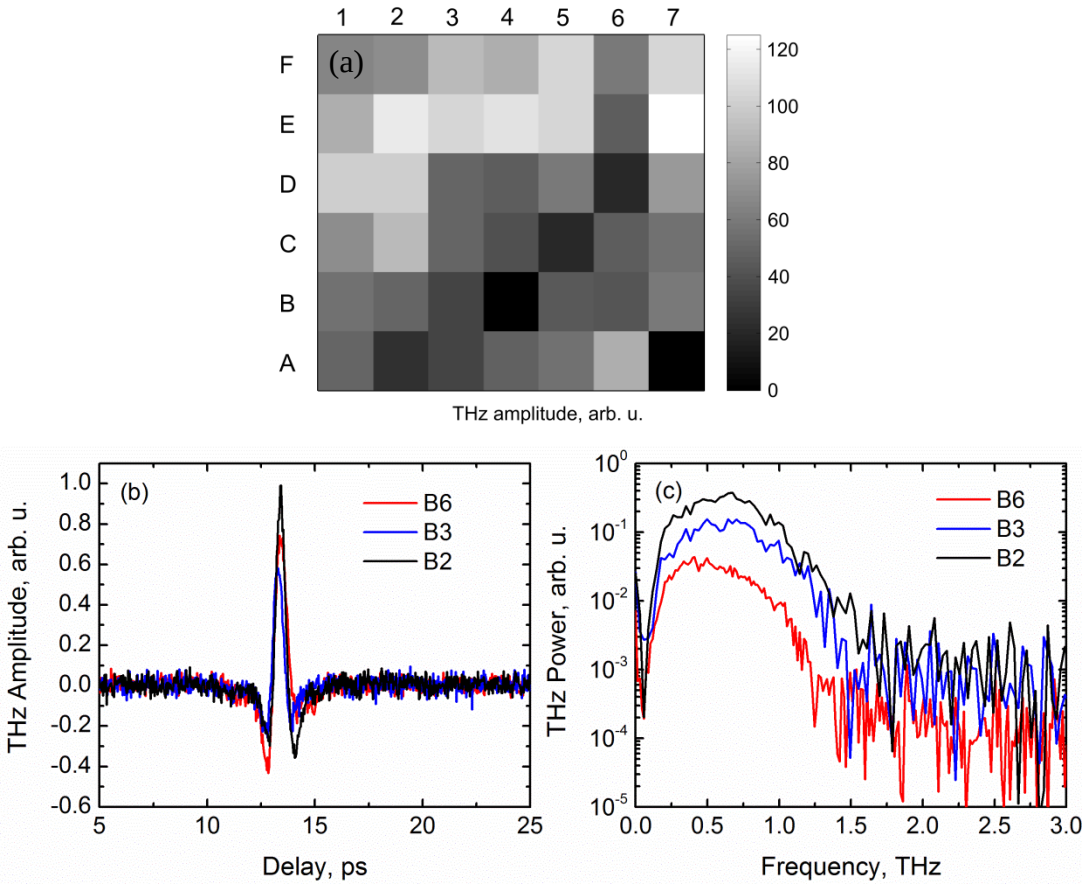

Figure 38. Peak Terahertz amplitude map of CIGS samples (a). Different colors represent THz amplitude values of individual CIGS sample segments. Indexing is the same as in Figure 37. Registered THz emission pulses (b) and their spectra (c) of row B CIGS samples.

As it can be seen in Figure 38a, the THz amplitude distribution of different CIGS samples is random. This can be due to different sample properties caused by unequal growing and annealing conditions for such a large sample. THz pulse waveforms and spectra are similar. Samples with stronger THz emission produce a wider spectrum.

The second technological step was undoped ZnO buffer deposition. A 50 - 60 nm ZnO layer was deposited on top of the sample. After that, another THz

emission from the surface of a sample scan was done. Results are shown in Figure 39.

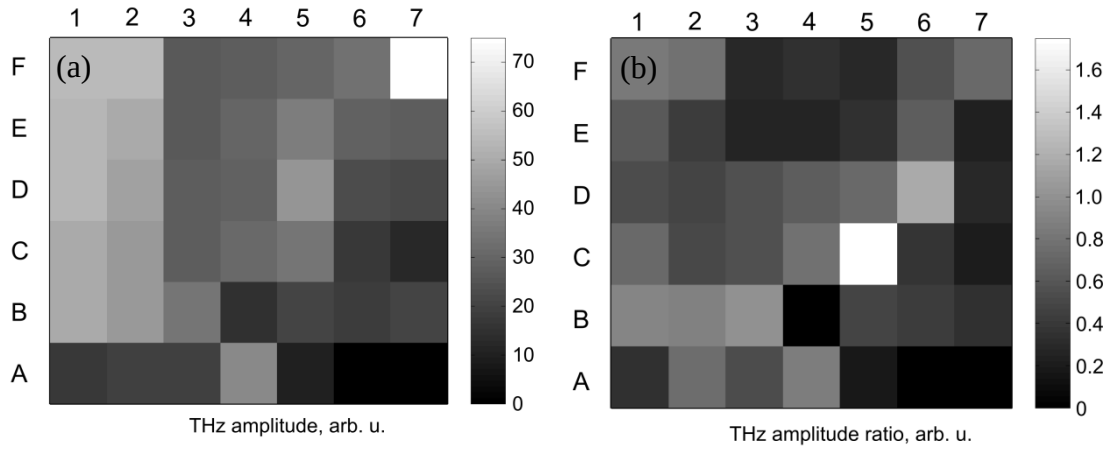

Figure 39. Peak Terahertz amplitude map of CIGS samples with an undoped ZnO layer (a). Ratio of peak THz amplitudes without (see Figure 38a) and with (see Figure 39a) undoped ZnO layer (b). Different colors represent THz amplitude values of individual CIGS sample segments.

After the deposition of ZnO, THz emission of all CIGS samples decreased, but the amplitude map became more uniform. Such results can be attributed to a modification of internal electric fields near the surfaces of CIGS samples by deposition of undoped wide-gap ZnO layer.

Finally, four 200 nm thick n-type doped ZnO:Al_2O_3 layers (standard 2% doping) were deposited on top of the sample. The influence of doped ZnO layer thickness on THz emission efficiency at different excitation energies was studied. The B2 element of CIGS array was chosen for further study. Before and after each doped ZnO layer deposition THz emission at different excitation beam energies was measured from this sample. Measurements were taken using a method described in reference [16]. The obtained results are presented in Figure 40. We can see the growth in the THz emission amplitude as photon energy is increased. This behavior is common to direct bandgap

semiconductors [16]. THz emission starts from 1.2 eV. Below that energy signal is weak. 1.2 eV is the expected bandgap energy of such composition CIGS sample.

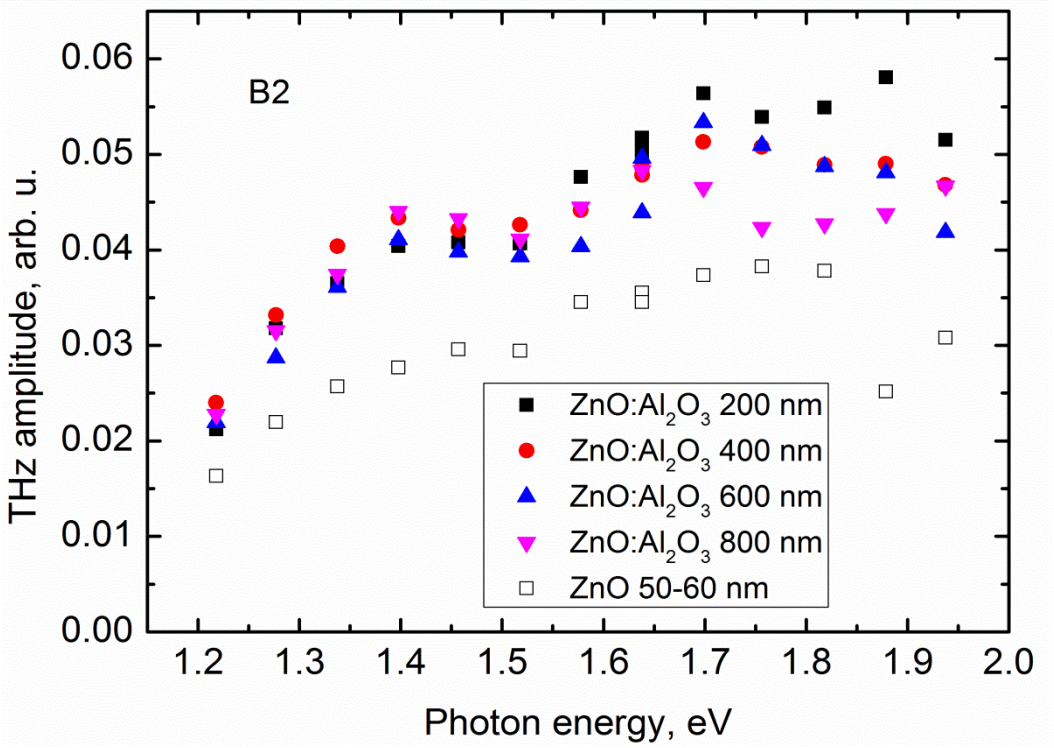

Figure 40. The B2 element of CIGS array THz excitation spectrum. Dependence of doped ZnO layer thickness on THz emission efficiency at different excitation beam energies.

As one can see from the measurement results, doped ZnO layer improved THz emission of the CIGS sample for all excitation beam photon energies. This effect can be attributed to an increased electric field near the CIGS/ZnO/ZnO:Al_2O_3 junction. The CIGS layers are usually p-type, while ZnO:Al_2O_3 is n-type wide bandgap semiconductor. Due to doping of the ZnO:Al_2O_3 layer, the depleted area in such heterostructures should mostly extend into layers below. This means that 200 nm is a sufficient thickness to screen any DC electric fields within this layer. Due to the wide band-gap of

ZnO, it is also transparent for all photon energies in the investigated range and partially transparent in THz [132].

4.2.3 Conclusions

The accomplished studies of CIS and CIGS samples lead to the following conclusions:

1. The THz emission efficiency strongly depends on the stoichiometry of CIS films and shows the highest values when Cu/In ratio equal to 0.9.

2. THz emission from the large area CIGS sample is rather irregular due to imperfections in the grown layers.

3. The THz emission amplitude was reduced after undoped ZnO buffer layer deposition, but increased after n-type ZnO:Al_2O_3 layer deposition.

4. The growth of the THz amplitude was observed above 1.2 eV excitation pulse energy, confirming the expected bandgap on such composition CIGS sample.

Main results

1. Study of post growth annealing of GaAsBi layers leads to the following results:

   - The rapid thermal annealing at temperatures up to 700 ºC has a dual effect on the electron decay characteristics of GaAsBi layers. For samples with 4% of Bi atoms it has minor changes, however for samples with 6% of Bi atoms the non-equilibrium carries lifetime is reduced to less than 1 ps.

   - The PL peak position for sample with 6% of Bi atom annealed at 700 ºC has a blue-shift, which is in line with the results obtained from PT measurements showing that the bandgap energy increases at 80 K.

   - The recombination centers in GaAsBi are more likely to occur in the layers with a larger Bi composition, due to a bigger lattice mismatch with the substrate and their number shall grow during the high-temperature annealing due to stress relaxation in the layer.

2. The study on nonlinear effects in $GaAs_{1-x}Bi_x$ samples with different compositions using the time-resolved optical pump – optical probe technique showed:

   - The optical absorption bleaching effect in GaAsBi layers has been observed over a wide wavelength range extending up to 1.6 μm.

   - The non-equilibrium carrier lifetimes of order of a few picoseconds and saturation fluencies comparable with their values to the best known semiconductor saturated absorbers make the investigated GaAsBi samples promising material for near and mid-IR range SESAM devices.

- The non-linear absorption measurements using the optical pump – optical probe technique are suitable for carrier lifetime measurements and semiconductor band gap determination.

3. Study of THz emission from the surface of samples with GaAs nanowires leads to the following results:

   - The samples with GaAs nanowires emit THz radiation 2-3 times better than GaAs substrate, despite the small surface fill factor (0.07) of NWs.

   - Such behavior can be explained assuming enhanced light absorption due to localized surface plasmon resonances in GaAs nanowires.

4. The accomplished studies of light absorbers based on CIS and GIGS samples show that THz emission from the surface of a semiconductor technique can be used for characterization of thin layer solar cell materials and lead to the following conclusions:

   - The THz emission efficiency strongly depends on the stoichiometry of CIS films and shows the highest values when Cu/In ratio equal to 0.9.

   - The THz emission amplitude of CIGS samples with multilayer ZnO structures on top is strongly depends on ZnO layers thickness and doping.

   - The growth of the THz amplitude was observed above 1.2 eV excitation pulse energy, confirming the expected bandgap on such composition CIGS sample.

References

[1]. D. H. Auston, K. P. Cheung and P. R. Smith, "Picosecond photoconducting Hertzian dipoles", Appl. Phys. Lett. **45**, 284 (1984).

[2]. Ch. Fattinger and D. Grischkowsky, „Terahertz beams“, Appl. Phys. Lett. **54**, 490 (1989).

[3]. M. van Exter, Ch. Fattinger, and D. Grischkowsky, „High-brightness terahertz beams characterized with an ultrafast detector“, Appl. Phys. Lett. **55**, 337 (1989).

[4]. M. Tonouchi, "Cutting-edge terahertz technology”, Nature Photonics **1**, 97 (2007).

[5]. C. Schmuttenmaer, "Exploring Dynamics in the Far-Infrared with Terahertz Spectroscopy", Chem. Rev. **104** (4), 1759 (2004).

[6]. M. C. Kemp, "Explosives Detection by Terahertz Spectroscopy—A Bridge Too Far?", Terahertz Science and Technology **1** (1), 282 (2011).

[7]. D. Grischkowsky, S. Keiding, M. van Exter, and Ch. Fattinger, "Far-infrared time-domain spectroscopy with terahertz beams of dielectrics and semiconductors", JOSA B **7** (10), 2006 (1990).

[8]. M. C. Beard, G. M. Turner, and C. A. Schmuttenmaer, “ Subpicosecond carrier dynamics in low-temperature grown GaAs as measured by time-resolved terahertz spectroscopy“, J. Appl. Phys. **90**, 5915 (2001).

[9]. J. Hebling, K. -L. Yeh, M. C. Hoffmann and K. A. Nelson, "High Power THz Generation, THz Nonlinear Optics, and THz Nonlinear Spectroscopy", IEEE J. Selected Topics in Quantum Electronics **14**, 345(2008).

[10]. M. C. Hoffmann, J. Hebling, H. Y. Hwang, K.-L. Yeh and K. A. Nelson, "THz-pump/THz-probe spectroscopy of semiconductors at high field strengths [Invited]", JOSA B **26** (9), A29, (2009).

[11]. B. B. Hu and M. C. Nuss, "Imaging with terahertz waves", Opt. Lett. **20**, 1716 (1995).

[12]. W. L. Chan, J. Deibel and D. M. Mittleman, "Imaging with terahertz radiation", Rep. Prog. Phys. **70**, 1325 (2007).

[13]. A. Geižutis, R. Adomavičius, A. Urbanowicz, K. Bertulis, A. Krotkus, H.H. Tan and C. Jagadish, "Carrier recombination properties in low-temperature-grown and ion-implanted GaAs", Lithuanian J. Phys. **45**, 249 (2005).

[14]. A. Urbanowicz, R. Adomavičius and A. Krotkus, "Terahertz emission from photoexcited surfaces of Ge crystals", Physica B **367**, 152 (2005).

[15]. R. Adomavičius, J. Macutkevic, R. Suzanovičienė, A. Šiušys and A. Krotkus, "Time-domain terahertz reflection and transmission spectroscopy of InSb", Phys. Status Solidi C **6** (12), 2849 (2009).

[16]. A. Arlauskas and A. Krotkus, "THz excitation spectra of AIIIBV semiconductors", Semicond. Sci. Technol. **27**, 115015 (2012).

[17]. V. Pačebutas, A. Bičiūnas, S. Balakauskas, A. Krotkus, G. Andriukaitis, D. Lorenc, A. Pugžlys and A. Baltuška, "Terahertz time-domain-spectroscopy system based on femtosecond Yb:fiber laser and GaBiAs photoconducting components", Appl. Phys. Lett. **97**, 031111 (2010).

[18]. A. Arlauskas, P. Svidovsky, K. Bertulis, R. Adomavičius, A. Krotkus, "GaAsBi Photoconductive Terahertz Detector Sensitivity at Long Excitation Wavelengths", Appl. Phys. Express **5**, 022601 (2012).

[19]. Ch. Fattinger and D. Grischkowsky, "Point source terahertz optics ", Appl. Phys. Lett. **53**, 1480 (1988).

[20]. M. van Exter, Ch. Fattinger, and D. Grischkowsky, "Terahertz time-domain spectroscopy of water vapor ", Optics Letters **14** (20), 1128 (1989).

[21]. F. W. Smith, H. Q. Le, V. Diaduk, M. A. Hollis, A. R. Calawa, S. Gupta, M. Frankel, D. R. Dykaar, G. A. Mourou and T. Y. Hsiang, "Picosecond GaAs-based photoconductive optoelectronic detectors", Appl. Phys. Lett. **54**, 890 (1989).

[22]. V. Pačebutas, A. Bičiūnas, K. Bertulis and A. Krotkus, "Optoelectronic terahertz radiation system based on femtosecond 1μm laser pulses and GaBiAs detector", Electronics Letters **44** (19), 1154 (2008).

[23]. A. Bičiūnas, "Puslaidininkinių medžiagų, skirtų 1 μm bangos ilgio femtosekundiniais lazerio impulsais aktyvuojamų terahercinių optoelektroninių sistemų komponentams, tyrimas", (Daktaro disertacija, Vilnius, 2012).

[24]. M. Suzuki and M. Tonouchi, "Fe-implanted InGaAs photoconductive terahertz detectors triggered by 1.56 μm femtosecond optical pulses", Appl. Phys. Lett. **86**, 163504 (2005).

[25]. O. Hatem, J. Cunningham, E. H. Linfield, C. D. Wood, A. G. Davies, P. J. Cannard, M. J. Robertson, and D. G. Moodie, "Terahertz-frequency photoconductive detectors fabricated from metal-organic chemical vapor deposition-grown Fe-doped InGaAs", Appl. Phys. Lett. **98**, 121107 (2011).

[26]. K. P. H. Lui and F. A. Hegmann, "Ultrafast carrier relaxation in radiation-damaged silicon on sapphire studied by optical-pump–terahertz-probe experiments", Appl. Phys. Lett. **78**, 3478 (2001).

[27]. E. Knoesel, M. Bonn, J. Shan and T. F. Heinz, "Charge Transport and Carrier Dynamics in Liquids Probed by THz Time-Domain Spectroscopy", Phys. Rev. Lett. **86**, 340 (2001).

[28]. J. Lloyd-Hughes, S. K. E. Merchant, L. Fu, H. H. Tan, C. Jagadish, E. Castro-Camus and M. B. Johnston, "Influence of surface passivation on ultrafast carrier dynamics and terahertz radiation generation in GaAs", Appl. Phys. Lett. **89**, 232102 (2006).

[29]. J. Zhang, A. Belousov, J. Karpiński, B. Batlogg, G. Wicks and R. Sobolewski, "Time-resolved femtosecond optical characterization of multi-photon absorption in high-pressure-grown $Al_{0.86}Ga_{0.14}N$ single crystals", J. Appl. Phys. **110**, 113112 (2011).

[30]. A. Krotkus, R. Adomavičius, G. Molis, A. Urbanowicz and H. Eusebe, "Terahertz radiation from $Cd_xHg_{1-x}Te$ photoexcited by femtosecond laser pulses", J. Appl. Phys. **96**, 4006 (2004).

[31]. Q. Wu and X. -C. Zhang, "7 terahertz broadband GaP electro-optic sensor", Appl. Phys. Lett. **70**, 1784 (1997).

[32]. E. Castro-Camus, L. Fu, J. Lloyd-Hughes, H. H. Tan, C. Jagadish and M. B. Johnston, "Photoconductive response correction for detectors of terahertz radiation", J. Appl. Phys. **104**, 053113 (2008).

[33]. J. Kitagawa, Y. Kadoya, M. Tsubota, F. Iga, T. Takabatake, "Terahertz time-domain spectroscopy of photoinduced carriers in $YTiO_3$", J MAGN MAGN MATER **310**, 913 (2007).

[34]. S. C. Zerbetto, E. C. C. Vasconcellos, L. R. Zink and K. M. Evenson, "Optically pumped far-infrared laser lines and frequencies from $^{13}CD_3OH$", J. Opt. Soc. Am. B. **12**, 1516 (1995).

[35]. B. S. Williams, "Terahertz quantum-cascade lasers", Nature Photonics **1**, 517 (2007).

[36]. Y.-S. Lee, "Principles of Terahertz Science and Technology", (Springer Science+Business Media, LLC) 2009.

[37]. E. R. Brown, K. A. McIntosh, K. B. Nichols and C. L. Dennis, "Photomixing up to 3.8 THz in low-temperature-grown GaAs", Appl. Phys. Lett. **66**, 285 (1995).

[38]. T. K. Ostmann, A. Knobloch, M. Koch, S. Hoffmann, M. Breede, M. Hofmann, G. Hein, K. Pierz, M. Sperling, and K. Donhuijsen, "Continuous-wave THz imaging", Electron. Lett. **37**, 1461 (2001).

[39]. Q. Y. Lu, N. Bandyopadhyay, S. Slivken, Y. Bai, and M. Razeghi, "Room temperature single-mode terahertz sources based on intracavity differencefrequency generation in quantum cascade lasers", Appl. Phys. Lett. **99**, 131106 (2011).

[40]. X. -C. Zhang, B. B. Hu, J. T. Darrow and D. H. Auston, "Generation of femtosecond electromagnetic pulses from semiconductor surfaces", Appl. Phys. Lett. **56**, 1011 (1990).

[41]. S. L. Chuang, S. Schmitt-Rink, B. I. Greene, P. N. Saeta and A. F. J. Levi, "Optical rectification at semiconductor surfaces", Phys. Rev. Lett. **68**, 102 (1992).

[42]. A. Rice, Y. Jin, X. F. Ma, X.-C. Zhang, D. Bliss, J. Larkin and M. Alexander, "Terahertz optical rectification from <110> zinc-blende crystals", Appl. Phys. Lett. **64**, 1324 (1994).

[43]. H. Hamster, A. Sullivan, S. Gordon, W. White and R. W. Falcone, "Subpicosecond, electromagnetic pulses from intense laser-plasma interaction", Phys. Rev. Lett. **71**, 2725 (1993).

[44]. J. Dai, X. Xie and X. -C. Zhang, "Detection of broadband terahertz waves with a laser-induced plasma in gases", Phys. Rev. Lett. **97** (10), 103903 (2006).

[45]. A. Leitenstorfer, S. Hunsche, J. Shah, M. C. Nuss and W. H. Knox, "Detectors and sources for ultrabroadband electro-optic sampling: Experiment and theory", Appl. Phys. Lett. **74**, 1516 (1999).

[46]. C. Kübler, R. Huber, S. Tübel and A. Leitenstorfer, "Ultrabroadband detection of multi-THz field transients with GaSe electro-optic sensors: approaching the near infrared", Appl. Phys. Lett. **85**, 3360 (2004).

[47]. F. Ellrich, T. Weinland, D. Molter, J. Jonuscheit and R. Beigang, "Compact fiber-coupled terahertz spectroscopy system pumped at 800 nm wavelength", Rev. Sci. Instrum. **82**, 053102 (2011).

[48]. P. L. Richards, "Bolometers for infrared and millimeter waves", J. Appl. Phys. **76**, 1 (1994).

[49]. J. -B. Chévrier, K. Baert, T. Slater and A. Verbist, "Micromachined infrared pneumatic detector for gas sensor", Microsyst. Technol. **1**, 71 (1995).

[50]. A. W. M. Lee, B. S. Williams, S. Kumar, Q. Hu and J. L. Reno, "Real−time imaging using a 4.3−THz quantum cascade laser and a 320×240 microbolometer focal−plane array", IEEE Photon. Tech. L. **18**, 1415 (2006).

[51]. A. Dobroiu, M. Yamashita, Y. N. Ohshima, Y. Morita, C. Otani and K. Kawase, "Terahertz imaging system based on a backward oscillator", Appl. Opt. **43**, 5637 (2004).

[52]. S. Verghese, K. A. McIntosh, S. Calawa, W. F. Dinatale, E. K. Duerr and K. A. Molvar, "Generation and detection of coherent terahertz waves using two photomixers", Appl. Phys. Lett. **73** (26), 3824 (1998).

[53]. Q. Wu and X. -C. Zhang, "Free-space electro-optics sampling of mid-infrared pulses", Appl. Phys. Lett. **71**, 1285 (1997).

[54]. J. T. Darrow, B. B. Hu, X. -C. Zhang and D. H. Auston, "Subpicosecond electromagnetic pulses from large-aperture photoconducting antennas", Optics Letters **15** (6), 323 (1990).

[55]. D. You, R. R. Jones, P. H. Bucksbaum and D. R. Dykaar, "Generation of high-power sub-single-cycle 500-fs electromagnetic pulses", Optics Letters, **18** (4), 290 (1993)**.**

[56]. A. Leitenstorfer, S. Hunsche, J. Shah, M. C. Nuss and W. H. Knox, "Femtosecond high-field transport in compound semiconductors", Phys. Rev. B **61**, 16642 (2000).

[57]. K. J. Siebert, A. Lisauskas, T. Löffler and H. G. Roskos, "Field Screening in Low-Temperature-Grown GaAs Photoconductive Antennas", Jpn. J. Appl. Phys. **43**, 1038 (2004).

[58]. A. Krotkus, "Semiconductors for terahertz photonics applications", J. Phys. D: Appl. Phys. **43**, 273001 (2010).

[59]. V. L. Malevich, R. Adomavičius and A. Krotkus, "THz emission from semiconductor surfaces", C. R. Physique **9**, 130 (2008).

[60]. X. -C. Zhang and D. H. Auston, "Optoelectronic measurement of semiconductor surfaces and interfaces with femtosecond optics", J. Appl. Phys. **71**, 326 (1992).

[61]. T. Dekorsy, T. Pfeifer, W. Kütt and H. Kurz, "Subpicosecond carrier transport in GaAs surface-space-charge fields", Phys. Rev. B **47**, 3842 (1993).

[62] M. B. Johnston, D. M. Whittaker, A. Corchia, A. G. Davies and E. H. Linfield, "Simulation of terahertz generation at semiconductor surfaces", Phys. Rev. B **65**, 165301 (2002).

[63]. V. L. Alperovich, V. I. Belinicher, V. N. Novikov and A. S. Terekhov, "Surface photovoltaic effect in gallium arsenide", JETP Pisma **31**, 581 (1980).

[64]. V. L. Alperovich, V. I. Belinicher, V. N. Novikov and A. S. Terechov, "Surface photogalvanic effect in solids - Theory and experiment for band-to-band transitions in gallium arsenide," Soy. Phys. JETP **80**, 2298 (1981).

[65]. R. Inoue, K. Takayama and M. Tonouchi, "Angular dependence of terahertz emission from semiconductor surfaces photoexcited by femtosecond optical pulses", JOSA B **26** (9), A14 (2009).

[66]. M. Reid, I. V. Cravetchi and R. Fedosejevs, "Terahertz radiation and second-harmonic generation from InAs: Bulk versus surface electric-field-induced contributions", Phys. Rev. B **72**, 035201 (2005).

[67]. X. -C. Zhang, J. T. Darrow, B. B. Hu, D. H. Auston, M. T. Schmidt, P. Tham and E. S. Yang, "Optically induced electromagnetic radiation from semiconductor surfaces", Appl. Phys. Lett. **56**, 2228 (1990).

[68]. R. Adomavičius, A. Urbanowicz, G. Molis, A. Krotkus and E. Šatkovskis, "Terahertz emission from p-lnAs due to the instantaneous polarization", Appl. Phys. Lett. **85**, 2463 (2004).

[69]. K. Liu, J. Xu, T. Yuan and X. -C. Zhang, "Terahertz radiation from InAs induced by carrier diffusion and drift", Phys. Rev. B **73**, 155330 (2006).

[70]. P. Gu, M. Tani, S. Kono, K. Sakai and X. -C. Zhang, "Study of terahertz radiation from InAs and InSb", J. Appl. Phys. **91**, 5533 (2002).

[71]. C. Weiss, R. Wallenstein and R. Beigang, "Magnetic-field-enhanced generation of terahertz radiation in semiconductor surfaces", Appl. Phys. Lett. **77**, 4160 (2000).

[72]. M. van Exter and D. Grischkowsky, "Optical and electronic properties of doped silicon from 0.1 to 2 THz", Appl. Phys. Lett. **56**, 1694 (1990).

[73]. P. U. Jepsen, D. G. Cooke, M. Koch, "Terahertz spectroscopy and imaging – Modern techniques and applications", Laser & Photonics Reviews (1), 124 (2011).

[74]. B. M. Fischer, M. Walther and P. U. Jepsen, "Far-infrared vibrational modes of DNA components studied by terahertz time-domain spectroscopy", Phys. Med. Biol. **47**, 3807 (2002).

[75]. L. Duvillaret, F. Garet and J. -L. Coutaz, "A reliable method for extraction of material parameters in terahertz time-domain spectroscopy", IEEE J. Select. Topics Quantum Electron. **2**, 739 (1196).

[76]. L. Duvillaret, F. Garet, and J.-L. Coutaz, "Highly precise determination of optical constants and sample thickness in terahertz time-domain spectroscopy", Appl. Optics **38**, 409 (1999).

[77]. A. Gauthier-Brun, J. H. Teng, E. Dogheche, W. Liu, A. Gokarna, M. Tonouchi, S. J. Chua and D. Decoster, "Properties of $In_xGa_{1-x}N$ films in terahertz range", Appl. Phys. Lett. **100**, 071913 (2012).

[78]. J. Lloyd-Hughes and T. -I. Jeon, "A Review of the Terahertz Conductivity of Bulk and Nano-Materials", J Infrared Milli Terahz Waves **33** (9), 871 (2012).

[79]. D. G. Cooke, F. A. Hegmann, Yu. I. Mazur, W. Q. Ma, X. Wang, Z. M. Wang, G. J. Salamo, M. Xiao, T. D. Mishima and M. B. Johnson, "Anisotropic photoconductivity of InGaAs quantum dot chains measured by terahertz pulse spectroscopy", Appl. Phys. Lett. **85**, 3839 (2004).

[80]. S. E. Ralph, Y. Chen, J. Woodall and D. McInturff, "Subpicosecond photoconductivity of $In_{0.53}Ga_{0.47}As$: Intervalley scattering rates observed via THz spectroscopy", Phys. Rev. B **54**, 5568 (1996).

[81]. M. C. Nuss, D. H. Auston and F. Capasso, "Direct Subpicosecond Measurement of Carrier Mobility of Photoexcited Electrons in Gallium Arsenide", Phys. Rev. Lett. **58**, 2355 (1987).

[82]. D. H. Auston, K. P. Cheung, J. A. Valdmanis and D. A. Kleinman, "Cherenkov Radiation from Femtosecond Optical Pulses in Electro-Optic Media", Phys. Rev. Lett. **53**, 1555 (1984).

[83]. M. Schall and P. U. Jepsen, „Photoexcited GaAs surfaces studied by transient THz time-domain spectroscopy“, Opt. Lett. **25**, 13 (2000).

[84]. M. C. Beard, G. M. Turner and C. A. Schmuttenmaer, "Transient photoconductivity in GaAs as measured by time-resolved terahertz spectroscopy", Phys. Rev. B **62**, 15764 (2000).

[85]. D. G. Cooke, F. A. Hegmann, E. C. Young and T. Tiedje, "Electron mobility in dilute GaAs bismide and nitride alloys measured by time-resolved terahertz spectroscopy", Appl. Phys. Lett. **89**, 122103 (2006).

[86]. A Urbanowicz, R Adomavičius, A Krotkus and V. L. Malevich, "Electron dynamics in Ge crystals studied by terahertz emission from photoexcited surfaces", Semicond. Sci. Technol. **20**, 1010 (2005).

[87]. J.H. Strait, P. A. George, M. Levendorf, M. Blood-Forsythe, F. Rana and J. Park, "Measurements of the Carrier Dynamics and Terahertz Response of Oriented Germanium Nanowires using Optical-Pump Terahertz-Probe Spectroscopy", Nano Lett. **9** (8), 2967 (2009).

[88]. C. Messner, H. Kostner, R. A. Höpfel and K. Unterrainer, "Time-resolved THz spectroscopy of proton-bombarded InP", JOSA B **18** (9), 1369 (2001).

[89]. H. Němec, L. Fekete, F. Kadlec, P. Kužel, M. Martin J. Mangeney, J. C. Delagnes and P. Mounaix, "Ultrafast carrier dynamics in Br^{+}-bombarded InP studied by time-resolved terahertz spectroscopy", Phys. Rev. B **78**, 235206 (2008).

[90]. M. Schall and P. U. Jepsen, "Above-band gap two-photon absorption and its influence on ultrafast carrier dynamics in ZnTe and CdTe", Appl. Phys. Lett. **80**, 4771 (2002).

[91]. M. C. Hoffmann, J. Hebling, H. Y. Hwang, K. -L. Yeh and K. A. Nelson, "Impact ionization in InSb probed by terahertz pump—terahertz probe spectroscopy", Phys. Rev. B **79**, 161201(R) (2009).

[92]. J. Hebling, M. C. Hoffmann, H. Y. Hwang, K. -L. Yeh and K. A. Nelson, "Observation of nonequilibrium carrier distribution in Ge, Si, and GaAs by terahertz pump–terahertz probe measurements", Phys. Rev. B **81**, 035201 (2010).

[93]. R. Adomavičius, G. Molis, A. Krotkus and V. Sirutkaitis, "Spectral dependencies of terahertz emission from InAs and InSb", Appl. Phys. Lett. **87**, 261101 (2005).

[94]. G. Molis, A. Krotkus and V. Vaičaitis, "Intervalley separation in the conduction band of InGaAs measured by terahertz excitation spectroscopy", Appl. Phys. Lett. **94**, 091104 (2009).

[95]. M. A. Contreras, B. Egaas, K. Ramanathan, J. Hiltner, A. Swartzlander, F. Hasoon and R. Noufi, "Progress toward 20% efficiency in Cu(In,Ga)Se_2 polycrystalline thin-film solar cells", Prog. Photovoltaics **7**, 311 (1999).

[96]. P. Jackson, D. Hariskos, E. Lotter, S. Paetel, R. Wuerz, R. Menner, W. Wischmann and M. Powalla, "New world record efficiency for Cu(In,Ga)Se_2 thin-film solar cells beyond 20%", Prog. Photovolt. Res. Appl. **19**, 894 (2011).

[97]. R. Adomavičius, A. Krotkus, J. Kois, S. Bereznev and E. Mellikov, "Terahertz radiation from nonstoichiometric $CuInSe_2$ films excited by femtosecond laser pulses", Appl. Phys. Lett. **87**, 191104 (2005).

[98]. R. Adomavičius, A. Krotkus, R. Šustavičiūtė, G. Molis, J. Kois, S. Bereznev, E. Mellikov and P. Gashin, "Optoelectronic surface emitters of terahertz radiation from copper chalcogenides", Electronics Letters **43** (25), 1458 (2007).

[99]. N. B. Chaure, J. Young, A. P. Samantilleke and I. M. Dharmandasa, "Electrodeposition of p–i–n type $CuInSe_2$ multilayers for photovoltaic applications", Sol. Energy Mater. Sol. Cells **81**, 125 (2004).

[100]. S. Francoeur, M. –J. Seong, A. Mascarenhas, S. Tixier, M. Adamcyk and T. Tiedje, "Band gap of $GaAs_{1-x}Bi_x$, $0<x<3.6\%$", Appl. Phys. Lett. **82,** 3874 (2003).

[101]. K. Bertulis, A. Krotkus, G. Aleksejenko, V. Pačebutas, R. Adomavičius, G. Molis and S. Marcinkevičius, "GaBiAs: A material for optoelectronic terahertz devices", Appl. Phys. Lett. **88**, 201112 (2006).

[102]. K. Yamashita, M. Yoshimoto and K. Oe, "Temperature-insensitive refractive index of GaAsBi alloy for laser diode in WDM optical communication", Phys. Status Solidi C **3**, 693 (2006).

[103]. V. Pačebutas, K. Bertulis, L. Dapkus, V. Aleksejenko, A. Krotkus, K. M. Yu and W. Walukiewicz, "Characterization of low-temperature molecular-beam-epitaxy grown GaBiAs layers", Semicond. Sci. Technol. **22**, 819 (2007).

[104]. Y. Kamo, S. Kitazawa, S. Ohshima and Y. Hosoda, "Highly efficient photoconductive antennas using optimum low-temperature-grown GaAs layers and Si substrates", Jpn. J. Appl. Phys. **53**, 032201 (2014).

[105]. D. E. Aspnes, "Third-derivative modulation spectroscopy with low-field electroreflectance", Surf. Sci. **37**, 418 (1973).

[106]. Y. Tominaga, K. Oe, M. Yoshimoto, "Low Temperature Dependence of Oscillation Wavelength in $GaAs_{1-x}Bi_x$ Laser by Photo-Pumping", Appl. Phys. Express **3**, 062201 (2010).

[107]. V. Pačebutas, K. Bertulis, A. Bičiūnas and A. Krotkus, "Low-temperature MBE-grown GaBiAs layers for terahertz optoelectronic applications", Phys. Status Solidi C **6**, 2649 (2009).

[108]. A. Krotkus, K. Bertulis, M. Kaminska, K. Korona, A. Wolos, J. Siegert, S. Marcinkevičius, J. -F. Roux and J. –L. Coutaz, "Be-doped low-temperature-grown GaAs material for optoelectronic switches", IEE Proc. Optoelectron. **149**, 111 (2002).

[109]. D. Dagnelund, J. Puustinen, M. Guina, W. M. Chen and I. A. Buyanova, "Identification of an isolated arsenic antisite defect in GaAsBi", Appl. Phys. Lett. **104**, 052110 (2014).

[110]. S. Yoon, M. J. Seong, B. Fluegel, A. Mascarenhas, S. Tixier and T. Tiedje, "Photogenerated plasmons in $GaAs_{1-x}Bi_x$", Appl. Phys. Lett. **91**, 082101 (2007).

[111]. U. Keller, K. J. Weingarten, F. X. Kärtner, D. Kopf, B. Braun, I. D. Jung, R. Fluck, C. Hönninger, N. Matuschek and J. Aus der Au, "Semiconductor Saturable Absorber Mirrors (SESAM's) for Femtosecond to Nanosecond Pulse Generation in Solid-State Lasers", IEEE J. Sel. Top. Quantum Electron. **2**, 435 (1996).

[112]. G. S. Maciel, N. Rakov, C. B. de Araujo, A. A. Lipovskii and D. K. Tagantsev, "Optical limiting behavior of a glass-ceramic containing sodium niobate crystallites ", Appl. Phys. Lett. **79**, 584 (2001).

[113]. J. Mangeney, S. Barré, J.-L. Oudar and O. Leclerc, "System application of 1.5 μm ultrafast saturable absorber in 10 Gbit/s long-haul transmission", Electron. Lett. **36**, 1725 (2000).

[114]. R. Grange, A. Rutz, V. Liverini, M. Haiml, S. Schön and U. Keller, "Nonlinear absorption edge properties of 1.3-μm GaInNAs saturable absorbers", Appl. Phys. Lett. **87**, 132103 (2005).

[115]. M. P. Lumb, E. Clarke, E. Harbord, P. Spencer, R. Murray, F. Masia, P. Borri, W. Langbein, C. G. Leburn, C. Jappy, N. K. Metzger, C. T. A. Brown and W. Sibbett, "Ultrafast absorption recovery dynamics of 1300 nm quantum dot saturable absorber mirrors ", Appl. Phys. Lett. **95**, 041101 (2009).

[116]. M. Le Dû, J. -C. Harmand, O. Mauguin, L. Largeau, L. Travers and J. -L. Oudar, "Quantum-well saturable absorber at 1.55μm on GaAs substrate with a fast recombination rate", Appl. Phys. Lett. **88**, 201110 (2006).

[117]. N. K. Metzger, C. G. Leburn, A. A. Lagatsky, C. T. A. Brown, S. Calvez, D. Burns, H. D. Sun, M. D. Dawson, M. Le Dû, J. C. Harmand and W. Sibbett, "Femtosecond pulse generation around 1500nm using a GaInNAsSb SESAM", Optics Express **16** (23), 18739 (2008).

[118]. V. Pačebutas, A. Stalnionis, A. Krotkus, T. Suski, P. Perlin, and M. Leszczynski, "Picosecond Z-scan measurements on bulk GaN crystals", Appl.Phys. Lett. **78**, 4118 (2001).

[119]. V. Pačebutas, G. Aleksejenko, A. Krotkus, J. W. Ager III, W. Walukiewicz, H. Lu and W. J. Schaff, "Optical bleaching effect in InN epitaxial layers", Appl. Phys. Lett. **88**, 191109 (2006).

[120]. B. R. Bennett, R. A. Soref, J. A. Del Alamo, "Carrier-induced change in refractive index of InP, GaAs and InGaAsP", IEEE J. Quantum Electron. **26**, 113 (1990).

[121]. C. Porzi, M. Guina, N. Calabretta, A. Bogoni and L. Poti, "Applications of Saturable Absorption-based Nonlinear Vertical-Cavity Semiconductor Devices for All-Optical Signal Processing", Semiconductor Technologies, Jan Grym (Ed.), ISBN: 978-953-307-080-3, InTech, p.325 (2010).

[122]. H. Ahn, Y. P. Ku, Y. C. Wang, C. H. Chuang, S. Gwo and C. L. Pan, "Terahertz emission from vertically aligned InN nanorod arrays", Appl. Phys. Lett. **91**, 132108 (2007).

[123]. G. B. Jung, Y. J. Cho, Y. Myung, H. S. Kim, Y. S. Seo, J. Park and C. Kang, "Geometry-dependent terahertz emission of silicon nanowires", Optics Express **18**, 16353 (2010).

[124]. D. V. Seletskiy, M. P. Hasselbeck, J. G. Cederberg, A. Katzenmeyer, M. E. Toimil-Molares, F. Leonard, A. A. Talin and M. Sheik-Bahae, "Efficient terahertz emission from InAs nanowires", Phys. Rev. B **84**, 115421 (2011).

[125]. A. Arlauskas, J. Treu, K. Saller, I. Beleckaitė, G. Koblmüller and A. Krotkus, "Strong Terahertz Emission and Its Origin from Catalyst-Free InAs Nanowire Arrays", Nano Lett. **14** (3), 1508 (2014).

[126]. P. Hoyer, M. Theur, R. Beigang and E. B. Kley, "Terahertz emission from black silicon ", Appl. Phys. Lett. **93**, 091106, (2008).

[127]. L. –W. Chou, N. Shin, S. V. Sivaram, M. A. Filler, "Tunable Mid-Infrared Localized Surface Plasmon Resonances in Silicon Nanowires", J. Am. Chem. Soc. **134**, 16155 (2012).

[128]. R. Klenk, J. Klaer, Ch. Koble, R. Mainz, S. Merdes, H. Rodriguez-Alvarez, R. Scheer and H. W. Schock, "Development of $CuInS_2$-based solar cells and modules", Sol. Energ. Mater. Sol. Cell. **95**, 1441 (2011).

[129]. L. Minkevičius, R. Suzanovičiene, S. Balakauskas, G. Molis, A. Krotkus, G. Valušis and V. Tamošiūnas, "Detection of tab wire soldering defects on silicon solar cells using terahertz time-domain spectroscopy", Electronics Letters **48**, 932 (2012).

[130]. L. Minkevičius, R. Suzanovičienė, G. Molis, A. Krotkus, S. Balakauskas, R. Venckevičius, I. Kašalynas, I. Šimkienė, G. Valušis and V. Tamošiūnas, "Terahertz techniques for solar cell imaging", AIP Conf. Proc. **1566**, 375 (2013).

[131]. M. Kauk, M. Altosaar, J. Raudoja, A. Jagomägi, M. Danilson and T. Varema, "The performance of $CuInSe_2$ monograin layer solar cells with variable indium content**"**, Thin Solid Films **515**, 5880 (2007).

[132]. G. Ma, D. Li, H. Ma, J. Shen, C. Wu, J. Ge, S. Hu and N. Dai, "Carrier concentration dependence of terahertz transmission on conducting ZnO films", Appl. Phys. Lett. **93**, 211101 (2008).